12-2017

The study of atomic quasi-stable states, decoherence and cooling of mesoscale particles

Changchun Zhong
Purdue University

STUDY OF ATOMIC QUASI-STABLE STATES, DECOHERENCE AND COOLING OF MESOSCALE PARTICLES

A Dissertation

Submitted to the Faculty

of

Purdue University

by

Changchun Zhong

In Partial Fulfillment of the

Requirements for the Degree

of

Doctor of Philosophy

December 2017

Purdue University

West Lafayette, Indiana

THE PURDUE UNIVERSITY GRADUATE SCHOOL STATEMENT OF COMMITTEE APPROVAL

Dr. Francis Robicheaux, Chair

Department of Physics and Astronomy

Dr. Chris Greene

Department of Physics and Astronomy

Dr. Tongcang Li

Department of Physics and Astronomy

Dr. Martin Kruczenski

Department of Physics and Astronomy

Approved by:

Dr. John Finley

Head of the School Graduate Program

ACKNOWLEDGMENTS

I would like to express my special appreciation to my advisor, Prof. Robicheaux, who is a tremendous mentor for me. I feel really grateful for all his help, advice and encouragement during my graduate study.

I also thank Prof. Greene, Prof. Li and Prof. Love as my thesis committee members. Special thanks to Prof. Kruczenski for his kind agreement as my committee member at my last minute request.

Thanks to my beloved parents, sister, and brother. Thanks to my dear wife Qiao Liu for her whole-hearted support and endless love. Words here can not express how grateful I am to them. Without their support and encouragement, it would be impossible for me to complete my studies in the US.

Thanks to Jingcheng Liang, Qiang Zhang, Bin Yan, Jie Hui for being wonderful friends. Thanks to Matt Eiles, Hyunwoo Lee, Teri Price and Xiao Wang for being amazing colleagues.

TABLE OF CONTENTS

LIST OF TABLES

LIST OF FIGURES

Figure Page

Figure Page

ABSTRACT

Zhong, Changchun PhD, Purdue University, December 2017. STUDY OF ATOMIC QUASI-STABLE STATES, DECOHERENCE AND COOLING OF MESOSCALE PARTICLES. Major Professor: Francis Robicheaux.

Quantum mechanics, since its very beginning, has totally changed the way we understand nature. The past hundred years have seen great successes in the application of quantum physics, including atomic spectra, laser technology, condensed matter physics and the remarkable possibility for quantum computing, etc. This thesis is dedicated to a small regime of quantum physics.

In the first part of the thesis, I present the studies of atomic quasi-stable states, which refer to those Rydberg states of an atom that are relatively stable in the presence of strong fields. Through spectrally probing the quasi-stable states, series of survival peaks are found. If the quasi-stable electrons were created by ultraviolet (UV) lasers with two different frequencies, the survival peaks could be modulated by continuously changing the phase difference between the UV and the IR laser. The quantum simulation, through directly solving the Schrödinger equation, matches the experimental results performed with microwave fields, and our studies should provide a guidance for future experiments.

Despite the huge achievements in the application of quantum theory, there are still some fundamental problems that remain unresolved. One of them is the so-called quantum-to-classical transition, which refers to the expectation that the system behaves in a more classical manner when the system size increases. This basic question was not well answered until decoherence theory was proposed, which states that the coherence of a quantum system tends to be destroyed by environmental interruptions. Thus, if a system is well isolated from its environment, it is in principle possible to observe macroscopic quantum coherence. Quite recently, testing quantum principles

in the macroscale has become a hot topic due to rapic technological developments. A very promising platform for testing macroscale quantum physics is a laser levitated nanoparticle, and cooling its mechanical motion to the ground state is the first step.

In the second part of this thesis, we develop the theory of decoherence for a mesoscopic system's rotational degrees of freedom. Combining decoherence in the translational degrees of freedom, the system's shot noise heating is discussed. We then focus on cooling the nanoparticle in the laser-shot-noise-dominant regime using two different feedback cooling schemes: the force feedback cooling and the parametric feedback cooling. Both quantum and classical calculations are performed, and an exact match is observed. We also explore the parameters that could possibly affect the cooling trend, where we find that the cooling limit for both cooling schemes strongly depends on the position measurement efficiency, and it poses good questions for researchers interested in achieving ground state cooling: what is the best measurement efficiency for a given measurement setup and what can be done to get a better measurement efficiency?

1. INTRODUCTION

This thesis is composed of two different research directions: One is the study of atomic quasi-stable states (Chaps. 2 and 3) [1, 2]; the other is the theory of decoherence for mesoscopic particles and its application to the cooling of laser trapped nanoparticles (Chaps. 4, 5 and 6) [3–5].

In Chaps. 2 and 3, as is reported in Refs. [1, 2], quantum simulations of quasi-stable states of Rydberg atoms are presented. The term quasi-stable state [6–8] refers to an atomic Rydberg state that is relatively stable in the presence of strong laser fields. In the simulations, we spectrally probe the quasi-stable states in the presence of strong infrared (IR) fields, where series of survival peaks are found. We also study coherence effects when the quasi-stable electrons are created by ultraviolet (UV) lasers with two different frequencies. As expected, the survival peaks are greatly modulated when we continuously change the phase difference between the UV and the IR laser. Our quantum simulation, through directly solving the Schrödinger equation, matches the experimental result done with microwave fields [6].

In Chap. 4, as is reported in Ref. [3], the theory of decoherence for a mesoscale particle's rotational degrees of freedom is discussed. Decoherence is a mechanism for a quantum system to gradually lose its quantum coherence due to the interaction with its environment [9], and it plays an important role in explaining the quantum-to-classical transition. Based on a scattering decoherence model [10], we derive a general expression of the decoherence rate for a quantum system in its rotational degrees of freedom. The decoherence rate is related to the difference of the scattering amplitudes for different orientational configurations. To understand the general result, we calculate two examples of scattering decoherence from two different environment particles, thermal photons and air molecules. The scattering of environmental particles

is the main sources of decoherence of macroscopic quantum systems, and thus plays a vital role in the emergence of classicality in the world around us.

In Chaps. 5 and 6, as is reported in Refs. [4, 5], we discuss the shot noise heating and feedback cooling of a laser trapped nanoparticle, both semi-classically and quantum mechanically. We first show that the decoherence from the laser beam corresponds to shot noise heating of the nanoparticle. For a laser trapped nanoparticle, this shot noise heating from the laser always exists no matter how well the nanoparticle is isolated from its thermal environment. Remarkably, recent experiments show that the current technology is already able to isolate the nanoparticle in the laser-shot-noise-dominant regime [11], which leads to hope for ground state cooling. In Chap. 5, the classical parametric feedback cooling is analyzed, and we compare in great detail the parameters that could possibly affect the cooling limit in the particle's translational and rotational degrees of freedom, such as the nanoparticle shape, the dielectric constant, or the laser parameters etc. In Chap. 6, by adopting the theory of continuous quantum measurement [12], the quantum version of force feedback and parametric feedback cooling is discussed. The feedback signal is obtained by continuously monitoring the position of the nanoparticle. The system evolution is described by a stochastic master equation (SME) or equivalently a stochastic Schrödinger equation (SSE). The force feedback and parametric cooling are simulated by numerically unraveling the SME. Our calculation shows that the force feedback cooling can give us a much lower cooling limit than that from a parametric cooling scheme. We also perform semi-classical calculations of the force feedback and parametric feedback cooling, which yield exactly the same results as those from the fully quantum calculations. By rescaling the semi-classical equation, we find that the cooling dynamics only depends on three parameters: feedback strength, position measurement efficiency, and the occupation number change due to the laser shot noise during one oscillation period. Interestingly, the position measurement efficiency is shown to be the key ingredient in obtaining a lower cooling limit. Thus, lastly we give a brief analysis of the position measurement efficiency for a widely used measurement scheme in experiments: the

balanced homodyne detection scheme. Under certain approximations, an intrinsic measurement efficiency is obtained which sets an upper bound for the measurement efficiency that can be reached in experiments.

Chapter 7 gives a brief summary of the thesis and an outlook for future work is discussed.

2. SPECTRUM OF QUASI-STABLE STATES

In this chapter, the quasi-stability of highly-exicited H and He atoms in a strong infrared (IR) field is discussed based on three-dimensional quantum calculations [1]. The spectra of atoms that survive the IR field show a series of IR-frequency-modulated peaks which extend from deeply bound states all the way to the ionization threshold and above. The atoms that survive mainly consist of highly-excited Rydberg states, even after hundreds of the intense IR cycles. Also, they tend to have initial energies which allow emission or absorption of an integer number of IR photons to reach these quasi-stable states. Peaks above the ionization threshold in the survival spectra indicate the existence of multi-photon assisted recombination in the intense IR field.

2.1 Introduction

Quasi-stable states of Li atoms in a strong microwave field has recently been discussed [6–8, 13, 14]. Arakelyan et al. [8] showed that when laser-excited atoms of Li were exposed to an intense microwave pulse, ~ 10% of the atoms were found in Rydberg states subsequent to the pulse, even if the microwave was far more intense than that required for static field ionization. Similar phenomenon of atoms in a strong laser pulse has been predicted and extensively discussed for the past half century [15–17]. Various mechanisms for strong-field stabilization of atoms have been proposed [18–21], and some related experimental papers can be found in Refs. [22–24].

Considering the existence of quasi-stable states of atoms in the presence of a strong microwave field, it is possible to study them spectrally. In the microwave experiment of Refs. [7, 8], Arakelyan et al. measured the optical spectra of Li atoms that survive the strong microwave field. They found a periodic train of peaks separated by the microwave frequency. The experimental observations suggest that Li atoms survive

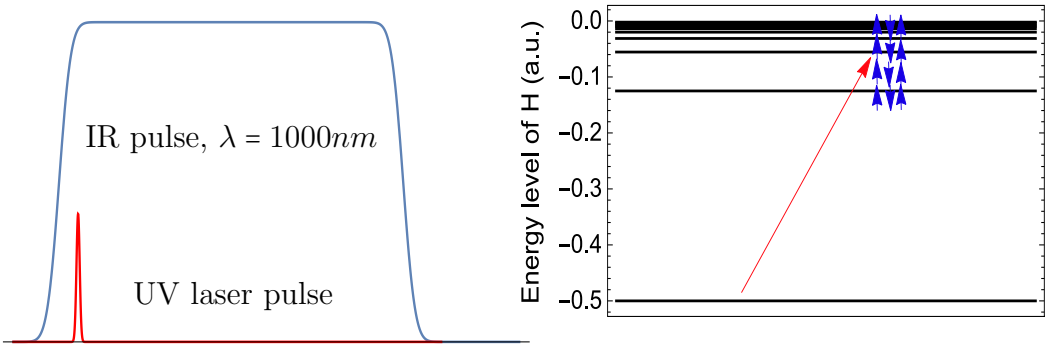

(a) (b)

Figure 2.1. **(a)** The timing envelope for the UV laser and IR field used in our simulation. We choose the duration of the UV laser (four IR cycles) in a way that is short on the scale of the IR duration and long on the scale of IR laser cycles. The duration of the IR is about 1.6×10^4 a.u.. **(b)** Each black line corresponds to an energy level of the H atom. The red arrow shows the electron being brought to the desired state by a UV laser. Then, the electron (blue arrow) continues evolving in the presence of the IR field plus atomic potential.

the intense microwave field in quasi-stable states, where the Rydberg electron stays in a weakly bound orbit infrequently visiting the Li core. Interestingly, the spectrum also revealed peaks above the ionization threshold which is explained by multi-photon assisted recombination [13, 14]. Those electrons excited to the continuum are able to stimulatedly emit a certain number of microwave photons, thus causing the recombination of ions and electrons [14].

Since quasi-stable states can also form in an intense laser field [15–17], one natural thing to do is to detect them spectrally. In this chapter, we spectrally probe the quasi-stable states of H and He atoms in the presence of an intense IR field by numerically solving the three-dimensional (3D) time dependent Schrödinger equation [1]. In order to simulate a prospective experiment, the IR laser is smoothly turned on and off in our calculation, and a weak UV laser is used to prepare atoms at the desired states, as shown in Fig. 2.1(a). After the IR laser is turned off, we compute the probability

of atoms in excited, bound states. The survival spectra show a periodic train of peaks separated by the IR frequency extending from deeply bound states to the ionization threshold and above. To get more information about the bound electrons, we also calculate the survival population as a function of principal quantum number of the electron after the IR field is turned off. The results show that the majority of the population is concentrated in high-lying states. Our analysis not only indicates the existence of multi-photon assisted recombination in a strong IR field, but also reveals that the atoms in IR fields, similar to the case in microwave fields, derive their quasi-stability from the time electrons spend away from the nucleus. In the sections which follow, we introduce the numerical approach that we use, present the results and analysis, compare them to our expectations, and comment on their implications.

We use atomic units except where explicitly stated otherwise.

2.2 The model and numerical method

Similar to the recent experiment of Li atom in a microwave field [8], we assume all atoms are in the ground state at the beginning, then a weak UV laser is turned on to bring atoms to the desired states through one photon absorption, while the IR field is on all the time. In the numerical simulation, we treat the UV laser as a source term since it is weak. After the UV laser is off, the source term stops providing electrons to the near threshold energy region. The IR field keeps interacting with the atoms until it is smoothly turned off. Figure 2.1 shows a schematic picture of the time evolution of atoms, with the short arrows in Fig. 2.1(b) denoting the IR laser induced multi-photon transitions. The wavelength of the IR field is fixed at λ = 1000 nm, which corresponds to frequency $\omega \sim 0.0455$ a.u.. The intense IR field is treated in a non-perturbative manner. In order to study the influence of the IR field strength on the quasi-stable states of atoms, we use six different IR intensities, which are I, 4I, 9I, 16I, 25I, 36I with I = 2.66×10^{11} W/cm^2. These IR intensities are

weak in the sense of affecting the ground states of H and He atoms, while strong in the sense of interacting with their excited states.

The dynamics is governed by the following time dependent Schrödinger equation

$$i\frac{\partial\Psi(\vec{r},t)}{\partial t} = H\Psi(\vec{r},t), \tag{2.1}$$

where the wave function and Hamiltonian can be written in the form $\Psi(\vec{r},t) = \Psi_g(\vec{r},t) + \Psi_e(\vec{r},t)$, and $H = H_0 + H_{UV} + H_{IR}$. $\Psi_g(\vec{r},t)$ is the ground state wave function and $\Psi_e(\vec{r},t)$ is the wave function of the electron after it has absorbed one UV photon. In the simulation, the IR field is treated non-perturbatively while the UV laser is treated using first order time dependent perturbation approximation. Noticing $i\partial\Psi_g(\vec{r},t)/\partial t = H_0\Psi_g(\vec{r},t)$, Eq. 2.1 can be written as

$$i\frac{\partial\Psi_e(\vec{r},t)}{\partial t} - \tilde{H}\Psi_e(\vec{r},t) = S(\vec{r},t) = H_{UV}\Psi_g(\vec{r},t). \tag{2.2}$$

$S(\vec{r},t) = F_{UV}(t)z\Psi_g(\vec{r})\exp(-i(E_g + \omega_{UV})t)$, which acts as a source of amplitude for $\Psi_e(\vec{r},t)$. The UV laser in the source takes a Gaussian envelope, $F_{UV}(t) \propto \exp(-t^2/2t_w^2)$ and t_w is chosen to make sure it lasts 4 IR periods in time (The duration controls the peak width in the energy domain). $\Psi_e(\vec{r},t)$ is initially zero everywhere before the UV laser is on. $\tilde{H} = H_0 + H_{IR}$, which reads

$$\tilde{H} = -\frac{1}{2}\nabla^2 + V(\vec{r}) - F_{IR}(t)z. \tag{2.3}$$

The third term in Eq. 2.3 is the interaction (dipole approximation is used) between the atom and the IR field (linearly polarized). The IR field strength is

$$F_{IR}(t) = F_{max}\cos(\omega_{\mathrm{IR}}t)\left(\mathrm{erf}[\frac{(t-t_i)}{t_w}] - \mathrm{erf}[\frac{(t-t_f)}{t_w}]\right). \tag{2.4}$$

The IR field is smoothly turned on and off through the use of two error functions, as depicted in Fig. 2.1(a). $V(r)$ is the interaction of the electron with the nucleus and the core electrons (if any). For the H atom, $V(r)$ is a pure Coulomb potential, while for the He atom the following model potential is used,

$$V(r) = -0.5\frac{\alpha}{r^4}\left(1 - \exp(-(\frac{r}{r_c})^3)\right)^2 - \frac{Z^*}{r}, \tag{2.5}$$

where $\alpha = 0.81, r_c = 1$, and $Z^* = 1 + \exp(-4.746r) + 0.2125r\exp(-3.537r)$. The model potential gives energy levels of the spin singlet of a He atom. The eigenvalues, except the ground state energy, deviate less than 0.1% from the energy levels of a He atom. The single active electron approximation is considered in our calculation since the strengths and frequencies of the fields insures that only a single electron will participate in the dynamics.

The quantum simulation is performed by numerically solving Eq. 2.2. The wave function is represented on a 2D space spanned by discrete radial points and an angular momentum basis. For the radial part, a nonlinear square root mesh is used. The propagation operator is constructed using a split-operator technique of the form,

$$U(\delta t) = U_1(\delta t/2)U_2(\delta t)U_1(\delta t/2), \tag{2.6}$$

where the approximation $U_i(\delta t) = (1 - iH_i\delta t/2)/(1 + iH_i\delta t/2)$ is used. During the time propagation, an absorbing potential is used. The radial position where the absorbing potential is turned on is set far away from the nucleus such that the potential mainly absorbs the ionized electron. One can refer to [25] for the numerical method in detail. In the following, all the data shown are collected after the IR field is smoothly turned off.

2.3 Results and discussions

We first discuss the results for a H atom. In order to see enough peaks in the spectrum, we choose to study the launch energy (the initial energy of electrons) ranging from $E = -0.17$ a.u. to $E = 0.11$ a.u. relative to the ionization threshold. This range covers about seven IR photons. In our simulation, the different launch energies are obtained by tuning the frequency of the UV laser. The duration of the UV laser is about four IR cycles, which is appropriate for us to see the spectrum in the energy domain (The peaks in the energy domain will be sharper for longer duration of the UV laser pulse). For each launch energy, we calculate the survival

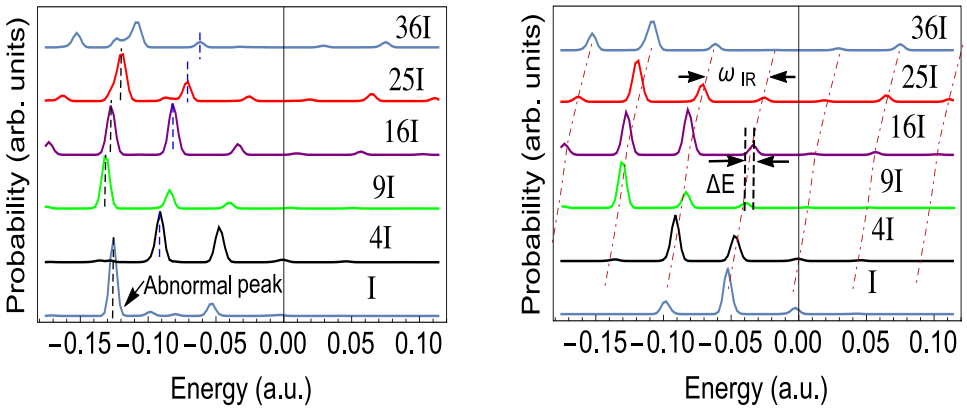

(a) (b)

Figure 2.2. For each solid curve from the bottom to the top, IR field intensity increases from I, 4I, 9I, 16I, 25I to 36I. **(a)** Each curve records the total survival probability of H as a function of the launch energy. The vertical dotted lines help to locate the peak positions. **(b)** Each curve records the survival probability of H in states with principal quantum number bigger than six as a function of the launch energy. The faint (nearly vertical) lines are calculated to track the right shifting of the peaks with increasing intensities. $\triangle E$ is the difference of peak shifts for intensities 16I and 9I. The periodic structure keeps the same even when we double the IR duration.

probability after the IR field is smoothly turned off, and results with six different IR intensities are compared.

In Fig. 2.2, the six curves correspond to the results of six different intensities, which increase from the bottom to the top. First, those curves mainly consist of a series of peaks, which are separated by the energy of one IR photon. Meanwhile, as shown in Fig. 2.2(a), an abnormal peak appears when the IR intensity is relatively weak. For instance, for the curve with intensity I = 2.66×10^{11} W/cm^2, one may expect the first left peak to sit a little left, but it is at E = −0.125 a.u., which is the first excited energy level of H atom. In this case, electrons with initial energy close to E = −0.125 a.u. will be stuck there (the 2p state) because the IR field intensity is too weak to trigger multiphoton transition at that binding energy. In other words, multiphoton

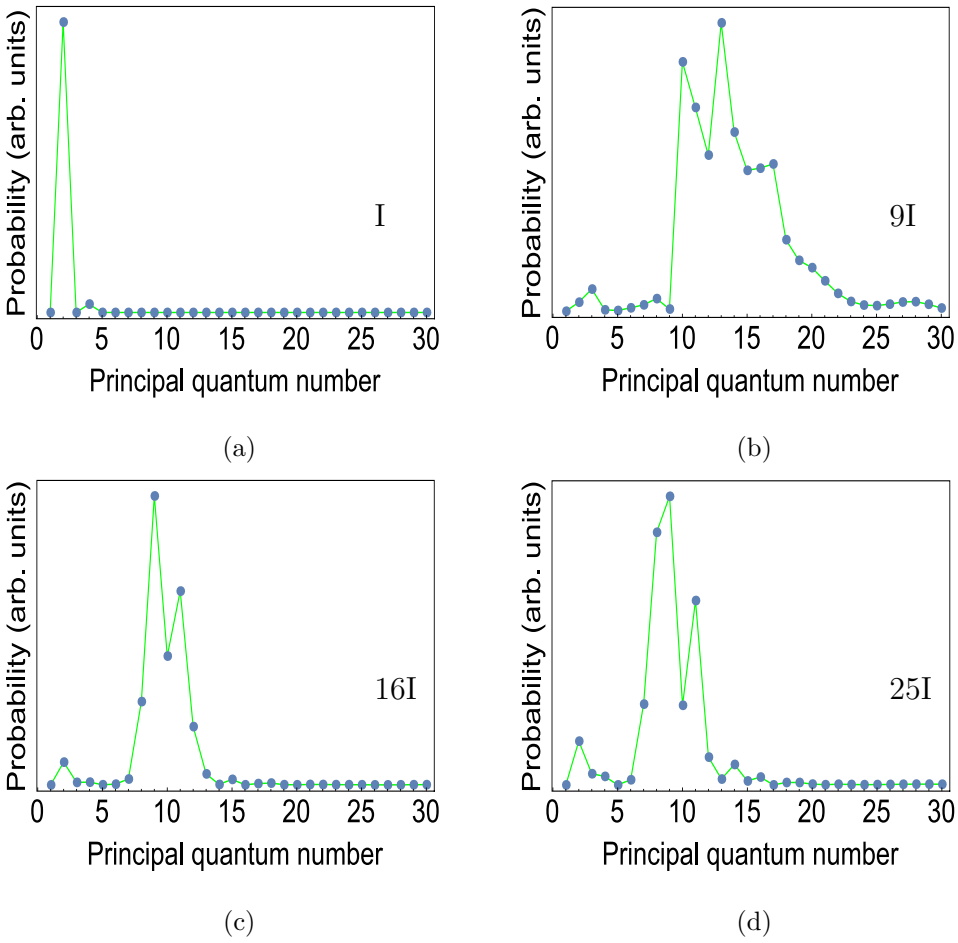

Figure 2.3. Survival probability distribution of H in each bound state for launch energy close to the first ($n = 2$) excited state. **(a)** IR intensity I = 2.66×10^{11}W/cm^2, and the initial launch energy $E = -0.125$ a.u. (marked by a vertical black line in Fig. 2.2(a)). **(b)**, IR intensity is 9I, and $E = -0.132$ a.u.. **(c)**, IR intensity is 16I. $E = -0.128$ a.u.. **(d)**, IR intensity is 25I. $E = -0.120$ a.u.. The energies are marked with vertical line in 2.2(a). For cases (b), (c) and (d), the survival probability concentrates on the highly excited states (The peak principal quantum number $n \sim 10$).

process is a necessary condition for the formation of IR-frequency-modulated peaks. In Fig. 2.2(b), the abnormal peak disappears because we only count the probability of electrons bound in high-lying states. In the following section, we will see it more clearly from the probability distribution in each energy eigenstate. Second, as the field strength increases, the peaks above the ionization threshold gradually emerge, which indicates that the so-called multi-photon assisted recombination also happens in the IR field [14]. It would be interesting for experimentalists to see how far the peaks can go above the threshold if the field strength keeps increasing. Third, all the peaks tend to shift to the right with increasing intensities (the dotted nearly vertical curves make it obvious), and the shifting amount is exactly the difference of ponderomotive energy in various IR fields. Take the curves with intensity 16I and 9I for example, the amount of shifting is $\triangle E \sim 0.006$ a.u.. This shift equals the difference of the ponderomotive energies of electrons when subjected to the corresponding IR fields, which is $\triangle E = F_{16\mathrm{I}}^2/4\omega_{\mathrm{IR}}^2 - F_{9\mathrm{I}}^2/4\omega_{\mathrm{IR}}^2$. This phenomenon can be understood if one imagines that the energy levels of high-lying states are shifted by the ponderomotive energy, thus the resonance is also shifted [26]. The peaks respectively are shifted by a different amount because electrons in the IR field with bigger intensity have bigger ponderomotive energy. As a final point, the periodic structure is still found when we increase the IR duration ($T_{IR} = 3.2\times10^4$ a.u.), which is much longer than the Rydberg period ($T_{Ryd} = 2\pi n^3 \simeq 6000$ a.u.).

In order to understand how the electrons survive, we perform a projection of the final wave function to each bound state. By doing this, we are able to see how the survival probability is distributed in each bound state. Figures 2.3 and 2.4 show the results for different IR intensities and different initial launch energies.

The situation depicted in Fig. 2.3(a) is obviously different from Fig. 2.3(b)-2.3(d). The first excited state holds nearly all electrons that survive the IR field. This actually corresponds to the abnormal peak in Fig. 2.2(a). The launch energy is close to the first excited energy level and the IR intensity is relatively small ($\mathrm{I} = 2.66 \times 10^{11}$ W/cm^2). The intensity is too small to trigger multiphoton absorption from the IR field, so

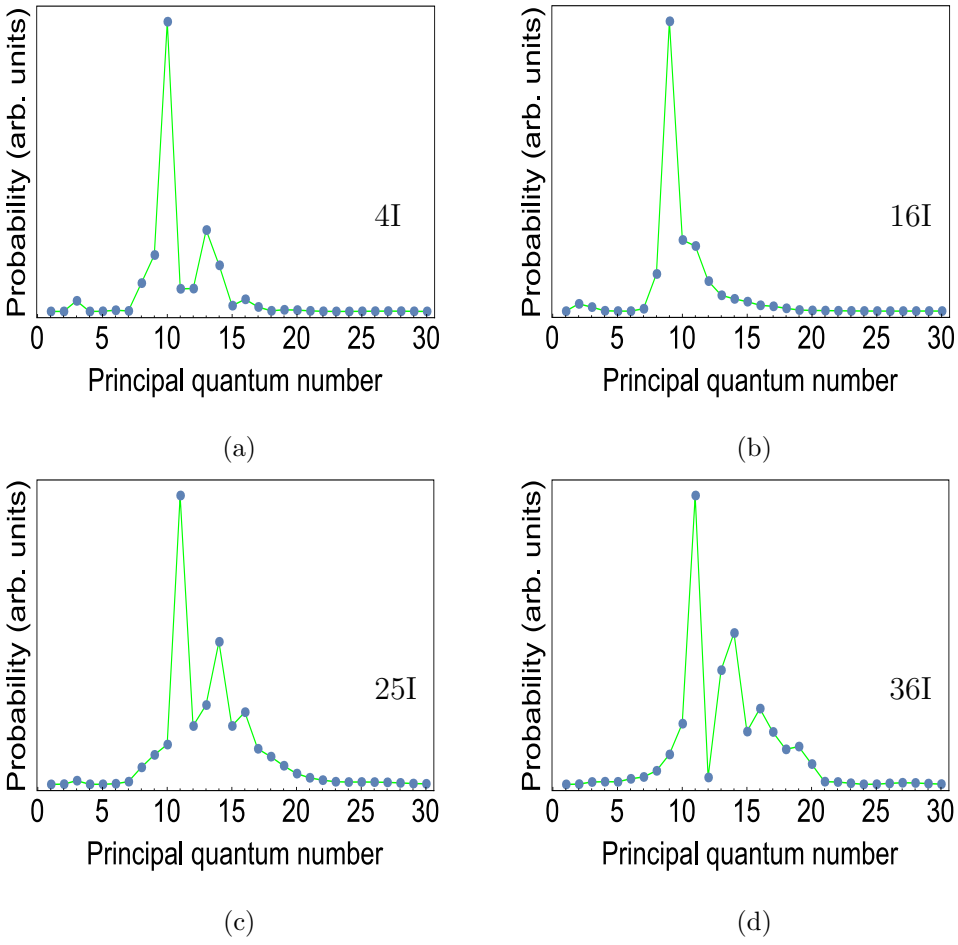

Figure 2.4. Survival probability distribution of H over each bound state for the launch energy relatively away from the first ($n = 2$) excited state. **(a)**, IR intensity is 4I, where $\mathrm{I} = 2.66 \times 10^{11}\mathrm{W/cm^2}$, and the initial launch energy $E = -0.093$ a.u. (marked by a vertical blue line in Fig. 2.2(a)). **(b)**, IR intensity is 16I, and $E = -0.082$ a.u.. **(c)**, IR intensity is 25I. $E = -0.073$ a.u.. **(d)**, IR intensity is 36I. $E = -0.0615$ a.u.. The energies are marked with vertical line in 2.2(a). For cases (a), (b), (c) and (d), the surviving probability all closely concentrates on the relatively high excited states (peak principal quantum number $n \sim 10$).

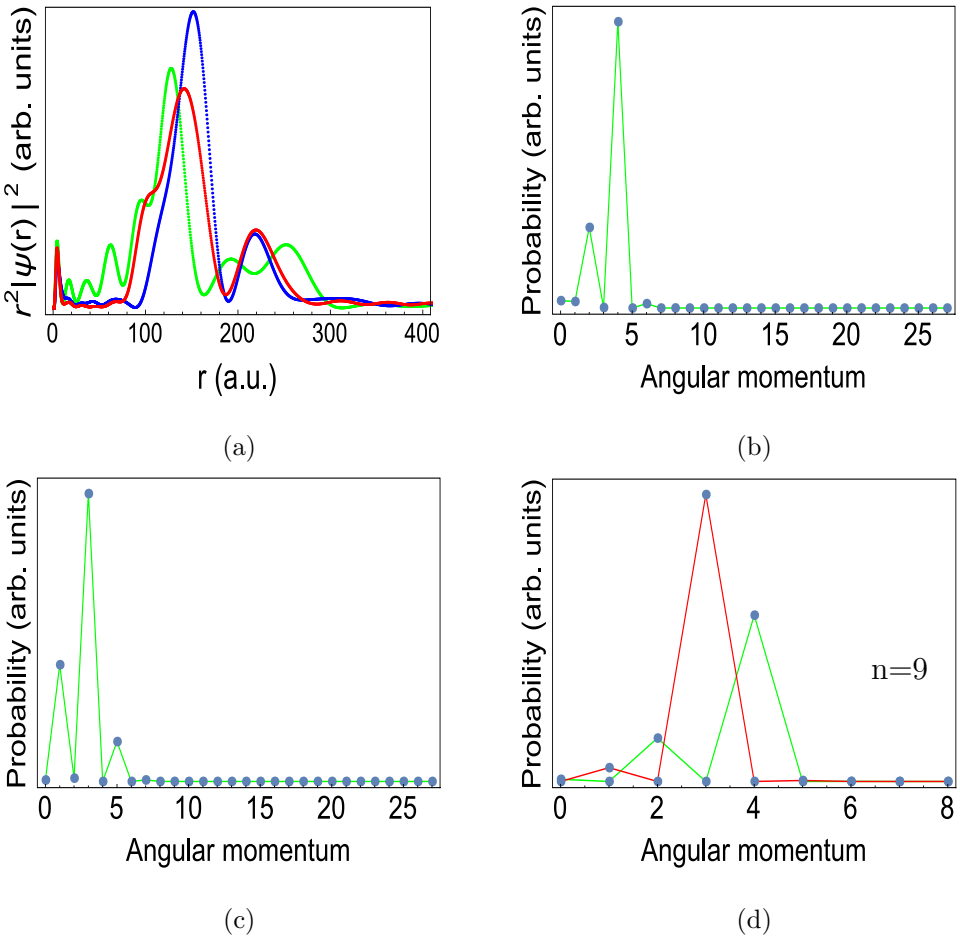

Figure 2.5. The survival probability distribution of H along the radial direction and over each orbital angular momentum. The IR intensity is 16I, where I = 2.66×10^{11}W/cm^2. **(a)** and the launch energy is E = −0.128 a.u.. The red, blue and green curves correspond to the distribution at three successive time after the IR field is off. **(b)** The survival probability over each orbital angular momentum for launch energy E = −0.128 a.u.. **(c)** The survival probability over each orbital angular momentum for launch energy E = −0.073 a.u.. **(d)** The survival probability over each orbital angular momentum with n = 9. The green and red lines correspond to launch energy E = −0.128 a.u. and E = −0.073 a.u. respectively.

those electrons get stuck at the first excited energy level, which is the reason why we see a big peak for $n = 2$ in Fig. 2.3(a). As we increase the IR intensity, the electrons can not stay there (n=2) anymore. Figure 2.3(b)-2.3(d) show the result with larger intensities, while the launch energy is still close to the first excited energy level. The probability distribution at each energy level indicates that most of the electrons that survive the IR field stay in highly-excited states (principal quantum number $n \sim 10$), with binding energy ten times smaller than one IR photon. The low-lying states contribute almost nothing to the survival probability. Figure 2.4 gives the results for a launch energy relatively far away from the first excited state. The survival probability peaks around the same highly-excited states ($n \sim 10$) for intensities 4I, 16I, 25I and 36I respectively. The IR duration is much longer than the Rydberg period ($T_{IR} > T_{Rydberg} \sim 2\pi n^3$) of the highly-excited states ($n \sim 10$), which indicates the electrons visit the core several times during the IR pulse.

Based on the above observation, the electron in highly excited states has a relatively high probability to survive, or we could say the atom becomes quasi-stable. In the process of time propagation, the electron can be directly excited to the quasi-stable states by the UV laser, or by absorbing integer number of IR photons after the UV laser excitation. Thus, one can imagine that electrons will have a higher probability to survive with initial energy which allows emission or absorption of an integer number of IR photons to reach the quasi-stable states. These initial energies of the electrons define the positions of the peaks in Fig. 2.2(b). In contrast, for electrons with other initial energies, it will be relatively easy to be ionized, because they can't reach the quasi-stable states through multiphoton processes during the IR interaction. In short, the quasi-stable states act like a safe harbor, which keeps the electron bound for a relatively long time. Admittedly, the harbor is not permanently safe. The electrons in the quasi-stable state still have probability to be ionized, which means the peaks in Fig. 2.2(b) will go lower and lower with increasing IR intensity or duration.

The probability distribution along the radial direction is also checked. In Fig. 2.5(a), the red, blue and green curves are picked at three successive time after the IR field is turned off. They show the radial probability distribution for IR intensity 16I and launch energy $E = -0.128$ a.u.. Refer to the result of Fig. 2.3(c), the state with principal quantum number $n \sim 9$ has the biggest probability. This corresponds to the outer radial turning point 160 a.u. ($r \approx 2n^2$). As shown in Fig. 2.5(a), the probability is centered around $r \sim 160$ a.u. for most of the time, and the structure persists even after hundreds of IR cycles, which obviously results from the electron staying in the safe harbor (the quasi-stable states) in the presence of IR field. Besides, we calculate the survival probability distribution over each orbital angular momentum, as shown in Fig. 2.5(b)-2.5(c) for launch energy $E = -0.128$ a.u. and $E = -0.073$ a.u. respectively. Figure 2.5(d) records the distribution with principal quantum number $n = 9$. In Fig. 2.5(b), the peaks at $l = 2, 4$ are due to the fact that the initial launch energy is three IR-photons away from the threshold. Thus, electrons survived at the quasi-stable states tend to have angular momentum $l = 0, 2, 4$ (The peak at $l = 0$ appears when using different IR intensity). The same argument applies to the result in Fig. 2.5(c).

In order to check that quasi-stability is not just for an atom with a pure Coulomb potential, a simulation of He atoms was also performed. In our calculation, the single active electron approximation was used, and the electron experienced a model potential given by Eq. (2.5). The eigen-energies were obtained by numerically diagonalizing the Hamiltonian without external fields. The model potential simulates the spin singlet of a He atom. It gives a $1s^2$ state with the bound energy $E \sim -0.736$ a.u., which deviates about 0.17 a.u. from the $1s^2$ state of the He atom. For the other states, the deviation is less than 0.1%. Similar to the case of the H atom, for each launch energy we measured their survival probability, and we also performed the projection of the final wave function to the bound states. The results are shown in Fig. (5.7). Figure 2.6(a) gives the result of survival spectra for IR intensities 16I, 25I, and 36I from the bottom to the top respectively. The IR-frequency-modulated peaks

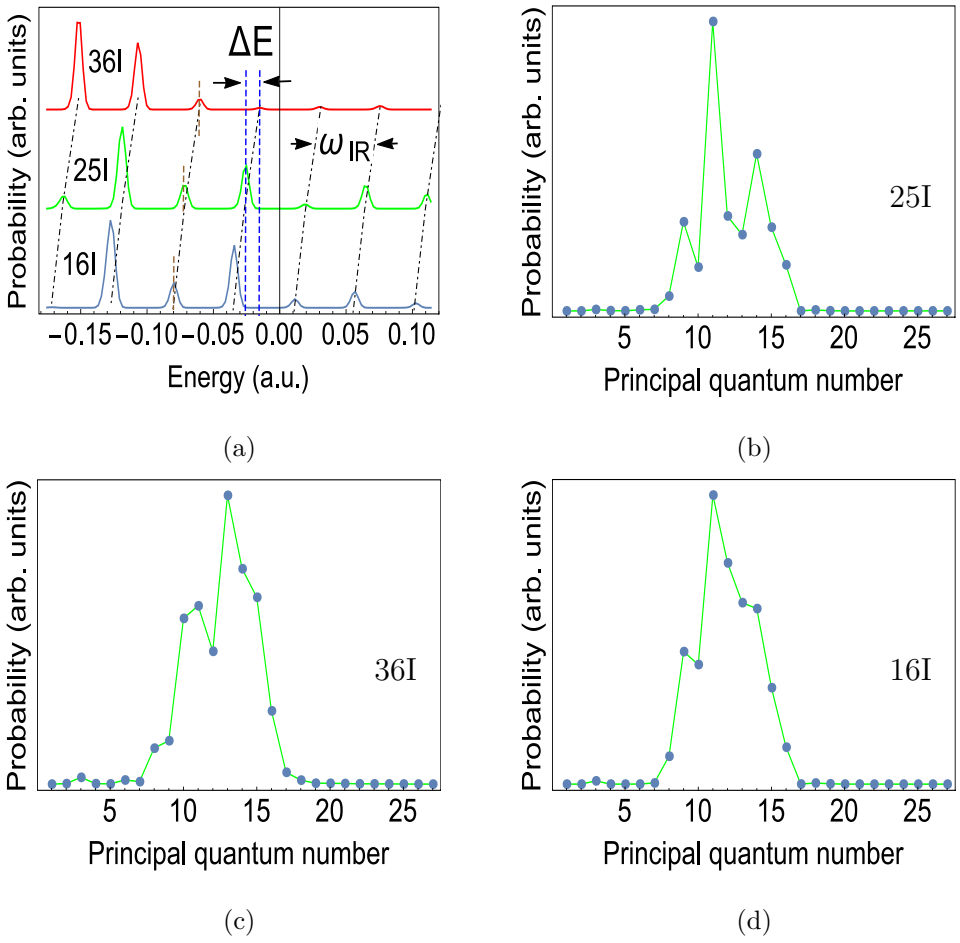

Figure 2.6. **(a)** Each curve records survival probability of He with principal quantum number n bigger than six. The Blue, Green and Red curves correspond to IR intensities 16I, 25I and 36I. The dotted (nearly vertical) curves help to track the right shifting of peaks. $\triangle E$ is the difference of peak shift for intensities 25I and 36I. **(b)** IR intensity is 25I, and the launch energy E = −0.072 a.u. (marked by a vertical brown line in Fig. 2.6(a)). **(c)** IR intensity is 36I. E = −0.063 a.u.. **(d)** IR intensity is 16I. E = −0.082 a.u.. (b), (c) and (d), give the probability distribution of He over each bound state, where electrons in the states with principal quantum number $n \sim 13$ are relatively stable.

can also be seen in each curve, and as the IR intensity increases, the whole set of peaks shifts to the right, with the amount determined by the difference of electron's ponderomotive energy. Figure 2.6(b)-2.6(d) show the projection results of final wave on to the bound states, where the peaks all focus around the state with principal quantum number $n \sim 13$. These high-lying states are the quasi-stable states, similar to what we discussed for the case of H atoms.

2.4 Summary and conclusion

In this chapter, we discussed the quasi-stability of H and He atoms in the presence of an intense IR field. The survival spectra and the population distribution in each bound state reveal how electrons survive the strong IR field. In the spectra, the peaks above the threshold are due to electrons launched in the continuum. Through the process of multi-photon assisted recombination [13, 14], those electrons could stimulatedly emit a certain number of IR photons, thus get caught by the core. Similar to that in the microwave experiments [7,8], the bound electron tends to stay in states with high principal quantum number, such that the electron spends a relatively long time away from the ion. Instead of being ionized, electrons away from the core only experience a ponderomotive quiver motion [8,23,27]. If the electron doesn't visit the core before the laser pulse is over, it must stay bound. However, in the present case the electron does visit the core since the Rydberg period of electrons is shorter than the IR field duration ($T_{Ryd} \sim 2\pi n^3 < T_{IR}$). The quasi-stability of the states shown in Fig. 2.2 persists even when we double the IR duration. This indicates that atoms in quasi-stable states can also survive collisions between the electron and the core. As a result, atoms in high-lying states become quasi-stable in the strong IR field. The quasi stability of atoms in an IR field is essentially the same as that in a microwave field [7] [8]. With the growing techniques of strong IR lasers, the phenomena discussed above could be investigated experimentally.

3. COHERENCE AND QUASI-STABLE STATES

In this chapter, we discuss the quasi-stability of UV-pulse-train-excited H atoms in a strong IR laser as a function of the phase delay of the UV-pulse-train relative to the IR laser [2]. The UV-pulse-train contains two frequency components. When the two components have frequencies separated by two IR photons, the population of surviving electrons is modulated by up to ten percent. When electrons are excited to right above or below the threshold, the survival probabilities have inverted phase delay dependence which can be explained classically. When the two frequencies are one IR-photon apart, the angular symmetry of the quasi-stable electrons is broken, and the asymmetry is also controlled by the phase delay. The asymmetrical distribution can be observed while the IR is on and smoothly evolves to a nonzero asymmetry that only weakly depends on the duration of the IR field.

3.1 Introduction

As discussed in the previous chapter, when highly excited atoms are exposed to an intense microwave or laser field, a certain fraction will stay bound for a long time [6–8, 13, 14], leading to their classification as quasi-stable states. Classically, the electrons in quasi-stable states derive their stability through orbiting in a weakly bound trajectory where they have little chance to absorb enough energy to escape [8,13,27]. These quasi-stable states can be studied spectrally, and a series of survival peaks can be detected [7,8]. These peaks are formed because electrons at the correct initial energy can reach the quasi-stable states through multi-photon transitions, while other initial energies will lead to ionization because the electron can not reach the quasi-stable state by absorbing integer number of photons.

As is well known, the properties of an excited electron wave packet in an intense IR field will differ depending on whether it was created by a single UV pulse or a train of them [28]. The properties of electrons excited by a single UV pulse are mainly determined by the IR intensity and frequencies. However, the behavior of electron wave packets produced by a UV-pulse-train is also affected by coherence, such as the large peak to peak modulation observed experimentally [28]. The coherence, timing, and varied energy of electrons could be controlled independently by changing the properties of the UV-pulse-train. A recent experiment can be seen in Ref. [29] for Li atoms in a microwave field, where they observed modulation of the population of weakly bound electrons by changing the delay in the pulse train and the detuning relative to threshold. Studying these features provides a novel, powerful tool to explore strong field interactions [28, 30].

In this chapter, we numerically study the survival probability of H in quasi-stable states as a function of the phase delay of a UV-pulse-train relative to an intense IR laser. The system is similar to the experiment [29], while we replace the microwave field by an intense IR field. The UV-pulse-train is created by combining two UV lasers with frequencies ω_1 and ω_2, as shown in Fig. 3.1(a). The phase delay between the pulse train and the IR laser is controlled by changing the initial phase of the two UV lasers. In our simulation, the two UV lasers are treated as two separate sources of excitation due to the linearity of the Schrödinger equation. Thus, a modulation by coherence in the survival probability is expected if the surviving electrons from each source have the same quantum numbers. This is satisfied when the two UV frequencies are separated by two IR photons ($\omega_2 - \omega_1 = 2\omega_{\mathrm{IR}}$), since the wave packets that reach the quasi-stable states will have the same even or odd parity [1]. In this case, a modulation of the population of weakly bound electrons is observed and is closely related to the phase delay. The peak to peak modulation in the survival probability varies for different launch energies. The launch energy is defined as the initial energy of electrons excited by the UV laser with frequency ω_1. When the launch energies are right above and below the threshold, the modulations are phase

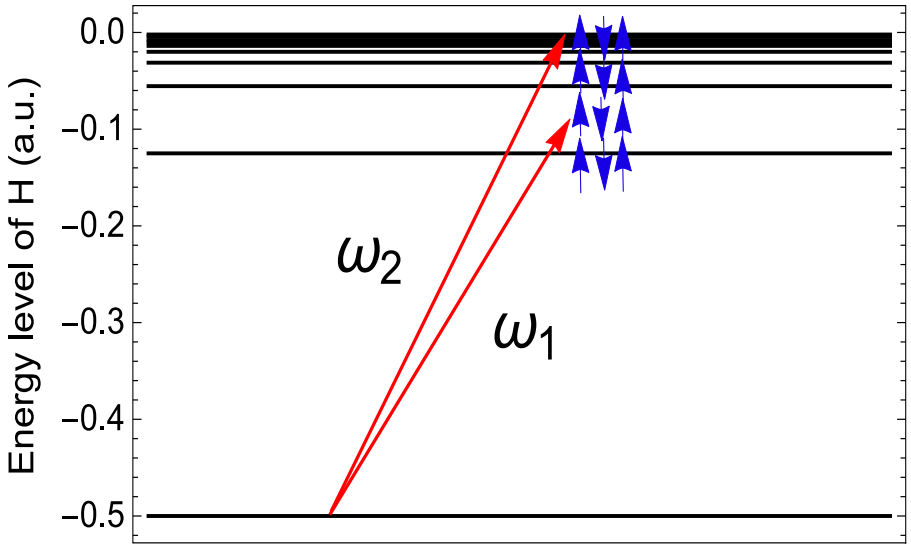

(a)

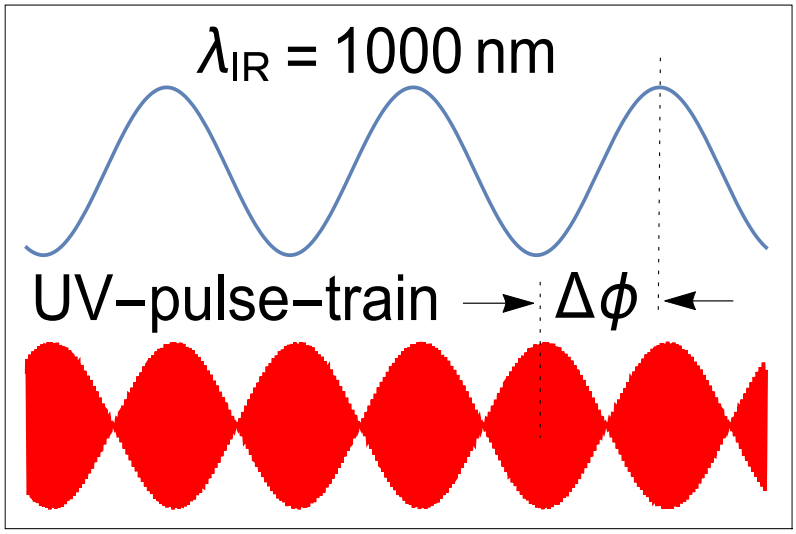

(b)

Figure 3.1. **(a)** Each black line corresponds to an energy level of the H atom. The red arrows show the electron being brought to the desired states by the UV lasers. Then the electron (blue arrows) continues evolving in the presence of the intense IR field plus atomic potential. **(b)** A sketch for the UV-pulse-train and IR field, where $\omega_2 - \omega_1 = 2\omega_{\mathrm{IR}}$. The IR laser lasts 1.6×10^4 a.u. in time. $\Delta\phi$ is the phase delay of the UV with respect to the IR.

inverted, which is the same as the experimental result in Ref. [29]. When the two UV frequencies are only one IR-photon apart ($\omega_2 - \omega_1 = \omega_{\rm IR}$), no coherence in the survival probability is seen. However, an interesting phenomenon is observed that the angular symmetry of the bound wave packet is broken and is also controlled by the phase delay. This asymmetrical distribution can be observed while the IR is on and smoothly evolves to a final value that only weakly depends on the IR duration. In the sections which follow, we introduce the numerical approach that we use, present the results and analysis, compare them to our expectations, and comment on their implications.

Similar to Chap. 2, we use atomic units except where explicitly stated otherwise.

3.2 Theory and method

In a simulation, H atoms were prepared in the ground state at the beginning. Then a weak UV-pulse-train was turned on to bring the electrons to the desired states through one-photon absorption. The UV-pulse-train was created by turning on two UV lasers with frequencies ω_1 and ω_2, as shown in Fig. (3.1). The beat frequency of the two lasers was assumed to be a multiple of an intense IR field so that the beats stay in phase with the IR over many cycles. After the UV pulse, the excited electrons continue to evolve in the presence of the intense IR field. The energy and angular momentum of the electrons change through multi-photon transitions. By tuning the initial phase of the UV lasers, the envelope of the UV-pulse-train can be shifted relative to the IR field. Figure 3.1(b) schematically shows the phase delay between the UV-pulse-train and the IR laser, where the UV frequency separation is two IR photons. In the simulation, the weak UV-pulse-train was treated as a source term in the Schrödinger equation. The duration of the pulse train should be short on the scale of the IR duration and long on the scale of one IR cycle. As long as this condition is satisfied, the actual duration of the pulse train becomes less important. In the simulation, we made the pulse train last about 4 IR cycles. The IR field lasted about

1.6×10^4 a.u. and its wavelength is 1000 nm, giving the frequency $\omega_{\mathrm{IR}} \sim 0.0455$ a.u.. The IR intensity was chosen to be I = 4.256×10^{12} W/cm^2. Similar to Ref. [1], the intensity was weak in the sense of affecting the H ground state, while strong in the sense of interacting with its excited states.

The dynamics is approximately governed by the following time dependent Schrödinger equation with a source term [1],

$$i\frac{\partial \Psi_e(\vec{r},t)}{\partial t} - \tilde{H}\Psi_e(\vec{r},t) = S(\vec{r},t), \tag{3.1}$$

where $\Psi_e(\vec{r},t)$ is the excited wave function of the electron after absorbing one UV photon and it is initially zero everywhere before the UV-pulse-train is on. The source term is

$$\begin{aligned} S(\vec{r},t) = \big\{ & F_{UV1}(t)\exp(-i(\omega_1 t + \sigma_1)) + \\ & F_{UV2}(t)\exp(-i(\omega_2 t + \sigma_2))\big\} z\Psi_g(\vec{r})\exp(-iE_g t), \end{aligned} \tag{3.2}$$

which provides the source of amplitude for the excited wave function. The UV lasers in the source take a Gaussian envelope, $F_{UV(1,2)}(t) \propto \exp(-t^2/2t_w^2)$ and t_w is chosen to make sure they last 4 IR periods in time. $\tilde{H}$ is the electron Hamiltonian without the UV interaction,

$$\tilde{H} = -\frac{1}{2}\nabla^2 + V(\vec{r}) - F_{\mathrm{IR}}(t)z, \tag{3.3}$$

where the third term is the interaction (using the dipole approximation) between the electron and the IR field (linearly polarized), and $V(r)$ is the interaction of the electron with the nucleus. $F_{\mathrm{IR}}(t)$ reads,

$$F_{\mathrm{IR}}(t) = F_m \cos(\omega_{\mathrm{IR}} t)\left(\mathrm{erf}[\frac{(t-t_i)}{t_w}] - \mathrm{erf}[\frac{(t-t_f)}{t_w}]\right). \tag{3.4}$$

The error function is used to smoothly turn on and off the IR laser. Noticing the linearity of Eq. (3.1), we can separate it into two parts, each of them treats only one UV laser. By doing this, the numerical calculation is greatly simplified. The excited wave function can be written as $\Psi_e(\vec{r},t) = \Psi_{e1}(\vec{r},t) + \Psi_{e2}(\vec{r},t)$. Thus the separated equations are

$$i\frac{\partial \Psi_{ei}(\vec{r},t)}{\partial t} - \tilde{H}\Psi_{ei}(\vec{r},t) = S_i(\vec{r},t), \tag{3.5}$$

in which

$$S_i(\vec{r},t) = F_{UVi}(t) z \Psi_g(\vec{r}) \exp(-i(E_g t + \omega_{UVi} t + \sigma_i)). \tag{3.6}$$

The index $i = (1,2)$. The phase delay of the UV-pulse-train relative to the IR can be changed by tuning σ_i (the initial phase of UV lasers).

The quantum simulation is performed by numerically solving Eq. (3.5). Each wave function is represented on a 2D space spanned by discrete radial points and an angular momentum basis. For the radial part, we use a nonlinear square root mesh. The propagation operator is constructed using a split-operator technique of the form,

$$U(\delta t) = U_1(\frac{\delta t}{2}) U_2(\delta t) U_1(\frac{\delta t}{2}), \tag{3.7}$$

where the approximation $U_i(\delta t) = (1 - iH_i\delta t/2)/(1 + iH_i\delta t/2)$ is used. During the time propagation, an absorbing potential is used, such that the ionized electrons are efficiently absorbed. One can refer to [25] for the details of the numerical technique. The final wave function in the quasi-stable states is obtained by adding Ψ_{e1} and Ψ_{e2}. In the sections that follow, one will see that most of the interesting effects are from the interference between these two wave packets.

3.3 Results and discussion

The UV-pulse-train was simulated by turning on two UV lasers which act as two independent sources in the system. In order to study the survival spectrum, the frequency of the first UV laser (ω_1) was scanned such that the electrons have initial energies ranging from $E = -0.17$ a.u. to $E = 0.11$ a.u. relative to the ionization threshold. For each frequency ω_1, the frequency of the second UV laser was tuned to satisfy $\omega_2 = \omega_1 + N \cdot \omega_{\mathrm{IR}}$ ($N = 1$ or 2). For each launch energy, the data was accumulated after the intense IR laser is smoothly turned off.

Refer to Eq. (3.5), the final wave function can be written as

$$\begin{aligned} \Psi_e(\vec{r},t) =& \Psi_{e1}(\vec{r},t) + \Psi_{e2}(\vec{r},t) \\ =& \psi_{e1}(\vec{r},t) \exp(-i\sigma_1) + \psi_{e2}(\vec{r},t) \exp(-i\sigma_2), \end{aligned} \tag{3.8}$$

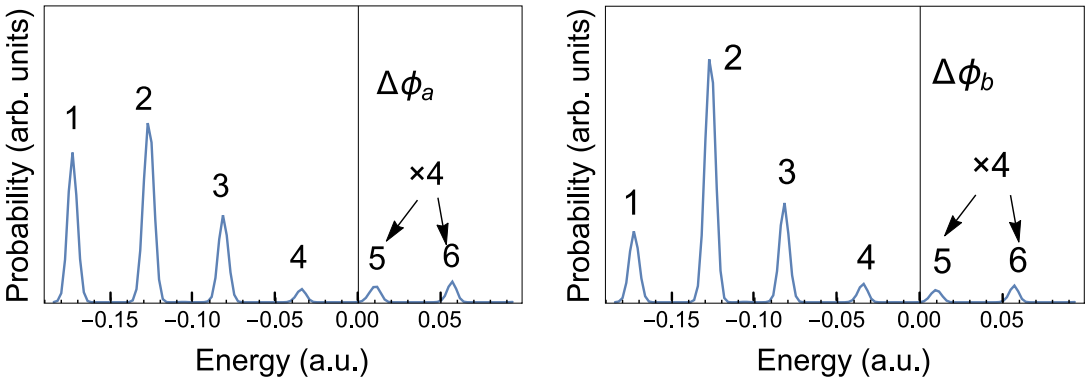

(a) (b)

Figure 3.2. The survival probability in quasi-stable states (with principal quantum number $n > 6$) as a function of the launch energies. Each figure has a given phase delay between the UV-pulse-train and the IR. The digits from 1 to 6 are to label each peak close to different launch energies. The peak 5 and 6 are multiplied by 4 to make them visible. Figure 3.2(a) and 3.2(b) are plotted in the same scale. **(a)** The phase delay is $\Delta\phi_a = \pi/2$. **(b)** The phase delay is $\Delta\phi_b = \pi$.

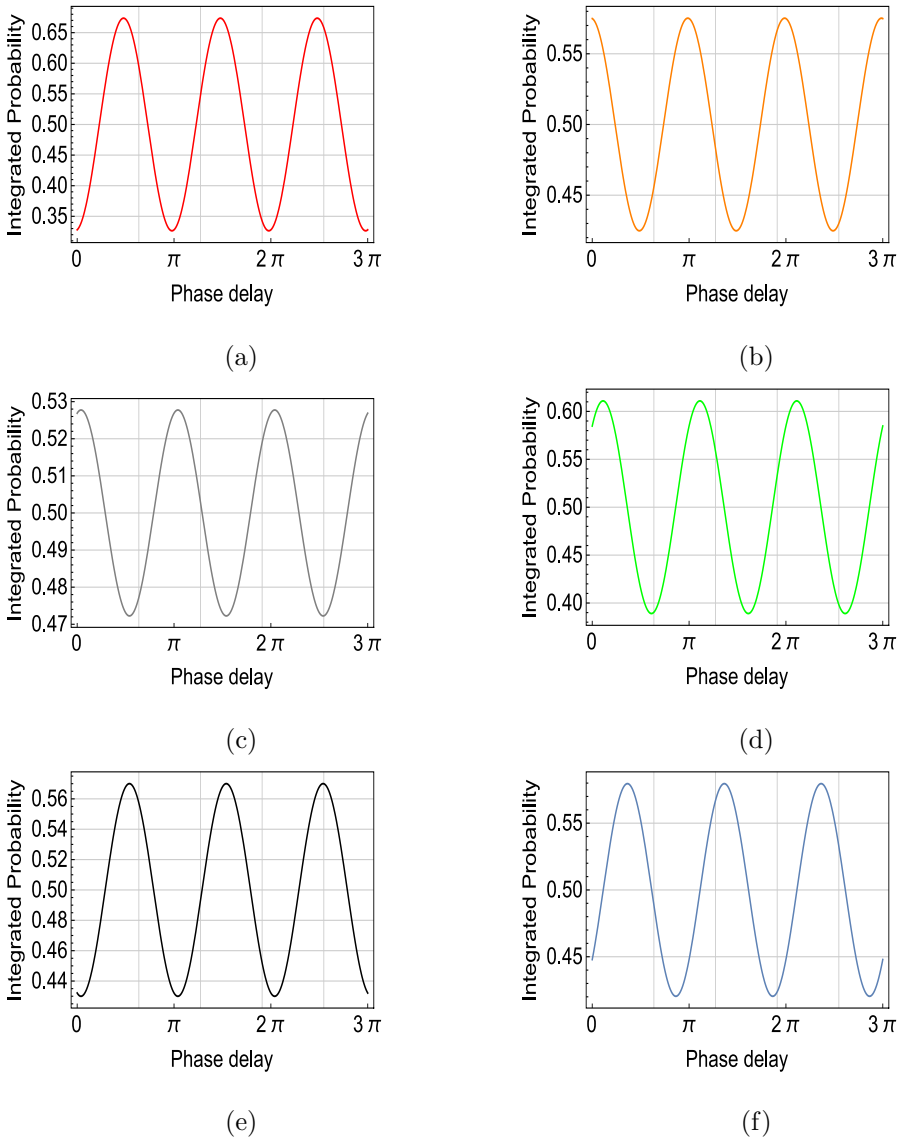

Figure 3.3. All the graphs record the integrated probability for each peak of Fig. 3.2 as a function of the phase delay of the UV-pulse-train relative to the IR. The integrated probability is obtained by integrating the survival probabilities of each peak in the spectrum of Fig. 3.2 and dividing it by twice its average over phase delay. The graph (a) corresponds to peak 1 in Fig. 3.2, (b) corresponds to peak 2 in Fig. 3.2, etc. All curves oscillate around 0.5. The bigger the oscillation is, the more the peak is in contrast with different phase delay.

where $\psi_{ei}(\vec{r},t)$ are the solutions to Eq. (3.5) when $\sigma_i = 0$ ($i = 1$ or 2). In principle, any observable $\hat{A}$ can be obtained through evaluating

$$\langle\hat{A}\rangle = \sum_{i=1}^{2}\langle\psi_{ei}|\,\hat{A}\,|\psi_{ei}\rangle + 2\mathrm{Re}\{\langle\psi_{e2}|\,\hat{A}\,|\psi_{e1}\rangle\exp(i(\sigma_2-\sigma_1))\}. \tag{3.9}$$

The second term shows clearly how the coherence is manifest in the value of an observable. By tuning the value of σ_i ($i = 1$ or 2), the phase delay of the UV-pulse-train relative to the IR laser will change accordingly, and so will the value of $\langle\hat{A}\rangle$. In the following subsections, observables $\hat{A} = \hat{I}$ and $\hat{A} = \cos\theta$ are discussed. They respectively correspond to the survival probability and orientation of electrons that survive the intense IR field. While the IR laser is on, the angular symmetry as a function of time is also discussed.

3.3.1 Coherence for two $\omega_{\mathbf{IR}}$ separation

Equation (3.9) gives the population of survival electrons when the observable $\hat{A} = \hat{I}$. The coherence in the survival population is greatly determined by the overlap $\langle\psi_{e2}|\psi_{e1}\rangle$. Since ψ_{e1} and ψ_{e2} are the electron wave functions in the quasi-stable states, they will have similar principal quantum numbers. Moreover they tend to have even (odd) angular quantum numbers if their initial energies are odd (even) number of IR-photon's away from the threshold [1]. When the two UV lasers have frequencies separated by two IR photons (N=2), they will create two electron wave packets with initial energies separated by two IR photons. As a result, ψ_{e1} and ψ_{e2} will concurrently have either odd or even angular quantum numbers when they reach the quasi-stable states. Thus, the overlap between ψ_{e1} and ψ_{e2} becomes significant, and coherence is expected in the electron's survival probability.

Figure (3.2) shows the survival spectrum for two different phase delays of the UV-pulse-train relative to the IR. The equally separated train of peaks is formed by electrons trapped in the quasi-stable states, which is discussed in Ref. [1, 7, 8]. The height of the peaks in the Fig. 3.2(a) and 3.2(b) are quite different, indicating the level of coherence in the electron population. Continuously changing the phase delay

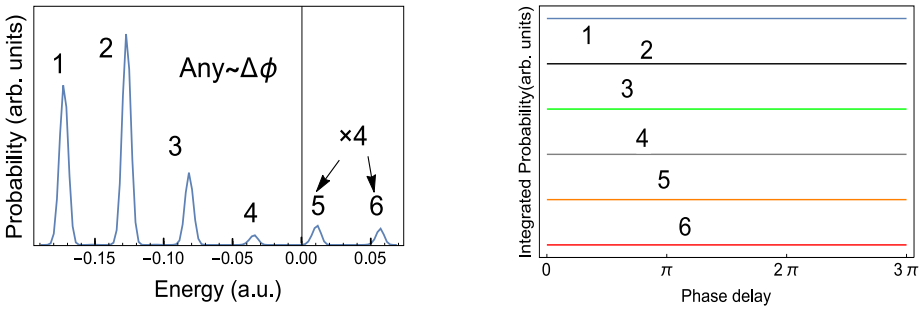

(a) (b)

Figure 3.4. The digits are used to track each peaks. The peak 5 and 6 are multiplied by 4 to make them visible. **(a)** The survival spectrum for the two components of the UV-pulse-train being separated by one IR photon. The shape of the spectrum keeps unchanged for any phase delay. **(b)** The straight lines denote the integrated survival probability of each peak in Fig. 3.4(a) in terms of the phase delay. Those lines are straight because no modulation is observed in this case.

will lead to a change in the interference term in Eq. (3.9). This phase sensitivity is an evidence that, after the UV excitation, most of the energy transfer from the IR to the excited electrons happens during the first few IR cycles, as suggested by the Simpleman's model [13, 14]. In order to clearly show this, for each phase delay, we integrate the survival probabilities of each peak in the spectrum and divide it by the twice average over phase delay. This quantity oscillates around 0.5, which contrast the survival probabilities of different phase delays. The result is shown in Fig. (3.3). Each line from 3.3(a) to 3.3(f) corresponds to each peak in Fig. 3.2 from the left to the right. Each curve is oscillating with a period of π in terms of phase delay. The period π is determined by the fact that the UV-pulse-train repeats itself when its envelope shifts by π. What is more, the survival probability of electrons with different launch energies have varied phase delay dependence. For those peaks right above and below the threshold, shown by the grey, green and black curves in Fig. 3.3, they tend to have inverted phase delay dependence, because of the fact that the ionization and recombination happens at the same time when electrons are tuned below or above the threshold. For those peaks far below the threshold, shown by the red curve, the phase delay dependence is not inverted compared to the above threshold curve, which is a topic that deserves further study.

3.3.2 Coherence for one $\omega_{\mathbf{IR}}$ separation

When the frequencies of the two UV lasers are separated by one IR photon (N=1), although ψ_{e1} and ψ_{e2} still have similar principal quantum numbers, they will have different parity (even for one and odd for the other) [1]. Thus, the overlap $\langle\psi_{e1}|\psi_{e2}\rangle$ is expected to be zero, indicating no coherence in the survival probability. As shown in Fig. 3.4(a), the height of the survival peaks remains the same for any phase delay of the UV-pulse-train relative to the IR. As a result, the integrated probability for each peak will approximately be a constant, which is shown by the horizontal lines in Fig. 3.4(b).

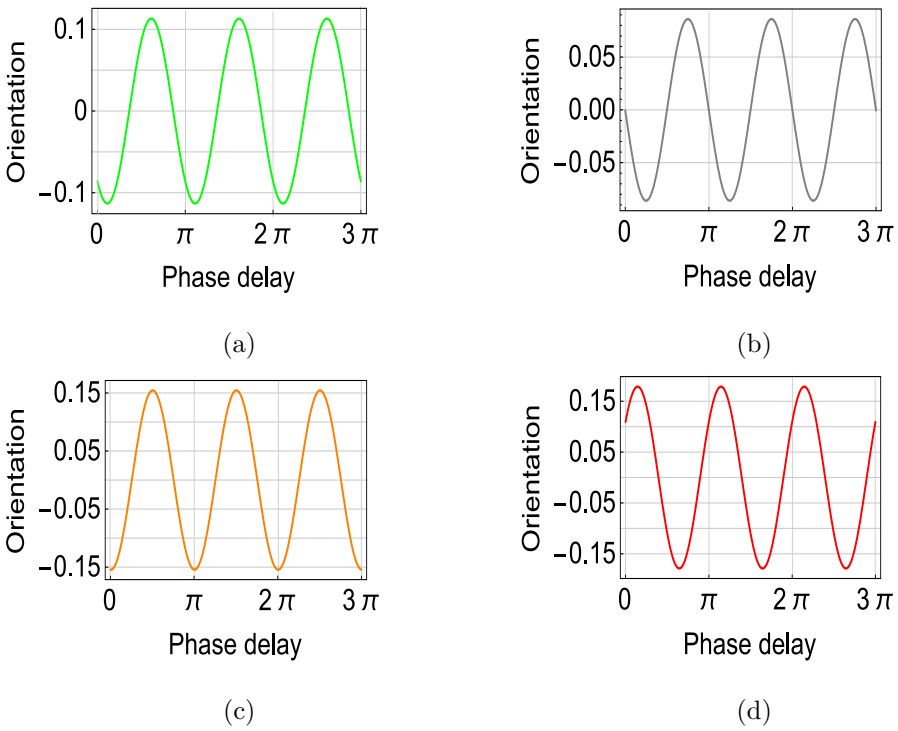

Figure 3.5. The orientation of the survival population as a function of the phase delay of the UV-pulse-train relative to the IR. The red (orange, gray, green) line is for the launch energy $E = 0.057$ a.u. ($E = 0.011$ a.u.,$E = -0.034$ a.u.,$E = -0.077$ a.u.). Each line is oscillating periodically around zero, indicating the phase delay is controlling the angular symmetry of the survival wave packets.

However, the parity difference of the two wave packets indicates an angular symmetry broken. The angular symmetry of an electron can be evaluated by the quantity (the orientation)

$$\text{Orientation} = \frac{\langle \Psi_e(\vec{r}) | \cos\theta | \Psi_e(\vec{r}) \rangle}{\langle \Psi_e(\vec{r}) | \Psi_e(\vec{r}) \rangle}, \tag{3.10}$$

where θ is the polar angle. Obviously, the orientation takes the value between $[-1, 1]$, and it being larger (smaller) than zero means the electrons are distributed more at the upper (lower) half sphere. From Eq. (3.9), when the observable $\hat{A} = \cos\theta$, the first term will vanish because the angular integral is nonzero only if the functions in the integral have angular quantum numbers differ by one ($\Delta l = \pm 1$). So the numerator in Eq. (3.10) simplifies to

$$\langle \cos\theta \rangle = 2\text{Re}(\langle \psi_{e2} | \cos\theta | \psi_{e1} \rangle \exp(i(\sigma_2 - \sigma_1))). \tag{3.11}$$

Thus, the orientation is also phase delay dependent. Meanwhile, $\langle \psi_{e2} | \cos\theta | \psi_{e1} \rangle$ is nonzero since the two wave packets exclusively have even or odd angular quantum numbers ($l = 1, 3, 5...$ for ψ_{e1}, then $l = 2, 4, 6...$ for ψ_{e2} or vice versa), which contributes to a nonzero integral. In Fig. (3.5), four different launch energies are shown. Each line records the orientation in terms of the phase delay. The oscillation of each line indicates that the surviving electrons' angular distribution switches between the upper and lower half sphere when continuously tuning the phase delay. Since the energy transfer from the IR to the electron (after excited) mostly happens at the first few IR cycles [14], the time of the electron being excited (controlled by phase delay) becomes crucial in determining the phase of the electron wave packets trapped at the quasi-stable states. As a result, tuning the phase delay will change the orientation, as indicated by Eq. (3.11). Figure (3.5) also reveals different phase delay dependence for varied launch energies. The below threshold behavior, shown by Fig. 3.5(a) and 3.5(b), has inverted phase delay dependence with respect to the above threshold behavior, shown by Fig. 3.5(d). However, they are not inverted with respect to Fig. 3.5(c), and more study is needed to understand this contrary result.

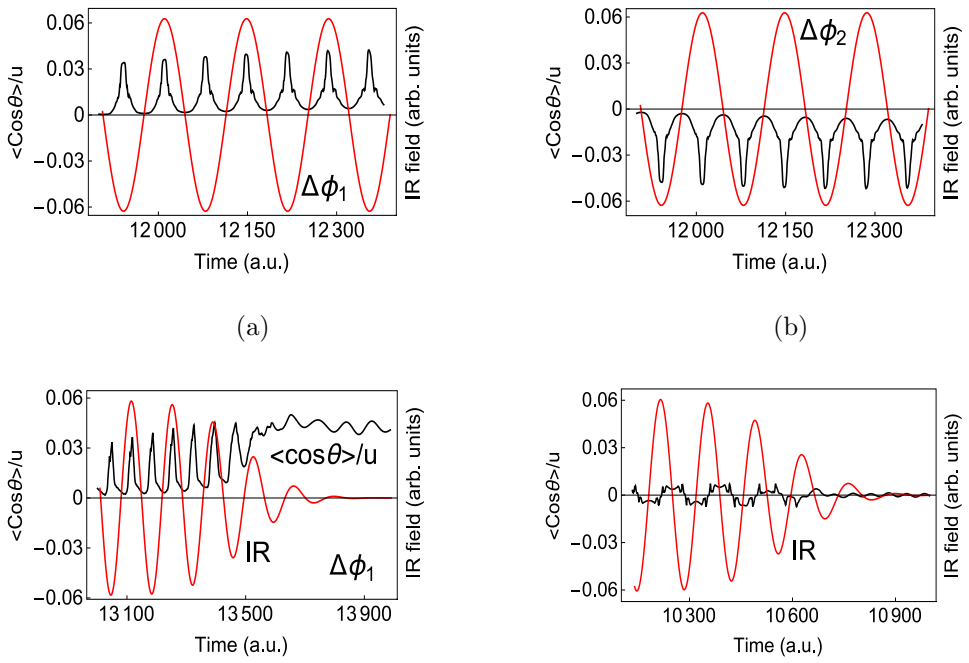

Figure 3.6. $\langle\cos\theta\rangle$ as a function of time while the IR is on (black lines). The plot is normalized by the final bound population (u= $\langle\Psi_e(\vec{r})|\Psi_e(\vec{r})\rangle$). The red curves are the IR. The launch energy $E = -0.082$ a.u. and $N = 1$ for Fig. 3.6(a) 3.6(b) and 3.6(c). **(a)** $\Delta\phi_1 = \pi/2$. **(b)** $\Delta\phi_2 = \pi$. **(c)** The IR field is being smoothly turned off, while $\langle\cos\theta\rangle$ stabilizes close to the peak value. **(d)** For $E = -0.127$ a.u. and the two laser has a frequency separation of $2\omega_{\rm IR}$, $\langle\cos\theta\rangle$ (black line) oscillates around zero and vanishes as the IR is turned off. Similar results apply to any phase delays.

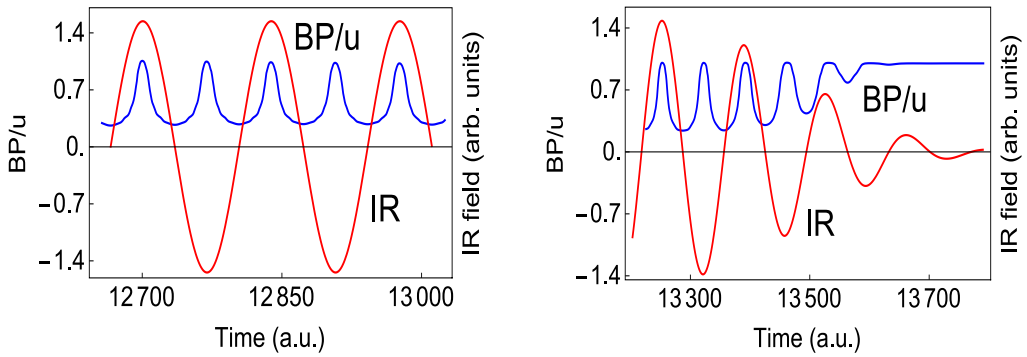

(a) (b)

Figure 3.7. The bound population (BP) of electrons ($\langle\psi_{e1}(t)|\hat{P}|\psi_{e1}(t)\rangle$). The plot (blue curve) is normalized by the final bound population (u= $\langle\psi_{e1}|\psi_{e1}\rangle$). The peak is going lower due to ionization. The launch energy $E = -0.082$ a.u.. The red curve is the IR field. **(a)** The IR is on. **(b)** The IR is being turned off.

We want to check the angular symmetry while the IR is still on. In the following discussion, we use the quantity $\langle\Psi_e(\vec{r},t)|\cos\theta|\Psi_e(\vec{r},t)\rangle$, which is time dependent since the IR is still on. First, $\langle\cos\theta\rangle$ is oscillating in time while the IR is on, as depicted by the black lines in Fig. 3.6(a) and Fig. 3.6(b). The cases shown in Fig. 3.6(a) and 3.6(b) have the same launch energy $E = -0.082$ a.u.. They have inverted angular distribution because their phase delays differ by $\pi/2$, which match the results in Fig. (3.5). The peak in the black line repeats every half of one IR cycle and follows the IR intensity. Also, when we smoothly turn off the IR field, $\langle\cos\theta\rangle$ stops oscillating and stabilizes near the peak value, as depicted in Fig. 3.6(c). In order to find the reason, we calculate $\langle\psi_{e1}(t)|\hat{P}|\psi_{e1}(t)\rangle$ as a function of time, where $\hat{P}$ is an projection operator to all bound states. Figure 3.7(a) reveals that the population of bound electrons also oscillates periodically while the IR is on. During each IR cycle, the electrons experience ionization and combination twice due to the ponderomotive motion, which is the reason for the periodical oscillation of $\langle\cos\theta\rangle$. As the IR is being turned off, shown in Fig. 3.7(b), the population of bound electrons stabilizes, which is the final amount of electrons that survive the IR laser. This amount of electrons contributes both to the maximal of $\langle\cos\theta\rangle$ while the IR is on and the stable value of it when the IR is off, as shown in Fig. 3.6(c).

Second, the final stable value of the orientation does not depend on the time of turning off the IR. Figure 3.6(c) shows the behavior of the orientation when the IR is being turned off at time $t = 13.5 \times 10^3$ a.u.. Similar behavior is observed when we turn off IR at other longer or shorter times, although the survival population varies. As a final point, we also calculate $\langle\cos\theta\rangle$ for $N = 2$. As expected, a symmetrical distribution ($\langle\cos\theta\rangle \sim 0$) is obtained for any phase delay. Fig. 3.6(d) shows that $\langle\cos\theta\rangle$ (black line) oscillates about zero while the IR is on and goes to zero when it is off. The magnitude of oscillation is approximately an order smaller than that in Fig. 3.6(c).

3.4 Conclusion

Quasi-stability of highly excited atoms in a strong field have been extensively discussed in the past fifty years [15–17]. Various mechanisms of stabilization and many related experiments can be found [19–24]. The fact that Rydberg atoms have lower chances to absorb energy keeps the electron bound for a relatively long time. Those surviving electrons, besides the same principal quantum number, tend to have the same even or odd (depending on the initial energy) angular quantum numbers [1]. Thus, a coherent effect is expected if electrons are being excited from different laser sources. The UV-pulse-train can be divided into two components, and they could separately act as a source, contributing electrons to the quasi-stable states.

In summary, we have studied the quasi-stability of UV-pulse-train-excited atoms in a strong IR field. When the two frequencies are separated by two IR photons, the survival probability will be a coherent superposition of the two contributions. By tuning the phase delay between the IR and the UV-pulse-train, we can coherently modulate the probability. The same coherence in the survival probability is not expected if the frequency separation is only one IR photon, where the survival probability is an incoherent addition of the two contributions. However, an asymmetry of the electron's angular distribution is observed in this case. By evaluating the orientation, we show the symmetry is oscillating as a function of the phase delay. And interestingly, the value of $\langle \cos\theta \rangle$ oscillates periodically in time while the IR is on. The period is half the IR cycle, and it stablizes after the IR is turned off. The oscillation of $\langle \cos\theta \rangle$ is due to the electrons experiencing recombination and ionization in each IR period, which is an interesting picture of quasi-stability in strong IR fields. With the growing techniques of attosecond physics [31], faster laser control and more accurate detection become possible. The above discussed coherence and angular distribution should be detectable in the lab. When studying pulse-train-excited atoms, the coherent effect shown above is surely of great importance to consider.

4. DECOHERENCE OF ROTATIONAL STATES

From this chapter, I start discussing the second part of the thesis. This chapter discusses the theory of decoherence for mesoscopic systems, which plays an important role in the fundamental problem of quantum-to-classical transitions. Back to the early age of quantum mechanics, people realized that there is an unclear boundary between quantum and classical physics, and it was vaguely said that the distinction is just the demarcation between the macroscopic and the microscopic. However, this answer is not satisfactory since the concept of macroscopic or microscopic is not well defined when we are dealing with real physical systems. In the past several decades, many new experimental results suggest the failure of the distinction. For example, superconducting Josephson junctions have quantum states associated with currents involving a huge number of electrons, while they could tunnel through the maxima of the effective potential [32]; Series of recent experiments has shown that molecules consisting of many atoms, such as fullerenes, can produce an interference pattern after traveling through a grating [33]. The size of the particle used in the interference experiments is still increasing, and even more strikingly, the theories of quantum superposition states of living organisms were recently reported [34] [35]. These experiments indicate that the macroscopic systems can not always be safely regarded as classical. Thus, a natural question, as raised by W. Zurek, is "where is the boundary of classical and quantum, or might there be no boundary at all" [36].

4.1 Introduction

Decoherence refers to the mechanism through which the classical world emerges from quantum systems in the sense of losing quantum coherence. The key point is that quantum systems in reality are never isolated from the environment. In this

case, we are not expecting the system to follow the Schrödinger equation, which only works for closed quantum systems. Due to the coupling with the environment, a system generally suffers from the loss of quantum coherence. The environment, usually with a huge number of degrees of freedom, is in some sense monitoring the system all the time, and the information of the system is gradually leaked into the environment, causing quantum decoherence. Mathematically, the ignorance of the environment requires us to trace out its degrees of freedom. Thus, the system we are interested in evolves in a way that the density matrix is quickly reduced to a classical mixed distribution.

In the past few decades, many environmental decoherence mechanisms have been proposed for a system's center of mass degree of freedom, such as air molecule collision, thermal radiation etc, where an exponential localized wave packet can be obtained. Detailed descriptions can be found in many literatures and books [10, 37–39]. While much work is devoted to the decoherence of the system's center of mass degree of freedom, little has been done for decoherence of its rotational degree of freedom. In a recent Ref. [40], Timo Fischer discussed the orientational decoherence through a Poisson process, and a orientational decoherence master equation is derived. In this thesis, I will mainly present our results based on scattering theory. With the growing interests in small system's internal degree of freedom, we believe that a general decoherence formalism for a system's rotational degree of freedom will be instrumental for future experiments.

4.2 The general theory of rotational decoherence due to scattering

We consider an object (system S) with only rotational degree of freedom interacting with its environment (environment E). As usual, the system and the environment are assumed initially uncorrelated. The combined system is described by

$$\rho_{(SE)} = \rho_{(S)} \otimes \rho_{(E)}, \tag{4.1}$$

where $\rho_{(E)}$ is the environment density operator. The system density operator $\rho_{(S)} = |\psi_S\rangle\langle\psi_S|$, where $|\psi_S\rangle = \oint C_\Omega |\Omega\rangle$ and $|\Omega\rangle = |\alpha, \beta, \gamma\rangle$. α, β, and γ are the Euler angles used to specify the configuration of the orientational state. In the following, we will show how correlation between the system and the environment is established from scattering events, which in the end leads to an exponential decay of the non-diagonal elements of system density matrix.

We first consider one single scattering event and confine our discussion to elastic collisions. $|\Omega\rangle = |\alpha, \beta, \gamma\rangle$ can be thought of a system $|0, 0, 0\rangle$ rotated by an operator

$$|\Omega\rangle = \hat{D}_S(\Omega)\,|0, 0, 0\rangle\,, \tag{4.2}$$

where $\hat{D}_S(\Omega) = \exp(-\frac{i}{\hbar}\hat{L}_z\alpha)\exp(-\frac{i}{\hbar}\hat{L}_y\beta)\exp(-\frac{i}{\hbar}\hat{L}_z\gamma)$. Now we denote the incoming particle by $|\chi\rangle$, Then the effect of the scattering event is formally described by the scattering operator $\hat{S}$ acting on the initial state,

$$|\Omega\rangle\,|\chi\rangle \to \hat{S}\,|\Omega\rangle\,|\chi\rangle\,. \tag{4.3}$$

Then we have,

$$\begin{aligned}
&\hat{S}\,|\Omega\rangle\,|\chi\rangle \to \hat{S}\hat{D}_S(\Omega)\,|0, 0, 0\rangle\,|\chi\rangle \to \hat{S}\hat{D}_S(\Omega)\,|0, 0, 0\rangle\,\hat{D}_E(\Omega)\hat{D}_E^\dagger(\Omega)\,|\chi\rangle \\
&\to \hat{S}\hat{D}_S(\Omega)\hat{D}_E(\Omega)\,|0, 0, 0\rangle\,\hat{D}_E^\dagger(\Omega)\,|\chi\rangle \to \hat{S}\hat{D}_{SE}(\Omega)\,|0, 0, 0\rangle\,\hat{D}_E^\dagger(\Omega)\,|\chi\rangle \\
&\to \hat{D}_{SE}(\Omega)\hat{S}\,|0, 0, 0\rangle\,\hat{D}_E^\dagger(\Omega)\,|\chi\rangle\,,
\end{aligned} \tag{4.4}$$

where $\hat{D}_E(\Omega)$ is the rotational operator of the environment. The last line used the fact that the scattering interaction is rotational symmetric. The next step is to include the non-recoil assumption, which states that the scattering event essentially does not disturb the system, except establishing entanglement between the system and the incoming particles [10, 39]. This assumption holds for the case that the system is much more massive than the incoming particle, and currently we restrict our discussion to this situation. After the action of the operator $\hat{S}$, the rotational state of the system remains as $|\Omega\rangle$. So, the above evaluation continues

$$\begin{aligned}
&\hat{D}_{SE}(\Omega)\,|0, 0, 0\rangle\,\hat{S}\hat{D}_E^\dagger(\Omega)\,|\chi\rangle \to \hat{D}_S(\Omega)\,|0, 0, 0\rangle\,\hat{D}_E(\Omega)\hat{S}\hat{D}_E^\dagger(\Omega)\,|\chi\rangle \\
&\to |\Omega\rangle\,\hat{D}_E(\Omega)\hat{S}\hat{D}_E^\dagger(\Omega)\,|\chi\rangle \to |\Omega\rangle\,\hat{S}(\Omega)\,|\chi\rangle \to |\Omega\rangle\,|\chi(\Omega)\rangle\,,
\end{aligned} \tag{4.5}$$

where $\hat{S}(\Omega) = \hat{D}_E(\Omega)\hat{S}\hat{D}_E^{\dagger}(\Omega)$. $|\chi(\Omega)\rangle$ is introduced to denote the state of the outgoing particle, which carries the information of the system. Equation (4.5) shows how the scattering event establishes correlations between the system and the environment particle. Accordingly, the initial separable density matrix of the combined system $\rho_{(SE)} = \rho_S \otimes \rho_{(E)}$ is transformed into the following entangled density matrix, expressed in the rotational configuration space,

$$\rho = \int d\Omega \int d\Omega' \rho_S(\Omega, \Omega') \left|\Omega\right\rangle \left\langle\Omega'\right| \otimes \left|\chi(\Omega)\right\rangle \left\langle\chi(\Omega')\right| . \tag{4.6}$$

The system we are interested in is described by the following reduced density matrix ρ_S, which is obtained by tracing over the environment,

$$\rho_S = tr_E(\rho) = \int d\Omega \int d\Omega' \rho_S(\Omega, \Omega') \left|\Omega\right\rangle \left\langle\Omega'\right| \left\langle\chi(\Omega')|\chi(\Omega)\right\rangle . \tag{4.7}$$

As a result, the evolution of the reduced density matrix due to the scattering event is

$$\rho_S(\Omega, \Omega') \to \rho_S(\Omega, \Omega') \left\langle\chi(\Omega')|\chi(\Omega)\right\rangle , \tag{4.8}$$

where $\langle\chi(\Omega')|\chi(\Omega)\rangle = \langle\chi|\hat{S}^{\dagger}(\Omega')\hat{S}(\Omega)|\chi\rangle$. Thus, a suppression is attached to the system density matrix element, and the value is determined by the average of the operator $\hat{S}^{\dagger}(\Omega')\hat{S}(\Omega)$ over the state of incoming particle.

4.2.1 Time evolution of the system density matrix elements

Recall the case for a symmetric system's translational degree of freedom [10, 39], the density matrix elements have a exponential decay in terms of time,

$$\rho(\vec{x}, \vec{x}', t) \propto \exp\left(-\kappa(\vec{x} - \vec{x}')^2 t\right)$$

with the decay rate depending on the scattering amplitude and the distance. For the decoherence of a system's rotational degree of freedom, it is reasonable to guess that the rate should depend on the orientational configuration difference. To confirm this, we need to evaluate the suppression in Eq. (4.8). The suppression of the system density matrix element is determined by the average of the operator $\hat{S}^{\dagger}(\Omega')\hat{S}(\Omega)$ in

terms of the environment particles. As usual, we first confine the environment particle in a box with a periodic boundary condition. The box volume has a finite value V and the momentum eigenstate is denoted by $|\vec{K}\rangle$. Later we push the box size to the limit of infinity, and the momentum eigenstate in this space is $|\vec{k}\rangle$. Considering the normalization condition, these eigenstates have the following simple connection

$$|\vec{K}\rangle = \left(\frac{(2\pi)^3}{V}\right)^{1/2} |\vec{k}\rangle\,. \tag{4.9}$$

Obviously, we have the relation

$$\begin{aligned} \sum_{\vec{K}} \delta(\vec{K}-\vec{K}') &= \int d^3\vec{k}\,\delta(\vec{k}-\vec{k}'), \\ \frac{(2\pi)^3}{V}\sum &= \int d^3\vec{k}. \end{aligned} \tag{4.10}$$

The state of the incoming particle is described by the density operator,

$$\rho_E = \frac{(2\pi)^3}{V}\sum \mu(k)\,|\vec{K}\rangle\,\langle\vec{K}|\,, \tag{4.11}$$

where the summation runs over the set of momenta that satisfy the periodic boundary condition. $\mu(k)$ is the momentum probability distribution. We assume the environment is spherically symmetric such that $\mu(k)$ depends only on the magnitude of the momentum. Then the average of the operator $\hat{S}^\dagger(\Omega')\hat{S}(\Omega)$ can be written as

$$\begin{aligned} &\langle\chi|\hat{S}^\dagger(\Omega')\hat{S}(\Omega)|\chi\rangle \to \frac{(2\pi)^3}{V}\sum \mu(k)\,\langle\vec{K}|\,\hat{S}^\dagger(\Omega')\hat{S}(\Omega)\,|\vec{K}\rangle \\ &\to \frac{(2\pi)^3}{V}\sum \mu(k)\,\langle\vec{K}|\,D_E(\Omega')\hat{S}^\dagger D_E^\dagger(\Omega')D_E(\Omega)\hat{S}D_E^\dagger(\Omega)\,|\vec{K}\rangle\,. \end{aligned} \tag{4.12}$$

In the following, we will denote the rotational operator of the environment by $D(\Omega)$. To proceed, the identity $\hat{S} = \hat{I} + i\hat{T}$ is used to express the scattering operator $\hat{S}$ in terms of $\hat{T}$ operator. So the above expression reads

$$\begin{aligned} &\to\frac{(2\pi)^3}{V}\sum \mu(k)\,\langle\vec{K}|\,D(\Omega')(\hat{I}-i\hat{T}^\dagger)D^\dagger(\Omega')D(\Omega)(\hat{I}+i\hat{T})D^\dagger(\Omega)\,|\vec{K}\rangle \\ &\to\frac{(2\pi)^3}{V}\sum \mu(k)\,\langle\vec{K}|\,\hat{I}-i\hat{T}^\dagger+i\hat{T}+D(\Omega')\hat{T}^\dagger D^\dagger(\Omega')D(\Omega)\hat{T}D^\dagger(\Omega)\,|\vec{K}\rangle \\ &\to 1-\frac{(2\pi)^3}{V}\int d^3\vec{k}\mu(k)\,\langle\vec{k}|\,\hat{T}^\dagger\hat{T}-D(\Omega')\hat{T}^\dagger D^\dagger(\Omega')D(\Omega)\hat{T}D^\dagger(\Omega)\,|\vec{k}\rangle\,, \end{aligned} \tag{4.13}$$

where $-i\hat{T}^\dagger + i\hat{T} = -\hat{T}^\dagger\hat{T}$, $\int d^3\vec{k}\mu(k) = 1$ and relation (4.9), (4.10) are used. The above expression can be written in a more symmetric form if we notice the fact that the operator ρ_E commute with the rotation $D(\Omega)$, resulting from the environment being spherically symmetric. [1] Thus we have

$$\begin{aligned}\rightarrow 1 - \frac{(2\pi)^3}{2V}\int d^3\vec{k}\mu(k)\langle\vec{k}|\,(D(\Omega)\hat{T}^\dagger D^\dagger(\Omega)D(\Omega)\hat{T}D^\dagger(\Omega) + D(\Omega')\hat{T}^\dagger D^\dagger(\Omega')D(\Omega')\hat{T}D^\dagger(\Omega') \\ - D(\Omega')\hat{T}^\dagger D^\dagger(\Omega')D(\Omega)\hat{T}D^\dagger(\Omega) - D(\Omega')\hat{T}^\dagger D^\dagger(\Omega')D(\Omega)\hat{T}D^\dagger(\Omega)\,|\vec{k}\rangle\,.\end{aligned} \tag{4.14}$$

We denote $\hat{T}_\Omega = D(\Omega)\hat{T}D^\dagger(\Omega)$, which is the rotated $\hat{T}$ operator. The above expression simplifies to

$$\begin{aligned}&\rightarrow 1 - \frac{(2\pi)^3}{2V}\int d^3\vec{k}\mu(k)\langle\vec{k}|\,\hat{T}^\dagger_\Omega\hat{T}_\Omega + \hat{T}^\dagger_{\Omega'}\hat{T}_{\Omega'} - \hat{T}^\dagger_{\Omega'}\hat{T}_\Omega - \hat{T}^\dagger_{\Omega'}\hat{T}_\Omega\,|\vec{k}\rangle \\ &\rightarrow 1 - \frac{(2\pi)^3}{2V}\int d^3\vec{k}'\int d^3\vec{k}\mu(k)\Big\{\langle\vec{k}|\,\hat{T}^\dagger_\Omega\,|\vec{k}'\rangle\langle\vec{k}'|\,\hat{T}_\Omega\,|\vec{k}\rangle + \langle\vec{k}|\,\hat{T}^\dagger_{\Omega'}\,|\vec{k}'\rangle\langle\vec{k}'|\,\hat{T}_{\Omega'}\,|\vec{k}\rangle \\ &\quad - \langle\vec{k}|\,\hat{T}^\dagger_{\Omega'}\,|\vec{k}'\rangle\langle\vec{k}'|\,\hat{T}_\Omega\,|\vec{k}\rangle - \langle\vec{k}|\,\hat{T}^\dagger_{\Omega'}\,|\vec{k}'\rangle\langle\vec{k}'|\,\hat{T}_\Omega\,|\vec{k}\rangle\Big\},\end{aligned} \tag{4.15}$$

where an identity operator $\hat{I} = \int d^3\vec{k}'\,|\vec{k}'\rangle\langle\vec{k}'|$ is inserted in the second step. Next, we connect the $\hat{T}$ operator with the scattering amplitude by the following familiar formula

$$\langle\vec{k}|\,\hat{T}_\Omega\,|\vec{k}'\rangle = -\frac{\hbar^2}{2\pi m}\delta(E-E')f_\Omega(k\hat{k}, k\hat{k'}). \tag{4.16}$$

Using the above formula, we have

$$\begin{aligned}\rightarrow 1 - \frac{(2\pi)^3}{2V}\int d^3\vec{k}'\int d^3\vec{k}\mu(k)\frac{\hbar^4}{(2\pi m)^2}\delta^2(E-E')\Big\{f^*_\Omega(\vec{k}',\vec{k})f_\Omega(\vec{k}',\vec{k}) + f^*_{\Omega'}(\vec{k}',\vec{k})f_{\Omega'}(\vec{k}',\vec{k}) \\ - f^*_{\Omega'}(\vec{k}',\vec{k})f_\Omega(\vec{k}',\vec{k}) - f^*_{\Omega'}(\vec{k}',\vec{k})f_\Omega(\vec{k}',\vec{k})\Big\}.\end{aligned} \tag{4.17}$$

The squared delta function can be evaluated by the following formula [39],

$$\delta^2(E'-E) = \frac{t}{2\pi\hbar}\delta(E'-E) = \frac{t}{2\pi\hbar}\frac{m}{\hbar^2 k}\delta(k'-k), \tag{4.18}$$

[1] This condition can be released if we remember the total rotation $D_{SE}(\Omega) = D_S(\Omega)D_E(\Omega)$ commutes with all operators. This is important for the later discussions, which treat the laser beam as a non-spherical environment.

where the parameter t is interpreted as the time when the interaction is on during the scattering event, and t is assumed to be much shorter than the system's decoherence time induced by a large amount of collisions [39]. Using Eq. (4.18) and integrate the magnitude of momentum k', we get

$$\begin{aligned}
&\to 1 - \frac{t}{2V}\int d^3\vec{k}'\int d^3\vec{k}\mu(k)\frac{\hbar}{mk}\delta(k-k')\Big\{f^*_\Omega(\vec{k}',\vec{k})f_\Omega(\vec{k}',\vec{k}) + f^*_{\Omega'}(\vec{k}',\vec{k})f_{\Omega'}(\vec{k}',\vec{k}) \\
&\quad - f^*_{\Omega'}(\vec{k}',\vec{k})f_\Omega(\vec{k}',\vec{k}) - f^*_{\Omega'}(\vec{k}',\vec{k})f_\Omega(\vec{k}',\vec{k})\Big\} \\
&\to 1 - \frac{t}{2V}\int dkk^2\mu(k)\frac{\hbar k}{m}\iint d^2\hat{k}d^2\hat{k}'\Big\{f^*_\Omega(k\hat{k}',k\hat{k})f_\Omega(k\hat{k}',k\hat{k}) + f^*_{\Omega'}(k\hat{k}',k\hat{k})f_{\Omega'}(k\hat{k}',k\hat{k}) \\
&\quad - f^*_{\Omega'}(k\hat{k}',k\hat{k})f_\Omega(k\hat{k}',k\hat{k}) - f^*_{\Omega'}(k\hat{k}',k\hat{k})f_\Omega(k\hat{k}',k\hat{k})\Big\}.
\end{aligned} \tag{4.19}$$

The integral can be further simplified. Since $f_\Omega(k\hat{k}',k\hat{k}) = f^*_\Omega(k\hat{k},k\hat{k}')$ and $k\hat{k},k\hat{k}'$ are symmetric in swapping the integral index, the integral of each term is real. It means $\iint d^2\hat{k}d^2\hat{k}'f^*_{\Omega'}(k\hat{k}',k\hat{k})f_\Omega(k\hat{k}',k\hat{k}) = \iint d^2\hat{k}d^2\hat{k}'f_{\Omega'}(k\hat{k}',k\hat{k})f^*_\Omega(k\hat{k}',k\hat{k})$. Thus the above formula can be expressed in a more symmetric form,

$$\to 1 - \frac{t}{2V}\int dkk^2\mu(k)\frac{\hbar k}{m}\iint d^2\hat{k}d^2\hat{k}'\Big|f_\Omega(k\hat{k}',k\hat{k}) - f_{\Omega'}(k\hat{k}',k\hat{k})\Big|^2. \tag{4.20}$$

Equation (4.20) gives the suppression of the system density matrix element by one scattering event, and it confirms our expectation that the result depends on the difference of the scattering amplitudes for different rotational configurations. Now we can proceed to derive the time evolution of the system density matrix. By substituting the above result into Eq. (4.8) and taking the limit $t \to 0$, the following formula is obtained

$$\frac{\partial\rho(\Omega,\Omega',t)}{\partial t} = -\Lambda\cdot\rho(\Omega,\Omega',t), \tag{4.21}$$

where $\Lambda = \frac{1}{2V}\int dkk^2\mu(k)\frac{\hbar k}{m}\iint\frac{d^2\hat{k}d^2\hat{k}'}{4\pi^2}|f_\Omega(k\hat{k}',k\hat{k}) - f_{\Omega'}(k\hat{k}',k\hat{k})|^2$. We call it decoherence rate which quantifies how fast the matrix elements decay. Eq. (4.21) describes the decoherence effect by one particle scattering. An ensemble of N incoming particles

will build up the decoherence effect, in a way that the decoherence rate is multiplied by the number of particle,

$$\Lambda = \frac{\Sigma}{2}\int dk k^2 \mu(k)\frac{\hbar k}{m}\int\int d^2\hat{k}d^2\hat{k}'\left|f_\Omega(k\hat{k}',k\hat{k}) - f_{\Omega'}(k\hat{k}',k\hat{k})\right|^2, \tag{4.22}$$

where $\Sigma = N/V$, which is the number density for the incoming particles. Thus, we derive the general expression for the localization rate of a quantum rotational system from the scattering model. Equation (4.21) and (4.22) are our main results in this section. The expression is general, since we have not specified the concrete form of the scattering amplitude. Taking into account the spherical symmetry of the environment, we could further simplify the Eq. (4.22). Denote the scattering amplitude as

$$f_\Omega(k\hat{k}',k\hat{k}) = D^\dagger(\Omega)f(k\hat{k}',k\hat{k})D(\Omega). \tag{4.23}$$

$f(k\hat{k}',k\hat{k})$ is the scattering amplitude for a configuration of the system, which could be initially chosen to be symmetrically aligned with the coordinate axis. Thus we have

$$\begin{aligned}
&\left|f_\Omega(k\hat{k}',k\hat{k}) - f_{\Omega'}(k\hat{k}',k\hat{k})\right|^2 \to \left(f^*_\Omega(k\hat{k}',k\hat{k}) - f^*_{\Omega'}(k\hat{k}',k\hat{k})\right)\left(f_\Omega(k\hat{k}',k\hat{k}) - f_{\Omega'}(k\hat{k}',k\hat{k})\right)\\
&\to D(\Omega)\Big(f^*(k\hat{k}',k\hat{k}) - D^\dagger(\Omega)D(\Omega')f^*(k\hat{k}',k\hat{k})D(\Omega')D^\dagger(\Omega)\Big)\Big(f(k\hat{k}',k\hat{k})\\
&- D^\dagger(\Omega)D(\Omega')f(k\hat{k}',k\hat{k})D^\dagger(\Omega')D(\Omega)\Big)D^\dagger(\Omega)\\
&\to D(\Omega)\left|f(k\hat{k}',k\hat{k}) - D^\dagger(\Omega)D(\Omega')f(k\hat{k}',k\hat{k})D^\dagger(\Omega')D(\Omega)\right|^2 D^\dagger(\Omega)
\end{aligned} \tag{4.24}$$

Using the above formula and the rotational symmetry of the environment, Eq. (4.22) can be written as

$$\Lambda = \frac{\Sigma}{2}\int dk k^2 \mu(k)\frac{\hbar k}{m}\int\int d^2\hat{k}d^2\hat{k}'\left|f(k\hat{k}',k\hat{k}) - D^\dagger(\omega)f(k\hat{k}',k\hat{k})D(\omega)\right|^2, \tag{4.25}$$

where we define $D(\omega) = D^\dagger(\Omega')D(\Omega)$, and ω can be interpreted as the absolute angle distance between two rotational configurations. Equation (4.25) shows that the decoherence rate only depends on the absolute difference of the configuration. This

could greatly simplify the future evaluation since we can always fix one configuration, from which the other configuration is rotated to by some absolute angles. In the following sections, we will test this theory by calculating the localization rate for two main source of decoherence: thermal photons and air molecules.

4.3 Localization due to scattering of thermal photons

We first consider a dielectric ellipsoid immersed in a photon-gas environment. Assuming black-body radiation at temperature T_E, the average number of photons with energy $\hbar ck$ per unit volume is given by the Planck distribution, thus the probability distribution of k with N photons in volume V is

$$\mu(k) = \frac{V}{N}\frac{2}{\exp(\frac{\hbar ck}{k_B T_E}) - 1}. \tag{4.26}$$

To get the decoherence rate, a key task is to evaluate the scattering amplitude difference. For a dielectric object, the cross section is determined by the scattered radiation from the induced dipole. Detailed discussion can be found in the text book [41]. If we have an incoming field $\vec{E}_{inc} = \vec{\xi} E \exp(-ik\hat{k}\cdot\vec{r})$ with a polarization vector $\vec{\xi}$, the far field approximation gives a scattering amplitude

$$f(k\hat{k}', k\hat{k}) = \frac{k^2}{4\pi\epsilon_0 E}\vec{\xi}'\cdot\vec{p}, \tag{4.27}$$

where $\vec{\xi}'$ is the polarization of the outgoing radiation, $\vec{p}$ is the induced dipole moment. The induced dipole moment is given by

$$\vec{p} = \bar{\bar{\alpha}}_\Omega \cdot \vec{E}_{inc}, \tag{4.28}$$

where $\bar{\bar{\alpha}}_\Omega$ is the polarizability of the ellipsoid with configuration $\Omega = (\alpha, \gamma, \beta)$. According to Eq. (4.25), we can simply choose a configuration with the semi-axis of the ellipsoid aligned with the coordinate axis, such that the polarizability is diagonal

$$\bar{\bar{\alpha}}_0 = \begin{pmatrix} \alpha_x & 0 & 0 \\ 0 & \alpha_y & 0 \\ 0 & 0 & \alpha_z \end{pmatrix}, \tag{4.29}$$

where the subscript means the Euler angles are zero for this situation. Then the polarizability with any configuration can be easily derived through the following rotation

$$\bar{\bar{\alpha}}_{\Omega'} = R^{-1}(\Omega')\bar{\bar{\alpha}}_0 R(\Omega'). \tag{4.30}$$

Now we are ready to calculate the difference of the scattering amplitude in Eq. (4.22). Through combining the Eqs. (4.27), (4.28), (4.29) and (4.30), we have

$$\left| f_\Omega(k\hat{k}', k\hat{k}) - f_{\Omega'}(k\hat{k}', k\hat{k}) \right|^2 = \frac{k^4}{(4\pi\epsilon_0)^2} \left| \vec{\xi}' \cdot (\bar{\bar{\alpha}}_0 - \bar{\bar{\alpha}}_{\Omega'}) \cdot \vec{\xi} \right|^2. \tag{4.31}$$

Thus, the integral becomes

$$\Lambda = \frac{\Sigma}{2} \int dk k^2 \mu(k) \frac{\hbar k}{m} \iint d^2\hat{k} d^2\hat{k}' \frac{k^4}{(4\pi\epsilon_0)^2} \left| \vec{\xi}' \cdot (\bar{\bar{\alpha}}_0 - \bar{\bar{\alpha}}_{\Omega'}) \cdot \vec{\xi} \right|^2. \tag{4.32}$$

Then we should average over the polarization direction of the incoming and outgoing field. The expression can be simplified by using the following useful identity

$$\sum_\lambda \xi_i^{(\lambda)} \xi_j^{(\lambda)} = \delta_{ij} - \hat{k}_i \cdot \hat{k}_j, \tag{4.33}$$

where $\{\vec{\xi}^{(1)}, \vec{\xi}^{(2)}, \hat{k}\}$ form a orthogonal basis set. Including the expression (4.26), we arrive at the final result

$$\Lambda = 6! \frac{c}{36\epsilon_0^2} \left(\frac{k_B T_E}{\hbar c} \right)^7 \zeta(7) \left(x^2 a_1 + y^2 a_2 + z^2 a_3 + xy a_4 + xz a_5 - yz a_6 \right), \tag{4.34}$$

where

$$\zeta(7) = \frac{1}{6!} \int_0^\infty d\chi \frac{\chi^6}{e^\chi - 1}$$

is the Riemann ζ-function for $n = 7$, c is the speed of light, and the other parameters are

$$\begin{cases} a_1 = 3 - 3\cos(2\alpha)\cos(2\gamma) - \cos(2\alpha)\cos(2\beta)\cos(2\gamma) + 4\cos\beta\sin(2\alpha)\sin(2\gamma), \\ a_2 = a_3 = 2 - \cos(2\beta), \\ a_4 = a_5 = 2\cos(2\alpha)\sin^2\beta + 2\cos(2\gamma)\sin^2\beta, \\ a_6 = 2\cos(2\beta), \\ x = \alpha_x - \alpha_y, \\ y = \alpha_x - \alpha_z, \\ z = \alpha_y - \alpha_z. \end{cases}$$

For a cylindrical symmetric ellipsoid, only one angle dependence is expected for the decoherence rate, and this emerges from the general expression. Consider a z axis cylindrical symmetrical ellipsoid, we have $\alpha_x = \alpha_y$. The above result can be reduced to

$$\Lambda = 6!\frac{2c}{9\epsilon_0^2}\left(\frac{k_B T_E}{\hbar c}\right)^7 \zeta(7)(\alpha_x - \alpha_z)^2 \sin^2\beta. \tag{4.35}$$

First, we see that the decoherence rate depends on the sine square of the angle, and it will get its maximal when $\beta = \pi/2$. This is reasonable because, as β increases, the configuration begins to repeat itself when β becomes larger than $\pi/2$. Second, the decoherence rate strongly depends on the thermal temperature. Increasing the temperature will greatly suppress quantum coherence. Also, we find that the temperature dependence for rotational decoherence is two powers lower in T_E than that for center of mass decoherence [39]. Third, if we continue setting $\alpha_x = \alpha_z$, the decoherence rate is zero, which is trivial because the scattering event can not distinguish the rotational state of a spherically symmetrical object.

4.4 Localization due to scattering of air molecules

In this section, we will consider the localization of a ellipsoidal system due to collision with air molecules. The air molecule is assumed to be in thermal equilibrium, which satisfy the Maxwell-Boltzmann distribution

$$\mu(k) = \left(\frac{\hbar^2}{2\pi m k_B T_E}\right)^{3/2} \exp(-\frac{\hbar^2 k^2}{2m k_B T_E}). \tag{4.36}$$

Refer to Eq. (4.25), a key part is to calculate the difference of scattering amplitude. In the current situation, we will adopt the Born approximation to evaluate the scattering amplitude. In the Born approximation, the scattering amplitude is given by the following formula

$$f(\vec{k}', \vec{k}) = -\frac{m}{2\pi\hbar^2}\int d^3\vec{r}\exp\left\{-i(\vec{k}' - \vec{k})\vec{r}\right\} * V(\vec{r}), \tag{4.37}$$

in which $V(\vec{r})$ is the potential of the system. In a real situation, the potential can be very complicated. Here, we consider a cylindrically symmetric ellipsoid which is modeled by the following potential

$$V(\vec{r}) = D^{\dagger}(\theta,\phi)V_0(\vec{r})D(\theta,\phi), \tag{4.38}$$

where $V_0(\vec{r}) = V_0 \exp\big\{-a(x^2+y^2)-bz^2\big\}$, with its symmetric axis placed at the z direction. The parameters a and b are positive and unequal. The symmetric axis of the potential $V(\vec{r})$ is in a direction determined by the polar and azimuthal angles (θ,ϕ). Since the system is cylindrically symmetric, only two Euler angles are enough to specify its rotational configuration. We first calculate the scattering amplitude Eq. (4.37) with the above potential $V(\vec{r})$. A convenient way to do the integral is in Cartesian coordinates. We first perform a coordinate rotation $O(x,y,z) \to \widetilde{O}(\tilde{x},\tilde{y},\tilde{z})$ to get $V(\vec{r}) \to \widetilde{V}(\vec{r})$, such that the symmetric axis of the potential $\widetilde{V}(\vec{r})$ is aligned with the $\tilde{z}$ axis, then calculate the integral in the $\widetilde{O}$ coordinate. The final scattering amplitude is obtained by rotating the integral result back to the original coordinate O. The scattering amplitude is given

$$f_{\theta,\phi}(\vec{k}',\vec{k}) = \frac{mV_0}{2\pi\hbar^2}\frac{\pi}{a}\sqrt{\frac{\pi}{b}}\exp\left\{-\frac{\widetilde{\Delta k_x}^2}{4a}-\frac{\widetilde{\Delta k_y}^2}{4a}-\frac{\widetilde{\Delta k_z}^2}{4b}\right\}, \tag{4.39}$$

where the vectors $\overrightarrow{\widetilde{\Delta k}} = (\widetilde{\Delta k_x},\widetilde{\Delta k_y},\widetilde{\Delta k_z})$ and $\overrightarrow{\Delta k} = (\Delta k_x,\Delta k_y,\Delta k_z)$ satisfy $\overrightarrow{\widetilde{\Delta k}} = R_y^{-1}(\theta)R_z^{-1}(\phi)\overrightarrow{\Delta k}$, and $\Delta k_i = k_i' - k_i$, $\widetilde{\Delta k_i} = \widetilde{k}_i' - \widetilde{k}_i$, $(i = x,y,z)$. Substituting Eq. (4.36) and Eq. (4.39) into Eq. (4.25), we get

$$\Lambda = \frac{32\pi}{15\hbar^8}\frac{N}{V}\sqrt{2\pi m^7(k_bT_E)^5}\frac{(a-b)^2V_0^2}{a^4b^3}\sin^2\theta. \tag{4.40}$$

First, we see that the decoherence rate only depends on the polar angle, which specifies the angle difference for current situation. Second, the parameter $\frac{(a-b)^2V_0^2}{a^4b^3}$ is determined by the size and geometry of the system particle. When we set $a = b$, the system becomes spherically symmetric, which reduces the decoherence rate to zero. Moreover, the rate has a dependence on the two and a half power of the temperature, which is one power higher than that for the case of center of mass decoherence [39]. The rate

is also proportional to environment particle density N/V, which is quite reasonable because higher density increases the scattering rate.

4.5 Summary and conclusion

One of the main features of decoherence of a quantum system is to take into account of the unavoidable environment interactions. For whatever quantum system, it will more or less suffer from the scattering with the environment, including thermal photons, air molecules, or even 3K cosmic background radiation etc [39]. These interactions produce a system-environment entanglement, which causes the system information to leak into the environment. This quantum to classical transition mechanism due to scattering not only works for the center of mass degree of freedom, but is also true for the system's rotational states.

In this chapter, we derived a general expression for the decoherence of a rotational quantum system. The decoherence rate depends on the difference of the scattering amplitude for different rotational configurations. To test the formula we obtained, we calculated the localization rate due to scattering of thermal photons and air molecules. The system is modeled as an ellipsoid, which is initially prepared in any quantum rotational superposition states. Our calculation shows that, for a given environment, the angular difference of the superposed states determines the decoherence rate. If we introduce a concept of angular distance, we may claim that the further the superposed states are distributed, the quicker the scattering will get them localized. The formalism developed in this chapter will be used to study heating and cooling of a laser levitated nanoparticle in the coming chapters.

5. CLASSICAL CALCULATION OF HEATING AND COOLING OF AN ELLIPSOIDAL NANOPARTICLE TRAPPED IN A LASER BEAM

In this chapter, we investigate heating and parametric feedback cooling of an optically trapped anisotropic nanoparticle in the laser-shot-noise-dominant regime. It is demonstrated that the related dynamical parameters, such as the oscillating frequency and shot noise heating rate, depend on the shape of the trapped particle. For an ellipsoidal particle, the ratio of the axis lengths and the overall size controls the shot noise heating rate relative to the frequency. For a particle with smaller ellipticity or bigger size, the relative heating rate for rotation tends to be smaller than that for translation indicating a better rotational cooling. For the parametric feedback scheme, we also present results on the lowest occupation number that can be achieved as a function of the heating rate and the amount of classical uncertainty in the position measurement.

5.1 introduction

As mentioned in the previous chapter, the transition between a quantum and a classical description of a system as its size is increased has been a problem since the birth of quantum mechanics [10, 37, 38, 42]. Understanding the behavior of increasingly large systems in terms of quantum mechanics is one of the motivations for investigating mesoscopic quantum phenomena [43,44]. In order to observe mesoscopic quantum coherence, a mesoscopic system needs to be cooled to the quantum regime and it should be well isolated from its environment such that the quantum coherence is not destroyed before any observation. Recently, laser levitated nanoparticles have

become a promising candidate to study mesoscopic quantum phenomena due to this system's favorable properties regarding decoherence and thermalization. [43, 45–48].

Despite the great advantage of laser levitation, the nanoparticle still suffers from shot noise due to photon scattering from the trapping laser. In ultrahigh vacuum, this shot noise is the dominant source of decoherence [11], which will lead to an increase in energy of the solid body degrees of freedom: the center of mass motion and the solid body rotations. Thus, in a laser levitated cooling experiment, the photon scattering, as an unavoidable factor, plays the role of setting a fundamental cooling limit to the system since the heating from shot noise will counteract whatever method is used to cool the nanoparticle.

Cooling and controlling the center of mass vibration of levitated nanoparticles have been discussed intensively in the past several years [49–52]. The interest in the rotational motion of a non-spherical nanoparticle is also increasing [3, 48, 53, 54]. The anisotropy of a dielectric nanoparticle has an orientation dependent interaction with a linearly polarized optical field which leads to a restricted, librational motion in some of the orientation angles when the laser intensity is large enough [55, 56]. The oscillating frequency of the rotational degrees of freedom can be much larger than that of the spatial degrees of freedom indicating that the rotational ground state can be reached at a higher temperature [48]. However, this feature does not guarantee that the ground state of the librational motion is easier to reach than that for the center of mass vibration. From our previous study [3], the decoherence rate due to shot noise in the rotational degrees of freedom was several orders of magnitude faster than that in the translational degrees of freedom for a nanoparticle interacting with blackbody radiation. The results from the previous chapter suggested that cooling the center of mass vibrations has a practical advantage over cooling the librational motion.

In this chapter, we investigate the shot noise heating and parametric feedback cooling [49] of a nano ellipsoid trapped in a linearly polarized laser beam. The nanoparticle is trapped in the center of the beam with its long axis closely aligned

with the laser polarization direction. Because the nanoparticle is nearly oriented with the laser polarization, the decoherence and shot noise heating rate of the librational motion is qualitatively changed from that for a nanoparticle interacting with blackbody radiation. The heating rate differs in the rotational and the translational degrees of freedom depending on the particle size and geometry. Importantly, we find that the relative rotational heating rate is slower than translation for a wide range of nanoparticle sizes and shapes, suggesting a better rotational than translational cooling. *However*, the preference for smaller relative heating rates becomes much less certain when classical feedback uncertainty is included in the calculation. By one measure, a lower optimal cooling limit can be reached for motions with a higher relative heating rate. Thus, the details of the limitations imposed by the classical measurement uncertainty will determine whether lower quantum numbers can be achieved for vibrations or librations. The results of the feedback cooling calculations are suggestive, instead of definitive, because they are based on classical mechanics. Quantum calculations with more realistic measurement assumption would allow for estimates of the feedback cooling limits [12, 57–60]. Although more computationally demanding, a quantum version of feedback cooling of levitated nanoparticles should be within reach. We leave that discussion for the next chapter.

5.2 Shot noise heating in a laser beam

We consider a nano ellipsoid with a size about 50 nm and mass m trapped in a linearly polarized laser beam, as shown in Fig. (5.1). The laser field is polarized in z and propagating in the positive y direction, which can be denoted by $\vec{E}_{inc} = \vec{\xi} E \exp(i\vec{k}_0 \cdot \vec{r})$, where $\vec{\xi}$, E and $\vec{k}_0 = k_0 \hat{y}$ are the polarization vector, the field magnitude and wave number respectively. The system is assumed to be well isolated from its environment and recoil from the elastically scattered photons is the major source of decoherence.

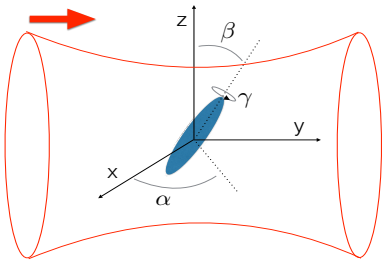

Figure 5.1. A symmetric ellipsoidal nanoparticle is trapped in a laser beam (shown by the red line), which is polarized in the z direction and propagating in the positive y direction (shown by the red arrow). Besides the vibrational motion in the center of mass degrees of freedom, the ellipsoid also rotationally vibrates with its long axis closely aligned with the laser polarization direction. The angles α, β, γ denote an orientation of the nanoparticle.

5.2.1 Shot noise in translational degrees of freedom

In order to compare the shot noise in rotation and translation, we first present the well known photon recoil heating of a trapped nanoparticle in its center of mass motion [11, 43]. Classically, the levitated nanoparticle experiences a momentum kick from each scattered photon [11], each of which gives an average recoil energy $\Delta E = \hbar^2 k^2/2m$ when the nanoparticle is much smaller than the wavelength of the light. The shot noise heating rate can be derived through multiplying the recoil energy by the momentum transfer cross section and the photon flux. Quantum mechanically, the interaction between the system and the incoming photons causes a decoherence in the system state [37], which generates a diffusion in momentum space. The classical and quantum mechanical treatments lead to the same shot noise heating rate. In the position basis, the master equation can be written as [10]

$$\frac{\partial}{\partial t}\rho(x,x') = -\Lambda(x,x')\rho(x,x'). \tag{5.1}$$

The unitary part of the time evolution is not shown in the above expression. $\Lambda(x,x')$ is the decoherence rate. In a long-wavelength approximation (which is a good approximation in the cases we consider), the decoherence rate $\Lambda = \mathscr{D}(x-x')^2$, where $\mathscr{D}$ is the momentum diffusion constant and it takes the form

$$\mathscr{D} = J_p \int d^3\vec{k}\mu(\vec{k}) \int d^2\hat{k}' \left| f(\vec{k},\vec{k}') \right|^2 \frac{k^2}{2} \left| \hat{k} - \hat{k}' \right|^2. \tag{5.2}$$

J_p is the photon flux, $\mu(\vec{k})$ is the incoming wave number distribution and $d\sigma/d\Omega = |f(\vec{k},\vec{k}')|^2$ is the differential cross section. $\vec{k}$ and $\vec{k}'$ are the incoming and outgoing wave vectors, respectively. The shot noise heating rate can be evaluated by the following formula

$$\dot{E}_T = \frac{d\langle \mathbf{H}_T \rangle}{dt} = \mathrm{tr}(\mathbf{K}_T \frac{\partial}{\partial t}\boldsymbol{\rho}), \tag{5.3}$$

where $\mathbf{H}_T = \mathbf{K}_T + \mathbf{V}_T$ denotes the system Hamiltonian and $\mathbf{K}_T = \mathbf{P}^2/2m$ is the free system Hamiltonian. The potential energy $\mathbf{V}_T$ is absent from the right hand side of

Eq. (5.3) since it has zero contribution after taking the trace. Combining the above equations, a straightforward calculation yields the following result

$$\dot{E}_T = J_p \int d^3\vec{k}\mu(\vec{k}) \int d^2\hat{k}' \frac{d\sigma}{d\Omega} \frac{\hbar^2 k^2}{2m} 2(1-\cos\theta), \tag{5.4}$$

where θ is the angle between the incoming and outgoing wave vector. Equation (5.4) gives the translational shot noise heating rate, which is exactly the same as what one would expect from a classical derivation [49].

In order to compare the above calculation with experimental results [11], Eq. (5.4) needs to be further evaluated. We are interested in the shot noise of a system coherently illuminated by a laser beam, so the incoming wave vector distribution can be approximated by

$$\mu(\vec{k}) = \delta(\vec{k} - \vec{k}_0), \tag{5.5}$$

in which $\vec{k}_0 = k_0\hat{y}$ is the incoming wave vector. If we denote ξ' as the polarization vector of the outgoing wave, the scattering amplitude can be written as [61]

$$f(\vec{k}', \vec{k}) = \frac{k^2}{4\pi\epsilon_0 E} \vec{\xi}' \cdot \vec{P}, \tag{5.6}$$

where $\vec{P} = \alpha \cdot \vec{E}_{inc}$ is the induced dipole moment. For now, we choose a spherical nanoparticle (a non-spherical particle is discussed below), such that the polarizability is a scalar

$$\alpha = 4\pi\epsilon_0 \left(\frac{\epsilon - 1}{\epsilon + 2}\right) r^3, \tag{5.7}$$

where r is the radius, ϵ and ϵ_0 are the relative and the vacuum dielectric constant respectively. Substituting the above equations into Eq. (5.4) and using the following well-known formula [62]

$$\sum_{\lambda=(1,2)} \epsilon_i^\lambda \epsilon_j^\lambda = \delta_{ij} - \hat{k}_i \hat{k}_j \tag{5.8}$$

to average the polarization of the outgoing wave, the shot noise heating rate is obtained

$$\dot{E}_T = \mathscr{D}\frac{\hbar^2}{m} = \frac{8\pi J_p}{3} \left(\frac{k_0^2}{4\pi\epsilon_0}\right)^2 \alpha^2 \frac{\hbar^2 k_0^2}{2m}. \tag{5.9}$$

Using the parameters in Ref. [11], the laser wavelength $\lambda = 1064$ nm, the particle mass of a fused silica of radius $r = 50$ nm is approximately 1.2×10^{-18} kg, the relative dielectric constant is about 2.1, and the photon flux J_p is equal to the laser intensity over the energy of a photon. The laser intensity at the focus is given by $I = Pk^2\mathrm{NA}^2/2\pi$. The laser power is $P = 70$ mW and NA = 0.9 is the numerical aperture for focusing [11] (These values are used throughout this chapter unless specified otherwise). Combining all of these factors, the translational shot noise heating rate is

$$\dot{E}_T \simeq 200 \text{ mK/sec}, \tag{5.10}$$

which matches well the experimental result in Ref. [11].

5.2.2 Shot noise in rotational degrees of freedom

Inspired by the experiment of laser trapping and cooling of non-spherical nanoparticles [48, 54], the master equation of rotational decoherence was studied for either mass particles or thermal photons scattered from an anisotropic system, and a squared sine dependence on the orientation difference was found in the angular localization rate [3, 53]. Similar to the momentum diffusion induced by the translational decoherence, the rotational decoherence generates an angular momentum diffusion, which was discussed for a spherically symmetric environment in Ref. [53]. Based on the rotational master equation, the time evolution of the expectation value of the angular momentum $\mathbf{J}$ was shown to be a constant, while the second moment of the angular momentum indeed follows the diffusion equation

$$\langle \mathbf{J}^2 \rangle_t = \langle \mathbf{J}^2 \rangle_0 + 4Dt, \tag{5.11}$$

where D is the diffusion coefficient determined by different types of scattering. The diffusion coefficients of Rayleigh-type and Van der Waals-type scattering were given in Ref. [53].

In this section, we discuss the rotational shot noise from photon scattering in a laser beam. The starting point is the master equation of rotational decoherence. As

shown in Fig. (5.1), the configuration of the ellipsoid can be described by its Euler angles $|\Omega\rangle = |\alpha, \beta, \gamma\rangle$ [3,53]. If we denote $\rho(\Omega, \Omega')$ as the density matrix of the system in the orientational basis, the time evolution follows the equation [3]

$$\frac{\partial}{\partial t}\rho(\Omega, \Omega') = -\Lambda(\Omega, \Omega')\rho(\Omega, \Omega'), \tag{5.12}$$

where

$$\Lambda = \frac{J_p}{2}\int d^3\vec{k}\mu(\vec{k})\int d^2\hat{k}'\left|f_\Omega(\vec{k}', \vec{k}) - f_{\Omega'}(\vec{k}', \vec{k})\right|^2 \tag{5.13}$$

is the rotational decoherence rate. Detailed discussion about the equation can be found in the previous chapter [3]. Similar to Eq. (5.3), the rotational shot noise heating can be obtained by evaluating

$$\dot{E}_R = \frac{d}{dt}\langle \mathbf{H}_R\rangle = \mathrm{tr}(\mathbf{K}_R\frac{\partial}{\partial t}\boldsymbol{\rho}), \tag{5.14}$$

where $\mathbf{H}_R = \mathbf{K}_R + \mathbf{V}_R$ is the rotational Hamiltonian, $\mathbf{V}_R$ is the potential energy which has zero contribution in the above equation, and $\mathbf{K}_R$ is the free rotational part. For a symmetric top, $\mathbf{K}_R$ takes the following form [63]

$$\begin{aligned}\mathbf{K}_R = -\frac{\hbar^2}{2I_1}\Big(&\frac{\partial^2}{\partial\beta^2} + \cot\beta\frac{\partial}{\partial\beta} + \Big(\frac{I_1}{I_3} + \cot^2\beta\Big)\frac{\partial^2}{\partial\gamma^2} \\ &+ \frac{1}{\sin^2\beta}\frac{\partial^2}{\partial\alpha^2} - \frac{2\cos\beta}{\sin^2\beta}\frac{\partial^2}{\partial\alpha\partial\gamma}\Big),\end{aligned} \tag{5.15}$$

where I_1 and I_3 are the moments of inertia of the ellipsoid along the short and long axis, respectively. To calculate the shot noise heating, the next step is to determine the decoherence rate Λ. As with the derivation of the translational shot noise, the distribution of the laser wave vector takes the delta function $\mu(\vec{k}) = \delta(\vec{k} - \vec{k}_0)$, where $\vec{k}_0$ is in the propagating y direction. The scattering amplitude is given by

$$f_\Omega(\vec{k}', \vec{k}) = \frac{k^2}{4\pi\epsilon_0 E}\vec{\xi}' \cdot \bar{\bar{\alpha}}_\Omega \cdot \vec{E}_{inc}, \tag{5.16}$$

where $\bar{\bar{\alpha}}_\Omega$ is the polarizability matrix for a specific configuration $|\Omega\rangle = |\alpha, \beta, \gamma\rangle$. If we place the ellipsoid symmetrically along the coordinate axis, the polarizability matrix will be diagonal

$$\bar{\bar{\alpha}}_0 = \begin{pmatrix} \alpha_x & 0 & 0 \\ 0 & \alpha_y & 0 \\ 0 & 0 & \alpha_z \end{pmatrix}, \tag{5.17}$$

where $\alpha_x = \alpha_y$ for a symmetric top. The polarizability with other rotational configuration can be derived through the following operation

$$\bar{\bar{\alpha}}_\Omega = R^\dagger(\Omega)\bar{\bar{\alpha}}_0 R(\Omega). \tag{5.18}$$

Combining the above equations and averaging over the polarizations of the outgoing wave using Eq. (5.8), the integral of Eq. (5.13) becomes

$$\begin{aligned}\Lambda = &\frac{J_p}{2}\frac{k_0^4}{(4\pi\epsilon_0)^2}\frac{2\pi}{3}(\alpha_z-\alpha_x)^2(1-\cos(2\beta)\cos(2\beta') \\ &-\cos(\alpha-\alpha')\sin(2\beta)\sin(2\beta')).\end{aligned} \tag{5.19}$$

The polarizability $\alpha_{x,z}$ should not be confused with the Euler angle α and α'. As expected, Λ differs from the decoherence rate from blackbody radiation given in the previous chapter [3]. The localization rate Λ depends on the orientations $|\Omega\rangle$ and $|\Omega'\rangle$ individually since the polarization of incoming photons is not isotropic. There is no dependence on γ because we're assuming a symmetric top. The localization rate depends only on the difference of the angle α because the photons are linearly polarized in the z-direction which does not have a preferential angle in the xy-plane.

For the cases considered below, we take the small oscillation approximation $\beta \ll 1$ which will be justified in the next section. (Unless specified otherwise, the symbol $\simeq$ in this chapter means this approximation is used.) Combining the Eqs. (5.12), (5.15) and Eq. (5.19), a direct evaluation of Eq. (5.14) yields the rotational shot noise heating rate

$$\dot{E}_R \simeq \frac{8\pi J_p}{3}\left(\frac{k_0^2}{4\pi\epsilon_0}\right)^2(\alpha_z-\alpha_x)^2\frac{\hbar^2}{2I_1}, \tag{5.20}$$

where terms of order β^2 have been dropped.

Table 5.1.
The parameters for three different nano-diamonds in a laser trap. The data is ordered for diamonds with decreasing ellipticity, while their sizes $\sqrt{a^2+b^2}$ are kept approximately the same. The trapping laser has wavelength λ = 1064 nm and power P = 70 mW.

$(a,b)/nm$	$\frac{\alpha_z-\alpha_x}{\alpha_z}$	$\omega_{\beta_1}/2\pi$	$\omega_x/2\pi$	$\omega_y/2\pi$	$\dot{E}_R$(mK/s)	$\dot{E}_T$(mK/s)	$\dot{E}_R/\dot{E}_T$	$\frac{\omega_{\beta_1}}{\omega_x}$	$\frac{\langle\dot{n}\rangle_R}{\langle\dot{n}\rangle_T}$	$\frac{\Delta n_R}{\Delta n_T}$
$(15,70)$	0.60	4.02 MHz	625 kHz	398 kHz	3.83×10^3	382	10.0	6.43	1.56	0.24
$(38,60)$	0.28	2.20 MHz	497 kHz	316 kHz	1.84×10^3	838	2.20	4.42	0.50	0.11
$(48,53)$	0.07	998 kHz	454 kHz	289 kHz	113	824	0.14	2.20	0.06	0.03

Table 5.2.
The parameters for three different nano-diamonds in a laser trap. The data is for diamonds with increasing size while fixing the ellipticity such that the ratio $(\alpha_z-\alpha_x)/\alpha_z$ stays approximately the same. The trapping laser has wavelength λ = 1064 nm and power P = 70 mW.

$(a,b)/nm$	$\frac{\alpha_z-\alpha_x}{\alpha_z}$	$\omega_{\beta_1}/2\pi$	$\omega_x/2\pi$	$\omega_y/2\pi$	$\dot{E}_R$(mK/s)	$\dot{E}_T$(mK/s)	$\dot{E}_R/\dot{E}_T$	$\frac{\omega_{\beta_1}}{\omega_x}$	$\frac{\langle\dot{n}\rangle_R}{\langle\dot{n}\rangle_T}$	$\frac{\Delta n_R}{\Delta n_T}$
$(27,42)$	0.28	3.14 MHz	497 kHz	316 kHz	1.23×10^3	292	4.22	6.31	0.68	0.11
$(38,60)$	0.28	2.20 MHz	497 kHz	316 kHz	1.84×10^3	838	2.20	4.42	0.50	0.11
$(49,78)$	0.28	1.68 MHz	497 kHz	316 kHz	2.46×10^3	1830	1.34	3.40	0.39	0.11

Table 5.3.
The parameters for three different fused silica in a laser trap. The data is for silica with different ellipticities, while their sizes $\sqrt{a^2+b^2}$ are kept approximately the same. The trapping laser has wavelength $\lambda = 1064$ nm and power $P = 70$ mW.

$(a,b)/nm$	$\frac{\alpha_z-\alpha_x}{\alpha_z}$	$\omega_{\beta_1}/2\pi$	$\omega_x/2\pi$	$\omega_y/2\pi$	$\dot{E}_R$(mK/s)	$\dot{E}_T$(mK/s)	$\dot{E}_R/\dot{E}_T$	$\frac{\omega_{\beta_1}}{\omega_x}$	$\frac{\langle\dot{n}\rangle_R}{\langle\dot{n}\rangle_T}$	$\frac{\Delta n_R}{\Delta n_T}$
$(15,70)$	0.30	1.90 MHz	419 kHz	267 kHz	119	48.6	2.45	4.52	0.54	0.12
$(38,60)$	0.13	1.17 MHz	388 kHz	247 kHz	93.2	197	0.47	3.01	0.16	0.05
$(48,53)$	0.03	549 kHz	374 kHz	238 kHz	6.50	240	0.03	1.47	0.02	0.01

Table 5.4.
The parameters for three different fused silica in a laser trap. The data is for silica with increasing sizes while the ellipticity is fixed such that the ratio $(\alpha_z-\alpha_x)/\alpha_z$ stays approximately the same. The trapping laser has wavelength $\lambda = 1064$ nm and power $P = 70$ mW.

$(a,b)/nm$	$\frac{\alpha_z-\alpha_x}{\alpha_z}$	$\omega_{\beta_1}/2\pi$	$\omega_x/2\pi$	$\omega_y/2\pi$	$\dot{E}_R$(mK/s)	$\dot{E}_T$(mK/s)	$\dot{E}_R/\dot{E}_T$	$\frac{\omega_{\beta_1}}{\omega_x}$	$\frac{\langle\dot{n}\rangle_R}{\langle\dot{n}\rangle_T}$	$\frac{\Delta n_R}{\Delta n_T}$
$(27,42)$	0.13	1.67 MHz	388 kHz	247 kHz	62.6	69.1	0.91	4.30	0.21	0.05
$(38,60)$	0.13	1.17 MHz	388 kHz	247 kHz	93.2	197	0.47	3.01	0.16	0.05
$(49,78)$	0.13	899 kHz	388 kHz	247 kHz	124	427	0.29	2.31	0.12	0.05

5.3 Relative cooling of the ellipsoid in the laser beam

There are several possible quantities that are useful when comparing the cooling of translation and rotation. The first one is the ratio of magnitudes of the translational and rotational shot noise, which is written as

$$\frac{\dot{E}_R}{\dot{E}_T} \simeq 5\left(\frac{\lambda}{2\pi\sqrt{a^2+b^2}}\right)^2 \frac{(\alpha_z-\alpha_x)^2}{\alpha_z^2}, \tag{5.21}$$

where the moment of inertia $I_1 = \frac{1}{5}m(a^2+b^2)$ with a and b being the short and long axis of the ellipsoid and $k_0 = 2\pi/\lambda$ are used. The polarizability can be determined by the formula [64]

$$\alpha_i = \epsilon_0 V \frac{\epsilon-1}{1+L_i(\epsilon-1)}, \tag{5.22}$$

where V is the particle volume, and ϵ is the relative dielectric constant. $L_{i=(x,y,z)}$ is determined by

$$\begin{aligned} L_x &= L_y = \frac{1-L_z}{2}, \\ L_z &= \frac{1-e^2}{e^2}\left(\frac{1}{2e}\ln\frac{1+e}{1-e}\right), \end{aligned} \tag{5.23}$$

where $e = \sqrt{1-a^2/b^2}$ is the ellipticity of the nanoparticle. Using the wavelength $\lambda = 1064$ nm and $\epsilon = 5.7$ for diamonds and $\epsilon = 2.1$ for silica, the rotational and translational shot noise and their ratios $\dot{E}_R/\dot{E}_T$ for several nano-diamonds and fused silica are given in Tab. 5.1, 5.2, 5.3 and 5.4 (For convenience, other related quantities are included in the tables). The geometries of the ellipsoids in the tables are chosen in a way such that their sizes $\sqrt{a^2+b^2}$ or ellipticities are approximately fixed. From the table, we see that the ratio $\dot{E}_R/\dot{E}_T$ differs depending on the ellipticity or size of the nanoparticle. More elongated or smaller ellipsoid tends to have higher shot noise heating in the rotational degrees of freedom, which suggests that particles with more spherical shape or bigger size may be better for rotational cooling.

The second useful quantity is the ratio of the rate of change of occupation number $\langle\dot{n}\rangle_R / \langle\dot{n}\rangle_T$, where $\langle n\rangle \equiv E/\hbar\omega$ is defined as the mean occupation number, and E and ω are the energy and the oscillating frequency in the corresponding degree of

freedom. For exploration of quantum phenomena, the occupation should be as small as possible. In order to get the ratio, it is necessary to analyze the mechanical motion of the nanoparticle in the laser trap. We consider an incident Gaussian beam which is z polarized and propagates in the y direction, as shown in Fig. (5.1). The detailed discussion of the Gaussian beam can be found in Ref. [49, 65]. The ellipsoid in the laser trap experiences a force and a torque

$$\begin{aligned} F_i &= \frac{1}{2}(\vec{P}\cdot\partial_i\vec{E}_{inc}), \\ M_i &= \frac{1}{2}(\vec{P}\times\vec{E}_{inc})_i, \end{aligned} \tag{5.24}$$

where no absorption is assumed such that the dipole moment $\vec{P}$ is real. For the center of mass motion, using the small oscillation approximation, the particle oscillates harmonically in the trap and each degree of freedom has an oscillating frequency,

$$\begin{aligned} \omega_x = \omega_z &\simeq \sqrt{\frac{\alpha_z}{m}}\frac{E_0}{w_0}, \\ \omega_y &\simeq \sqrt{\frac{\alpha_z}{2m}}\frac{E_0}{y_0}, \end{aligned} \tag{5.25}$$

where all corrections quadratic in the amplitude of oscillations have been dropped. $y_0 = \pi w_0^2/\lambda$, $w_0 = \lambda/(\pi \mathrm{NA})$ is the beam waist and E_0 is the field strength in the center of the laser focus. Similarly, for the rotational motion, due to the torque exerted on the particle, the long axis of the ellipsoid will tend to be aligned with the direction of the laser polarization, [1] as shown in Fig. (5.1). From the small oscillation approximation, the torsional oscillating frequencies can be written as

$$\omega_{\beta_1} = \omega_{\beta_2} \simeq \sqrt{\frac{\alpha_z - \alpha_x}{2I_1}}E_0, \tag{5.26}$$

where all corrections quadratic in the amplitude of oscillations have been dropped. The subindex β_1 and β_2 are used to denote the torsional vibration along the x and y axis, respectively. From the above equations, one finds that the ratio of torsional

[1] Strictly speaking, we are restricting the discussion to the case $I_3 \ll I_1 = I_2$, where the rotation in the symmetric degree of freedom is ignored. Or the symmetric rotation is small.

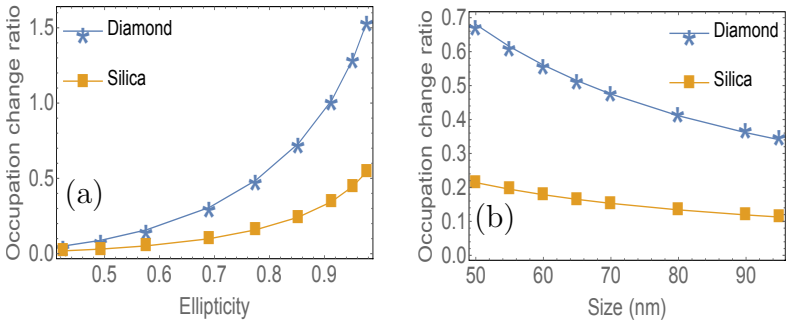

Figure 5.2. The ratio of the occupation number change $\langle \dot{n}_R \rangle / \langle \dot{n}_T \rangle$ in terms of ellipticity (**a**) and size (**b**). (**a**) The size of particles is fixed at $\sqrt{a^2+b^2}$ = 71 nm while the ellipticity increases. (**b**) The ellipticity is fixed at $e = 0.77$ while the particle size increases. The blue curves are for diamonds while the yellow curves are for silica.

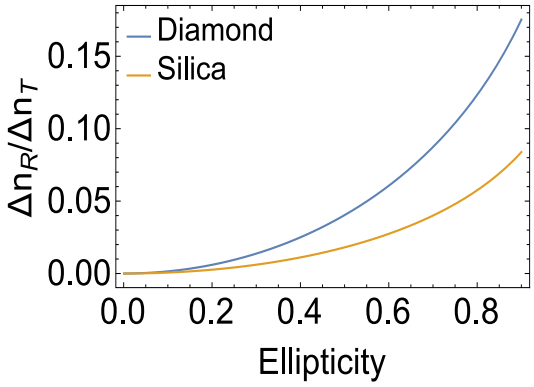

Figure 5.3. The ratio $\Delta n_R/\Delta n_T$ in terms of the particle ellipticity. The blue and yellow curves correspond to Diamond and Silica respectively.

oscillating frequency to the translational oscillating frequency is aproximately given by

$$\frac{\omega_{\beta_1}}{\omega_x} \simeq \frac{\sqrt{5}w_0}{\sqrt{2(a^2+b^2)}}\sqrt{\frac{\alpha_z-\alpha_x}{\alpha_z}}. \tag{5.27}$$

In an experiment, the beam waist is much bigger than the size of the particle, and the polarizability α_z and $\alpha_z - \alpha_x$ are roughly the same order, so the rotational oscillating frequency is generally higher than the translational oscillating frequency [48].

Thus, the ratio of the corresponding rate of change of occupation number is obtained

$$\frac{\langle \dot{n} \rangle_R}{\langle \dot{n} \rangle_T} \equiv \frac{\dot{E}_R/\omega_{\beta_1}}{\dot{E}_T/\omega_x} \simeq \frac{\lambda^2}{4\pi^2 w_0} \sqrt{\frac{10(\alpha_z - \alpha_x)^3}{(a^2+b^2)\alpha_z^3}}, \tag{5.28}$$

where the ratio is determined by the laser parameters, the particle size and the quantity $(\alpha_z - \alpha_x)/\alpha_z$ (determined by the particle ellipticity and dielectric constant). The ratios $\langle \dot{n} \rangle_R / \langle \dot{n} \rangle_T$ with respect to the particle ellipticity and size are given in Fig. (5.2). The blue and yellow curves are for diamonds and silica respectively. In Fig. 5.2(a), the particle size is kept fixed while we increase the ellipticity. As the particle shape approaches more spherical (ellipticity decreases), the ratio $\langle \dot{n} \rangle_R / \langle \dot{n} \rangle_T$ becomes smaller. In Fig. 5.2(b), we change the particle size while the particle ellipticity stays fixed. As the particle size increases, we see $\langle \dot{n} \rangle_R / \langle \dot{n} \rangle_T$ gets smaller. In addition, comparing the results for diamond and silica with the same geometries, we see that the ratio $\langle \dot{n} \rangle_R / \langle \dot{n} \rangle_T$ is generally smaller for silica. The reason is that $(\alpha_z - \alpha_x)/\alpha_z$ in Eq. (5.28) is smaller for particles with smaller dielectric constants and silica has a smaller dielectric constant than diamond. Intuitively, the ratio $\langle \dot{n} \rangle_R / \langle \dot{n} \rangle_T$ should be chosen as small as possible so as to get a better rotational cooling to the ground state. However, we will show later that the unavoidable measurement noise quantitatively modifies this expectation.

The third useful quantity is the ratio $\Delta n_R / \Delta n_T$, where $\Delta n \equiv 2\pi \dot{E}/\hbar\omega^2$ is the change in occupation number over one vibrational period in the corresponding degree of freedom. The ratio can be written as

$$\frac{\Delta n_R}{\Delta n_T} = \frac{\dot{E}_R/\omega_\beta^2}{\dot{E}_T/\omega_x^2} \simeq \frac{\lambda^2}{2\pi^2 w_0^2} \frac{\alpha_z - \alpha_x}{\alpha_z}, \tag{5.29}$$

which only depends on the laser parameters, the particle ellipticity and the particle dielectric constant. The ratios $\Delta n_R / \Delta n_T$ for diamond and silica with respect to the particle ellipticity are given in the tables and are plotted in Fig. (5.3). The curves show that the ratio increases with the particle ellipticity and also increases with the particle dielectric constant. This quantity is important and we will show in Sec.

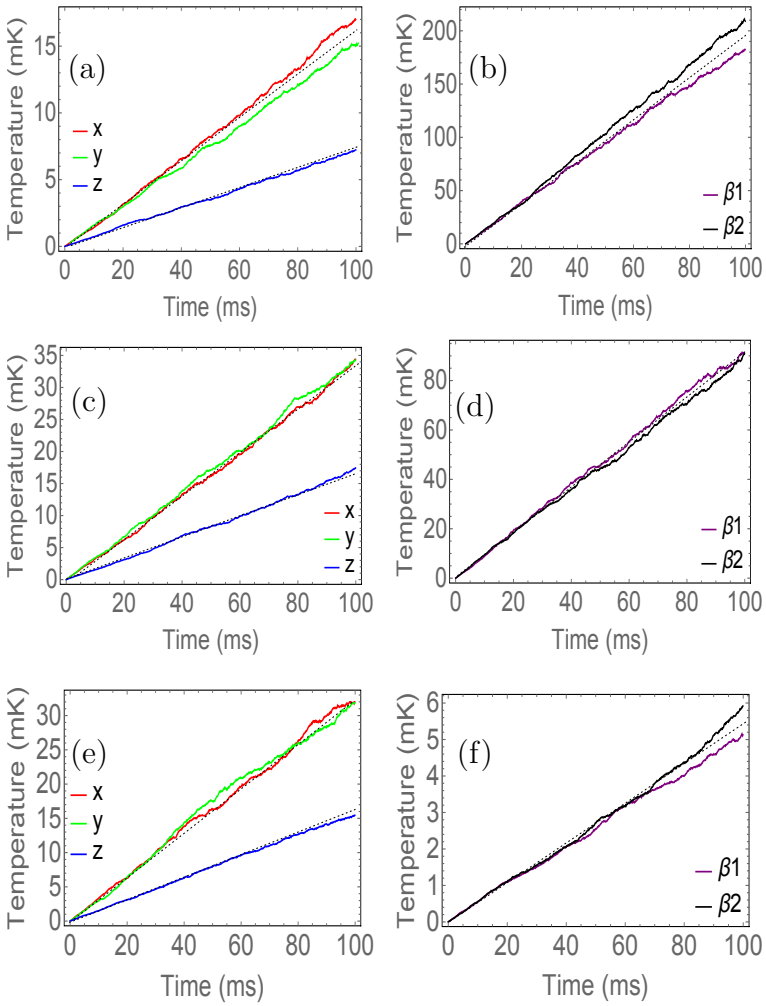

Figure 5.4. The classical simulation results of shot noise heating for nanodiamonds in both the translational and rotational degrees of freedom. Each curve is averaged over 400 individual reheating trajectories. **(a)** and **(b)** are for the nanoparticle with half axes ($a = 15$ nm, $b = 70$ nm), while **(c)** and **(d)** with half axes ($a = 38$ nm, $b = 60$ nm), **(e)** and **(f)** with half axes ($a = 48$ nm, $b = 53$ nm). The dashed lines are the heating curves $T = T_0 + \dot{E}t$ with T_0 the initial temperature and $\dot{E}$ the corresponding heating rate from Tab. 5.1.

5.5 that this quantity actually controls the classical dynamics during the feedback cooling.

The above equations are based on a small oscillation angle approximation. In a cooling experiment, the maximal oscillation angle can be estimated by

$$\beta_{max} \simeq \sqrt{\frac{2k_B T}{I_1 \omega_\beta^2}}, \tag{5.30}$$

where k_B is the Boltzmann constant and T denotes the temperature. Using the data ($a = 48$ nm, $b = 53$ nm) from Tab. 5.1 and 5.3, we find that the maximal angle spread is still small ($\beta_{max} \simeq 10^{-3}$ rad for diamond, $\beta_{max} \simeq 10^{-2}$ rad for silica) at $T = 0.1$ K. For higher oscillating frequencies and lower temperature, the maximal angle spread β_{max} will be even smaller.

5.4 Simulation of shot noise heating and feedback cooling

Parametric feedback cooling is discussed in Ref. [49], where a single laser beam is used for both trapping and cooling. The spatial motion of a nanoparticle is cooled from room temperature to subkelvin, and the quantum ground state cooling is also suggested with the same cooling mechanism. In this parametric feedback scheme, a signal at twice the oscillation frequency is obtained by multiplying the particle's position with its first time derivative $x(t)\dot{x}(t)$. This information is then fed back to the system, which leads to a loop that on average acts as a drag on the particle. The parametric cooling works by simply modulating the intensity of the trapping laser, and this scheme is extremely suitable for rotational cooling since it avoids relatively complex operations if one tries to feedback torque. In this section, the feedback cooling calculations are based on ideal assumptions about measuring the nanoparticle's position and orientation. The discussions of feedback cooling with the measurement uncertainty are given in the next section.

Combining the translational and rotational motion, the classical dynamics of the ellipsoid is governed by

$$\begin{aligned} m\frac{d^2 x_i}{dt^2} &\simeq -m\omega_i^2(1+\Delta)x_i, \\ I_1\frac{d^2 \beta_j}{dt^2} &\simeq -I_1\omega_{\beta_j}^2(1+\Delta)\beta_j. \end{aligned} \tag{5.31}$$

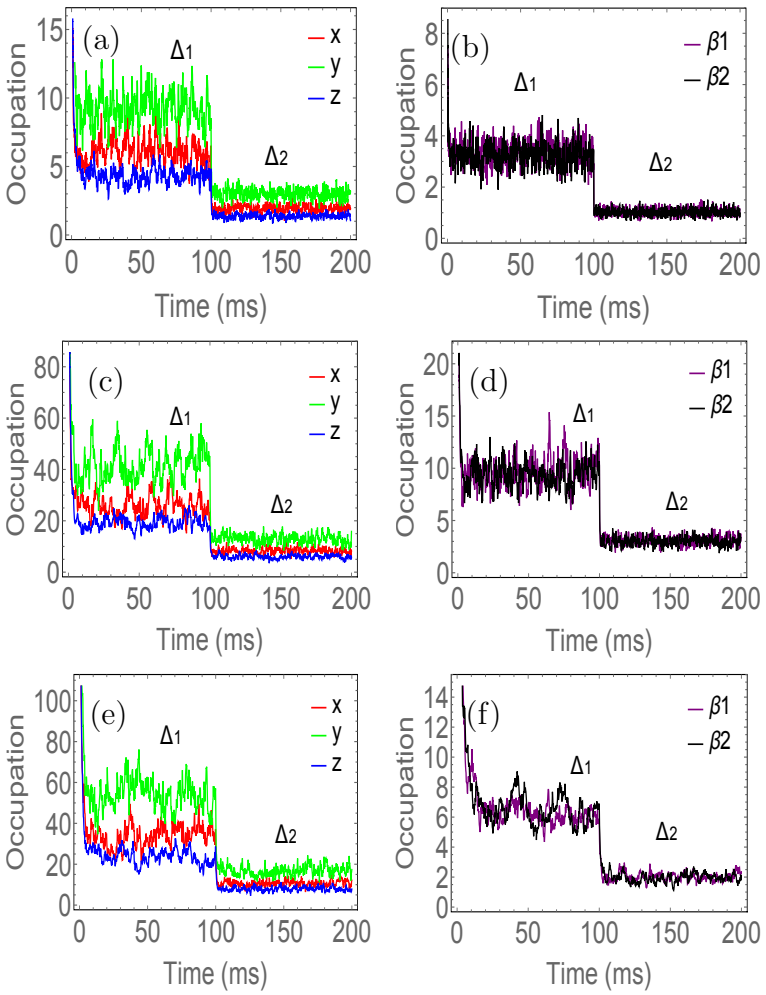

Figure 5.5. The parametric feedback cooling for nano-diamonds in all degrees of freedom, where each curve shows the time evolution of the average occupation number in the corresponding degree of freedom. Data are collected by averaging 30 cooling trajectories. Calculations are for classical parametric feedback cooling, thus results for occupation numbers less than 10 are suggestive. **(a)** and **(b)** depict the translational and rotational cooling respectively for a nanoparticle with half axes ($a = 15$ nm, $b = 70$ nm). The cooling parameter $\Delta_1 = \{\chi_i = 1.1 \times 10^{11}$ s/m$^2, \zeta_i = 10^{11}$ s/m$^2\}$ for $t < 100$ms and $\Delta_2 = 10\Delta_1$ for $t > 100$ms. Similarly, **(c)** and **(d)** show the cooling for half axes ($a = 38$ nm, $b = 60$ nm) while **(e)** and **(f)** for half axes ($a = 48$ nm, $b = 53$ nm).

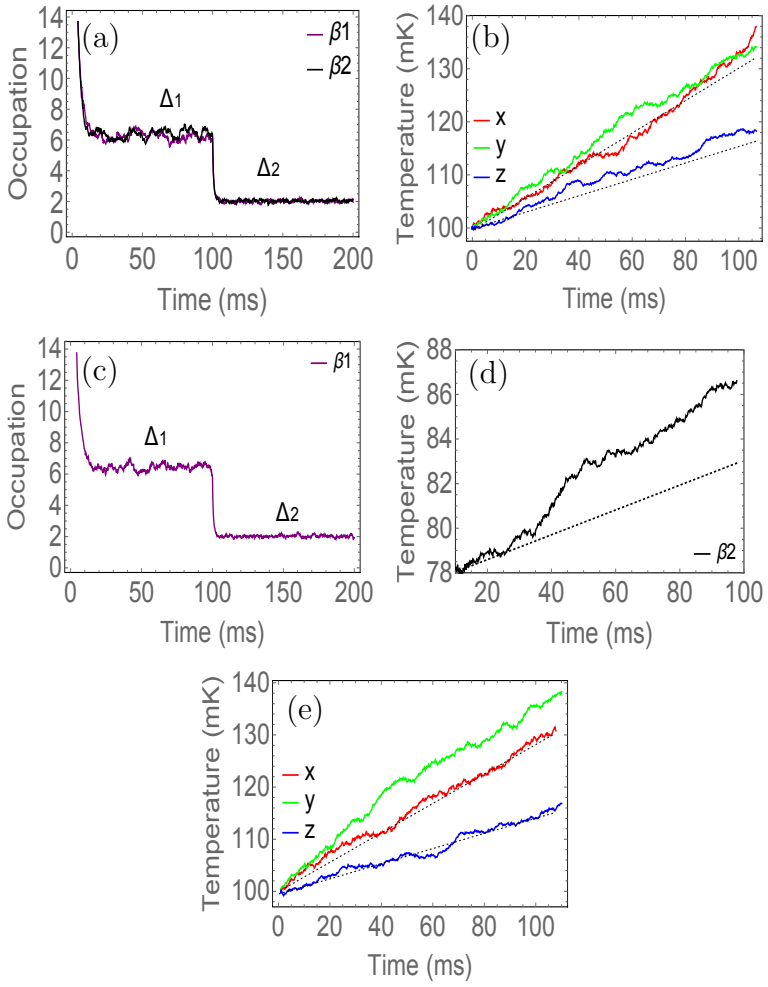

Figure 5.6. The parametric feedback cooling in only the rotational degrees of freedom for a nano-diamond ($a = 48$ nm, $b = 53$ nm). All curves are averaged over 400 trajectories. **(a)** and **(b)** show the cooling in both β_1 and β_2 with the cooling parameters $\Delta_1 = \{\chi_{1,2,3} = 0, \zeta_i = 10^{11}\ \mathrm{s/m^2}\}$. The black and purple lines show the rotational motion gets cooled as we increase the feedback parameters from Δ_1 to $\Delta_2 = 10\Delta_1$. The red, green and blue lines depict that the heating trajectories in translational degrees of freedom. **(c)**, **(d)** and **(e)** show the result of cooling in only β_1 with parameters $\Delta_1 = \{\chi_{1,2,3} = 0, \zeta_2 = 0, \zeta_1 = 10^{11}\ \mathrm{s/m^2}\}$ and $\Delta_2 = 10\Delta_1$, and heating in β_2 and x, y, z respectively. In **(d)**, resonance heating causes massive heating in the uncooled β_2 degree of freedom. The dashed lines in **(b)**, **(d)** and **(e)** are the heating curves $T = T_0 + \dot{E}t$ with T_0 the initial temperature and $\dot{E}$ the corresponding heating rate from Tab. 5.1.

The small oscillation approximation is used in the above equations where all corrections quadratic in the amplitude of oscillations have been dropped. $x_i = (x, y, z)$ and $\beta_j = (\beta_1, \beta_2)$. The shot noises in translation and rotation are added at each time step according to

$$\begin{aligned} p_i(t + \delta t) &= p_i(t) + \delta W_i \cdot \delta p_i, \\ L_i(t + \delta t) &= L_i(t) + \delta R_j \cdot \delta L_j, \end{aligned} \tag{5.32}$$

where $\delta W_i, \delta R_j$ are the standard normally distributed random numbers, and $\delta p_i = \sqrt{2\dot{E}_{T_i}\delta t \cdot m}, \delta L_j = \sqrt{2\dot{E}_{R_j}\delta t \cdot I}$ are the fluctuation of the momentum and angular momentum for each degree of freedom induced by the shot noise. The heating rate in the z direction (optical polarization direction) is half that of the other two translational degrees of freedom because the photons scatter less in the direction of the laser polarization [11]. Δ is a scalar which takes the form

$$\Delta = \sum_{i=1,2,3} \chi_i x_i \dot{x}_i + \sum_{i=1,2} \zeta_i r^2 \beta_i \dot{\beta}_i, \tag{5.33}$$

where r is the size of the nanoparticle. The feedback parameters χ_i and ζ_i have the unit $Time/Length^2$ and they control the cooling limit and speed. Details about the parameters and the parametric feedback cooling limit are given in Appx. A. Simulations are performed for three different nano-diamonds with decreasing ellipticity, whose half axes go from ($a = 15$ nm, $b = 70$ nm), ($a = 38$ nm, 60 nm) to ($a = 48$ nm, $b = 53$ nm). The corresponding parameters are given in Tab. 5.1. The classical equations of motion are numerically solved using a fourth-order Runga-Kutta algorithm with adaptive time steps [66]. All simulations are repeated many times and data is collected by averaging over the different runs to reduce the random noise.

We start by presenting the simulation with zero feedback ($\chi_{1,2,3} = 0$, $\zeta_{1,2} = 0$), which corresponds to the pure shot noise heating process. The system is prepared initially at temperature $T_i = 1$ μK. The result is shown in Fig. (5.4), where each curve depicts the time evolution of the energy in the corresponding degrees of freedom. Figure 5.4(a) and 5.4(b) show the case ($a = 15$ nm, $b = 70$ nm) in the first 100 ms. The rotational shot noise is about an order of magnitude larger than that in the

translational motion. The case (a = 38 nm, b = 60 nm) is given in Fig. 5.4(c) and 5.4(d), in which the rotational and translational shot noise heating rates are of similar size. As the ellipticity gets smaller, the shot noise in the rotational degrees of freedom becomes less than that in the translational motion, which is shown in the Fig. 5.4(e) and 5.4(f) for the case (a = 48 nm, b = 53 nm). From Tab. 5.1, the case (a = 48 nm, b = 53 nm) has a higher rotational than translational oscillating frequency, which suggests that it might be a good candidate for rotational cooling.

The non-zero feedback cooling is performed with the system temperature initially prepared at T_i = 0.1 K. The feedback parameters (χ_i, ζ_i) are chosen in a way such that Eq. (5.33) is much smaller than one and the position and velocity are assumed to be measured perfectly.

First, we turn on the feedback in all degrees of freedom. The results are shown in Fig. (5.5). Because the calculations are classical, the results for occupation less than 10 are qualitative/suggestive. However, we do expect that the classical results are approximately correct for $\langle n \rangle \sim 10$ so we do expect this feedback could get to near the ground state. By tuning the feedback parameters from $\Delta_1 = \{\chi_{1,2,3} = 1.1 \times 10^{11}$ s/m$^2, \zeta_{1,2} = 10^{11}$ s/m$^2\}$ to $\Delta_2 = 10\Delta_1$, the system is observed to be quickly cooled. Both the translational and rotational occupation numbers can get down to less than one in this classical calculation, which suggests a possibility of ground state cooling in all degrees of freedom. Figure 5.5(a) and 5.5(b) depict the cooling of a nanodiamond with half axes (a = 15 nm, b = 70 nm) in the translational and rotational degrees of freedom respectively. We see that rotation and translation are cooled with almost equal speed though the rotational oscillating frequency is more than six times higher than that for the translational motion. As the ellipticity goes lower, the cooling in rotation becomes more effective than in translation. As shown in Fig. 5.5(c) and 5.5(d) for case (a = 38 nm, b = 60 nm), when the parameter Δ_1 is taken, the rotational occupation numbers go down close to 10 while the translational occupation numbers are still around 20. The cooling in rotation gets even better when the particle with half axes (a = 48 nm, b = 53 nm) is used, where the rotation

is close to the ground state ($\langle n \rangle < 1$) while the translational occupation numbers are still more than 10, as shown in Fig. 5.5(e) and 5.5(f). The reason is that when the ellipticity of the nanoparticle gets smaller, the rotational shot noise heating is less than that for translational heating while the rotational oscillating frequency is still larger than that for translation. Thus, a better rotational cooling for a particle with low ellipticity is expected, which was suggested in the previous section. From Appx. A, the steady state value of $\langle n \rangle$ is proportional to the square root of $\dot{E}/\omega^2$. This suggests that smaller values of $\Delta n = 2\pi\dot{E}/(\hbar\omega^2)$, as defined in the previous section, are better for cooling to the ground state. However, we will see in the next section that measurement noise qualitatively modifies this trend.

Second, we keep the feedback cooling only in the rotational degrees of freedom with $\Delta_1 = \{\chi_{1,2,3} = 0, \zeta_{1,2} = 10^{11}\ \mathrm{s/m^2}\}$ and $\Delta_2 = 10\Delta_1$. The results are shown in Fig. 5.6(a) and 5.6(b) for the nano-diamond with half axes ($a = 48$ nm, $b = 53$ nm). As shown in Fig. 5.6(a), when the feedback is increased from Δ_1 to $\Delta_2 = 10\Delta_1$, the rotational occupation number goes down all the way to the quantum regime. However, as shown in Fig. 5.6(b), the translational motion is heated up in the mean time. In order to see the cooling in only one rotational degree of freedom, we also calculate the case with $\Delta_1 = \{\chi_{1,2,3} = 0, \zeta_2 = 0, \zeta_1 = 10^{11}\ \mathrm{s/m^2}\}$. As shown in Fig. 5.6(c), 5.6(d) and 5.6(e), the motion in β_1 degree of freedom quickly gets cooled to the ground state regime when Δ_2 are taken, while all other degrees of freedom (β_2, x, y and z) are heated up. For β_2, extra heating is observed due to the resonance heating: the changes in the laser intensity are predominantly at the frequency to resonantly couple with either of the rotational degrees of freedom. In Fig. 5.6(b), 5.6(d) and 5.6(e), the dashed lines show the heating from pure shot noise. We see that the pure shot noise heating rates are slightly lower (almost the same) than the heating rate with feedback cooling. The reason is because the cooling in one degree of freedom can add to the heating in the other degrees of freedom. Fortunately, this extra heating is not excessive and should not be a problem in experiments.

5.5 The parametric feedback cooling limit with classical uncertainty

The above discussion of feedback cooling is based on an ideal measurement of the particle's position and velocity. In reality, a measurement can't be infinitely accurate and is fundamentally limited by the quantum uncertainty $\delta x \delta p \geqslant \hbar/2$, which introduces an extra feedback noise during the cooling process. The uncertainty in the position measurement can be reduced by increasing the photon scattering rate, however stronger photon scattering induces faster shot noise heating. Thus, tuning an appropriate photon recoil rate and a proper feedback parameter should be important in optimizing the feedback cooling.

This section numerically studies the optimal cooling limit when the main error in the position measurement is due to classical measurement uncertainty. As we will show below, the equations of motion can be scaled. Therefore, the simulation is performed in only the x degree of freedom for the case ($a = 48$ nm, $b = 53$ nm) in Tab. 5.1. The calculation is still classical, but the feedback signal is modified to satisfy $\delta x \delta p = N\hbar/2$, where N is a measure of the classical uncertainty. The dynamical equation is given by

$$\begin{aligned} m\frac{d^2x}{dt^2} &= -m\omega_x^2(1 + \chi x_m \dot{x}_m)x, \\ x_m &= x + \delta R \cdot \delta x, \end{aligned} \tag{5.34}$$

and the shot noise is added according to

$$p(t + \delta t) = p(t) + \delta W \cdot \delta p, \tag{5.35}$$

where δR and δW are Gaussian random numbers with unit variance, $\delta p = \sqrt{2\dot{E}_{T_x}\delta t \cdot m}$ is the momentum fluctuation determined by the shot noise $\dot{E}_{T_x}$, and x_m is the measured position with $\delta x = N\hbar/(2\sqrt{2\dot{E}_{T_x}\delta t \cdot m})$, which is chosen to satisfy the relation $\delta x \delta p = N\hbar/2$. Several values of N are used in the the pure classical calculation. In reality, the results are not physically possible for $N < 1$, and for small N the result is only suggestive because it would require a true quantum treatment. Figure (5.7) shows the results, where each curve corresponds to the steady state occupation in

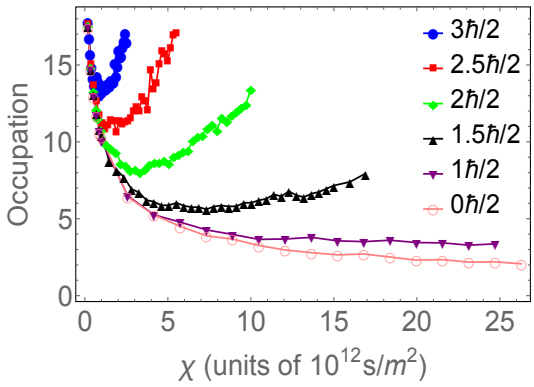

Figure 5.7. The steady state occupation in terms of the feedback paramter χ for x degree of freedom of the particle ($a = 48$ nm, $b = 53$ nm) from Tab. 5.1. The different curves correspond to several different values of classical uncertainty.

terms of the feedback parameter χ. The pink line corresponds to the classical feedback with no noise in the position measurement ($N = 0$), where the occupation keeps decreasing as we increase the feedback parameter. As we add uncertainty to the feedback signal, the purple ($N = 1$), black ($N = 1.5$), green ($N = 2$), red ($N = 2.5$) and blue ($N = 3$) lines will go up after passing their minimal occupations, which are the corresponding optimal cooling limit. The reason is that, as χ increases, the feedback cooling is strengthened, but the noise in the measured value of x leads to the feedback procedure itself adding noise to the motion. Beyond a value of χ, the feedback noise heating becomes faster than the feedback cooling, which indicates that the steady state occupation can reach a minimum and then increase. Moreover, one can see that a larger uncertainty in the position measurement leads to a larger occupation for optimal cooling limit. The reason is that the feedback noise heating is generally faster with a big N in the position measurement than that with a smaller N.

The steady state occupation is also related to the shot noise heating and the oscillating frequency, as suggested by the result in Appx. A, $\langle n \rangle_{limit} \propto \sqrt{\dot{E}_T/\omega^2}$

for ideal measurements. In fact, the one dimensional dynamical equation for the nanoparticle can be scaled

$$\begin{aligned} \frac{d^2\tilde{x}}{d\tilde{t}^2} &= -\tilde{x}(1+\chi\frac{\hbar}{2m}\tilde{x}_m\dot{\tilde{x}}_m), \\ \tilde{x}_m &= \tilde{x}+\delta R\cdot\delta\tilde{x}, \end{aligned} \tag{5.36}$$

and the shot noise is added according to

$$\tilde{p}(t+\delta t) = \tilde{p}(t)+\delta\tilde{p}(t)\delta W, \tag{5.37}$$

where the scaled position $\tilde{x} = x/a_0$ with $a_0 = \sqrt{\hbar/(2m\omega_x)}$, $\tilde{t} = \omega_x t$, and $\dot{\tilde{E}}_T = 2\dot{E}_T/(\hbar\omega_x^2)$. $\delta\tilde{p} = \sqrt{2\dot{\tilde{E}}_T/d\tilde{t}}$ and $\delta\tilde{x} = N\sqrt{1/(2\dot{\tilde{E}}_T d\tilde{t})}$. The scaled equation shows that $\Delta n = 2\pi\dot{E}_T/(\hbar\omega_x^2)$ (as defined previously), N and χ determine the particle's dynamics. To confirm that, we simulate the cooling of the x degree of freedom for particle ($a = 48$ nm, $b = 53$ nm) with fixed measurement uncertainty ($N = 2$). First, we choose ($\dot{E}_T$, ω_x) to be different values (470 mK/s,343 kHz), (824 mK/s,454 kHz) and (1295 mK/s,569 kHz), which are obtained by tuning the laser power to $P = (40\text{ mW}, 70\text{ mW}, 110\text{ mW})$ respectively. Figure 5.8(a) gives the simulation results, where the three curves give the steady state occupation in terms of the feedback parameter. Those curves match each other, which confirms that Δn indeed determines the dynamics, since varying the laser power doesn't change the quantity $\Delta n \simeq 0.083$. All three curves get to an optimal cooling limit around $\langle n\rangle = 8.5$ when $\chi = 3.3\times10^{12}$ s/m^2. In Fig. 5.8(b), we take $\Delta n \simeq 0.026$ by changing the laser beam waist. Using the same laser powers $P = (40\text{ mW}, 70\text{ mW}, 110\text{ mW})$, the shot noise heating and the x translational oscillating frequency are (1488 mK/s,1085 kHz), (2603 mK/s,1434 kHz) and (4092 mK/s,1798 kHz) respectively. The three curves still match, but the minimal point is shifted to ($\langle n\rangle = 12, \chi = 5\times10^{11}$ s/m^2), which suggests that the optimal cooling limit should depend on the choice of Δn for a given value of N, the scale factor between the uncertainty in the position measurement, δx, and the momentum shot noise scale, δp.

Comparing the two results in Fig. (5.8), we see that a lower optimal cooling limit is reached for the motion with a bigger Δn when N is held fixed. This motivates us

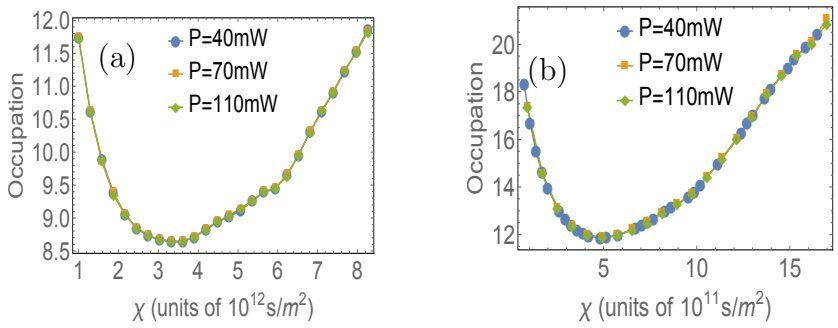

Figure 5.8. The steady state occupation for x degree of freedom of particle (a = 48 nm, b = 53 nm) from Tab. 5.1 in terms of the feedback parameter χ with N = 2. Three different laser powers P = (40 mW, 70 mW, 110 mW) are used. **(a)** The quantity Δn = 0.083; **(b)** The quantity Δn = 0.026.

to calculate the optimal cooling limit for varied Δn (by changing the beam waist), and the result is show in Fig. (5.9), where the two curves correspond to N = (1, 2). Both curves reveal that a bigger Δn leads to a lower optimal cooling limit, which suggests that a more accurate feedback cooling can beat the cost from the higher shot noise heating for fixed N. The fact that a higher shot noise leads to a lower optimal occupation might be because of (1) a higher shot noise indicates a more accurate and effective feedback cooling; (2) an accurate feedback induces a lower feedback noise. Figure (5.9) also shows that a smaller N generally has a lower optimal cooling limit, which matches the result in Fig. (5.7). The data in Fig. (5.9) stops at Δn = 0.41, since a bigger χ is needed in order to get to the optimal cooling limit. Our calculation becomes unstable when χ is too larger. In reality, a bigger feedback parameter χ means a lot more effort in feedback cooling. The maximal realizable χ in the experiment should physically bound the lowest cooling limit for fixed N. The actual shot noise heating rate and measurement uncertainty determines the minimum occupation number. By scaling these parameters, one can understand how the system will respond in terms of the dimensionless Eqs. (5.36) and (5.37).

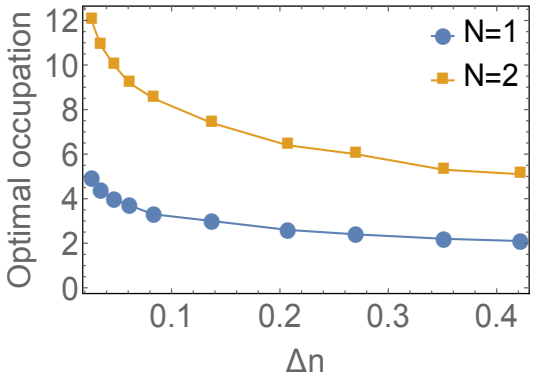

Figure 5.9. The optimal cooling limit for x degree of freedom of particle (a = 48 nm, b = 53 nm) from Tab. 5.1 with respect to Δn. The blue and yellow curves correspond to the classical uncertainty measure N = 1 and N = 2 respectively. Our data stops at Δn = 0.41 since the feedback calculation with a larger χ becomes unstable when we try to reach the optimal cooling limit.

5.6 Summary and conclusion

The translational and rotational shot noise heating and feedback cooling of an optically trapped nano-ellipsoid were analytically and numerically investigated. The detailed analysis suggests that a lower relative rotational heating rate is expected for a wide range of nanoparticle geometries. This conclusion is in contrast to that when scattering from black body radiation was studied [3] which reported that rotational degrees of freedom decohered much faster than translational degrees of freedom. The qualitatively different conclusion is due to the difference in photon scattering from a polarized beam aligned along the nanoparticle axis compared to unpolarized photons.

The analysis and numerical calculation of the shot noise heating suggest that a lower relative rotational heating rate results from (1), a nanoparticle with near to spherical shape for fixed size; (2), a nanoparticle with a bigger size for fixed ellipticity; (3), a trapping laser with a shorter wavelength and a bigger beam waist; (4), a nanoparticle with lower dielectric constant. In addition, the calculation of the feedback cooling in only the rotational degrees of freedom reveals that a separate rotational cooling should be experimentally possible, since heating in the other degrees of freedom was only slightly faster than the shot noise.

The feedback cooling with classical measurement uncertainty was analyzed. The measurement uncertainty introduces an extra noise during the feedback, which competes with the cooling when the feedback parameter increases. When the scaled classical uncertainty N is held fixed, a system with a bigger value of $\Delta n = 2\pi\dot{E}/(\hbar\omega^2)$ could in principle get to a lower optimal cooling limit. While this is an interesting result, it is hard to imagine an experiment where the N can be held fixed while the shot noise heating rate is changed as it would require the uncertainty in x to decrease proportional to $1/\sqrt{\dot{E}}$ as the heating rate increases. A more effective way to achieve small occupation number is to decrease N which is proportional to the uncertainty in x times $\sqrt{\dot{E}}$.

In conclusion, the shot noise heating, the measurement uncertainty, and the feedback parameter are important factors to consider when cooling a levitated nanoparticle in the shot noise dominant region. The results presented here can provide a framework for thinking about how these parameters affect the heating and the feedback cooling of levitated nanoparticles. However, since our calculations are classical, there is still a need for investigations of quantum effects on feedback cooling for small occupation number. The results in Fig. (5.9) suggest there may be non-intuitive trends in the quantum limit. We will investigate the quantum cooling in the next chapter.

6. QUANTUM CALCULATION OF FORCE FEEDBACK AND PARAMETRIC FEEDBACK COOLING OF A LASER LEVITATED NANOPARTICLE

In this chapter, we explore the quantum feedback cooling of an optically trapped nanoparticle in the laser-shot-noise-dominant regime. We numerically investigate the levitated system using both parametric and force feedback cooling schemes. We show that, for the same position measurement efficiency, the cooling limit from the force feedback is lower than that from the parametric feedback. We also develop a set of semi-classical equations for feedback cooling that accurately match the quantum results. By rescaling the semi-classical equations, the cooling dynamics is shown to be determined simply by the following parameter set: the feedback strength, the position measurement efficiency and the change of occupation number over one oscillation period due to the shot noise. The minimum occupation number that can be reached is determined by the measurement efficiency and the change of occupation number over one period.

6.1 Introduction

The system of optically trapped nanoparticles has recently emerged as an exciting candidate for tests of quantum mechanics at the mesoscale [43, 49, 56, 57, 60]. It helps not only in our understanding of quantum fundamentals, such as the role decoherence plays in the quantum-classical transition, but also in the study of many other physical topics, such as ultrasensitive metrologies [43, 44, 47, 54, 67–69], spin optomechanics [70, 71], and nonlinear physics [50]. Because the nanoparticle is levitating, good thermal isolation can be reached. Recent experiments with optical cavities have demonstrated

cooling of a levitated particle to several kelvin [72, 73], and ground state cooling was also suggested [74]. For a trapped nanoparticle without a cavity, much lower temperatures have been reached by feedback cooling [49, 75]. While most discussions are given in the classical regime, the first quantum model for parametric feedback cooling and force sensing using a single-laser-trapped nanoparticle was studied in Ref. [57], and it demonstrated quite different features from the standard cavity-assisted cooling [74, 76, 77], such as the non-exponential decay of phonon number and the nonlinear dissipative mechanism [57].

In a recent experiment [11], it was reported that the photon shot noise overwhelms the thermal noise by at least a factor of 25 when the particle is trapped in ultrahigh vacuum (the pressure is about 10^{-8} mbar). Thus, the shot noise from the trapping laser becomes the particle's major source of decoherence. In this chapter, we present results on the quantum feedback cooling of a single-laser-trapped nanoparticle in the shot-noise-dominant regime. The feedback signal is obtained through continuously measuring the particle's position [78]. Due to the measurement back-action, the system state evolves stochastically, which is described by a stochastic master equation or equivalently by a stochastic Schrödinger equation [12, 79]. The measured position is used to modify the system Hamiltonian such that cooling of the center of mass degrees of freedom is achieved [59].

The force feedback and the parametric feedback schemes are widely used in cooling optically trapped mesoscale particles [49, 80–82]. They are realized by controlling the force exerted on the particle (force feedback) [80] or by changing the trapping laser intensity (parametric feedback) [49]. In this chapter, the cooling of an optically trapped nanoparticle is simulated using these two feedback cooling schemes. For each cooling scheme, we calculate and compare the steady state occupation number as a function of the feedback strength and the measurement efficiency. It is demonstrated that a lower cooling limit can be reached by force feedback cooling than by parametric feedback cooling for the same measurement efficiency. We also develop a set of semi-classical equations for modeling the feedback cooling, and introduce

a concept of classical measurement uncertainty [4]. It is shown that the quantum and semi-classical results of the cooling limit are identical. Remarkably, by rescaling the semi-classical equations, we find that the optimal cooling limit is uniquely determined by the parameter set: Δn (defined as the change of occupation number in a vibrational period due to the shot noise), the feedback cooling strength, and the measurement efficiency. Our study provides a useful guide and framework for the community to think about how those parameters affect the the feedback cooling of levitated nanoparticles.

The measurement efficiency plays a significant role in both the force feedback and the parametric feedback cooling. In order to achieve ground state cooling ($\langle n \rangle < 1$), a suitable measurement efficiency must be reached. For the force feedback scheme, more than ten percent measurement efficiency is sufficient for cooling the nanoparticle to the ground state, while a higher efficiency (more than forty percent) is needed for the parametric feedback to achieve ground state cooling. In practice, the measurement efficiency is determined by the photon collection efficiency and the actual measurement scheme. For a widely used balanced Homodyne detection scheme, the position measurement efficiency is shown to be bound from above by an intrinsic detection efficiency. This bound places a challenge for reaching the ground state cooling. However, this derivation we present is only accurate for trapping lasers with small numerical aperture (NA). It might be possible to get a higher position measurement efficiency than that for balanced Homodyne detection using other methods, such as using a tightly focused laser beam, using a different photon collection scheme [83], or using quantum metrology that could possibly break the Cramér-Rao bound [84, 85].

6.2 The laser levitated nanoparticle

A laser levitated nanoparticle in ultrahigh vacuum is well isolated from its thermal environment. Due to the isolation, the trapping laser is the particle's major source of heating [11], which results from the recoil caused by each of the randomly scattered

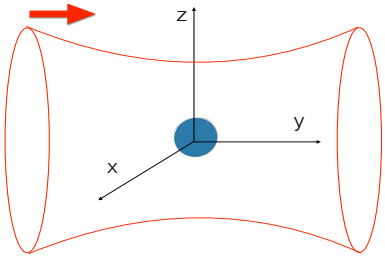

Figure 6.1. A nanoparticle with mass m is trapped at the focus of a laser beam (schematically shown by the red line), which is polarized in the z direction and propagating in the positive y direction (shown by the red arrow).

photons. We consider a nanoparticle trapped in the focus of a linearly polarized laser beam, as shown in Fig. (6.1). The laser field is polarized in z and propagating in the positive y direction. Using a scattering model [3, 10, 37, 38], one can show that the system density operator $\boldsymbol{\rho}$ follows the master equation

$$\frac{d\boldsymbol{\rho}}{dt} = \frac{1}{i\hbar}[\boldsymbol{H}, \boldsymbol{\rho}] - \kappa[\boldsymbol{x}, [\boldsymbol{x}, \boldsymbol{\rho}]], \tag{6.1}$$

where the wavelength of the light is assumed to be much larger than the size of the nanoparticle. $\boldsymbol{H}$ is the system Hamiltonian which will be given below. The last term is from the decoherence due to photon scattering which localizes the position of the nanoparticle. $\boldsymbol{x}$ is the position operator and $\kappa = \dot{E}m/\hbar^2$ is the interaction strength, where $\dot{E}$ is the shot noise heating from the trapping laser and m is the particle mass. $\dot{E}$ takes the form [11, 49]

$$\dot{E} = \frac{8\pi J_p}{3}\left(\frac{k_0^2}{4\pi\epsilon_0}\right)^2 \alpha^2 \frac{\hbar^2 k_0^2}{2m}, \tag{6.2}$$

where J_p is the laser photon flux, k_0 is the incoming wave vector, $\alpha = 4\pi\epsilon_0 R^3(\epsilon - 1)/(\epsilon + 2)$ is the particle polarizability, ϵ_0 is the vacuum dielectric constant and ϵ is the relative dielectric constant. It is worth mentioning that, because of the detailed pattern of dipole radiation, the shot noise is different in each degree of freedom by the factors $\zeta_x = \zeta_y = 2/5$, $\zeta_z = 1/5$. The factors must be added to the corresponding degree of freedom when evaluating the shot noise [49].

The nanoparticle is trapped at the focus by an optical gradient force. If one models the laser beam as Gaussian and takes a small oscillation approximation [65, 86], each degree of freedom of the particle oscillates as an independent harmonic oscillator along its principal axis. The Hamiltonian can be written as

$$\boldsymbol{H} = \sum_{i=x,y,z} \hbar\omega_i(\boldsymbol{a}_i^\dagger \boldsymbol{a}_i + \frac{1}{2}), \tag{6.3}$$

Table 6.1.
The parameters for diamond and fused silica with sizes $R \simeq 50$ nm trapped in a laser beam. The laser has wavelength $\lambda = 1064$ nm, power $P = 70$ mW and an objective lens with numerical aperture NA= 0.9. The parameters are given in the x degree of freedom.

	ϵ	mass (kg)	ω_x (kHz)	$\dot{E}$ (W)	Δn
diamond	5.7	1.79×10^{-18}	$2\pi \times 454$	4.55×10^{-24}	0.033
silica	2.1	1.13×10^{-18}	$2\pi \times 374$	1.32×10^{-24}	0.014

where $\boldsymbol{a}_i^\dagger, \boldsymbol{a}_i$ are creation and annihilation operators respectively. The oscillation frequencies ω_i were shown to be [65, 86]

$$\begin{aligned} \omega_{x,z} &\simeq \sqrt{\frac{\alpha}{m}}\frac{E_0}{w_0}, \\ \omega_y &\simeq \sqrt{\frac{\alpha}{2m}}\frac{E_0}{y_0}, \end{aligned} \tag{6.4}$$

where $y_0 = \pi w_0^2/\lambda$, $w_0 = \lambda/(\pi \mathrm{NA})$ is the beam waist, and E_0 is the field strength at the center of the laser focus. In this following discussions, we use a laser with wavelength $\lambda = 1064$ nm, power $P_0 = 70$ mW, and an objective lens with numerical aperture NA$= 0.9$. The particle size is $R = 50$ nm. For later discussions, we evaluate the parameters related to feedback cooling Tab. (6.1). Since each degree of freedom of the nanoparticle is essentially decoupled, we focus on only the x degree of freedom in the following discussions. The notations without subindex all correspond to quantities in the x degree of freedom.

6.3 Continuous quantum measurement and the feedback cooling scheme

In quantum feedback control, a system needs to be continuously measured and the measured information collected to modify the system Hamiltonian so as to achieve a targeted outcome [59]. The system evolution conditioned on the measurement result can be derived by the theory of continuous quantum measurement [12, 79]. For demonstration, I am going to briefly summarize the theory in this thesis.

6.3.1 Continuous quantum measurement

Quantum states can be identified with linear operators $\boldsymbol{\rho}$ defined on a Hilbert space, where $\boldsymbol{\rho}$ is positive and trace one [1] ($\boldsymbol{\rho} \geq 0, \mathrm{tr}(\boldsymbol{\rho}) = 1$) [87]. Imagine we directly measure an observable which has a spectral decomposition,

$$\boldsymbol{O} = \sum \lambda_n \boldsymbol{P}_n, \tag{6.5}$$

[1] $\boldsymbol{\rho} \geq 0$ means all its eigenvalues are non-negative. Pure or mixed quantum states can be identified with $\boldsymbol{\rho}$'s, where pure states correspond to $\boldsymbol{\rho}$'s with only one non-zero eigenvalue whereas mixed states have more than one.

where the $\boldsymbol{P}_n$ are the projection operators. The measurement will project the system onto an eigenstate of the observable

$$\boldsymbol{\rho}_f = \frac{\boldsymbol{P}_n \boldsymbol{\rho} \boldsymbol{P}_n}{\mathrm{tr}(\boldsymbol{P}_n \boldsymbol{\rho} \boldsymbol{P}_n)}, \tag{6.6}$$

with a probability given by $P(n) = \mathrm{tr}(\boldsymbol{P}_n \boldsymbol{\rho} \boldsymbol{P}_n)$. This projection measurement is also called the von Neumann measurement, which is sometimes referred to as the process of wave function collapse.

Besides projection measurement, there is a more generalized measurement which is called positive operator valued measurement (POVM). The generalized POVM typically can be implemented by first coupling the system to an auxiliary system, then performing a projection measurement on the auxiliary system. This enables us to do a so-called weak measurement, by which the system information is partially revealed. Continuous quantum measurement corresponds to the process where partial information is continuously extracted by applying POVM repeatedly.

Unlike the projection measurement, the POVM is described as a set of arbitrary operators $\{\boldsymbol{E}_m\}$ satisfying the completeness relation $\sum_m \boldsymbol{E}_m^\dagger \boldsymbol{E}_m = \boldsymbol{I}$. The operators $\boldsymbol{E}_m$ don't need to be orthogonal to each other. A POVM measurement on the system will yield an outcome m with probability $P(m) = \mathrm{tr}(\boldsymbol{E}_m \boldsymbol{\rho} \boldsymbol{E}_m^\dagger)$, and the system state becomes

$$\boldsymbol{\rho}_f = \frac{\boldsymbol{E}_m \boldsymbol{\rho} \boldsymbol{E}_m^\dagger}{\mathrm{tr}(\boldsymbol{E}_m \boldsymbol{\rho} \boldsymbol{E}_m^\dagger)}. \tag{6.7}$$

In the following, we discuss the continuous position measurement. The observable $\boldsymbol{X}$ has a continuous spectrum

$$\boldsymbol{X} |x\rangle = x |x\rangle, \tag{6.8}$$

where $\langle x|x'\rangle = \delta(x - x')$. Suppose one designs a POVM

$$\boldsymbol{E}_\alpha = C \int_{-\infty}^{\infty} \exp[-2\kappa \Delta t (x - \alpha)^2] \, |x\rangle \langle x| \, dx, \tag{6.9}$$

where $C = (4\kappa \Delta t/\pi)^{1/4}$, κ is the measurement strength (discussed below) and α is a continuous index, which serves to label the measured results. Δt is the time interval for the measurement; we will take the small time limit $\Delta t \to 0$ to recover

the continuous measurement. One can easily check that the completeness formula $\oint_\alpha \boldsymbol{E}_\alpha^\dagger \boldsymbol{E}_\alpha = \boldsymbol{I}$ is satisfied.

Suppose that we have an initial state $\boldsymbol{\rho} = |\psi\rangle\langle\psi|$. The probability for getting a result α is

$$\begin{aligned} P(\alpha) =& \mathrm{tr}(\boldsymbol{E}_\alpha^\dagger \boldsymbol{E}_\alpha \boldsymbol{\rho}), \\ =& (\frac{4\kappa\Delta t}{\pi})^{1/2} \int_{-\infty}^{\infty} \left|\psi(x)\right|^2 \exp[-4\kappa\Delta t(x-\alpha)^2] dx, \\ =& (\frac{4\kappa\Delta t}{\pi})^{1/2} \int_{-\infty}^{\infty} \delta(x - \langle \boldsymbol{X}\rangle) \exp[-4\kappa\Delta t(x-\alpha)^2] dx, \\ =& (\frac{4\kappa\Delta t}{\pi})^{1/2} \exp[-4\kappa\Delta t(\alpha - \langle \boldsymbol{X}\rangle)^2], \end{aligned} \tag{6.10}$$

where we use $\psi(x) \sim \delta(x - \langle \boldsymbol{X}\rangle)$, because for sufficiently small Δt, the expression $\exp[-4\kappa\Delta t(x-\alpha)^2]$ will be much broader than $\psi(x)$, such that $\psi(x)$ can be approximated as a δ-function centered at $\langle \boldsymbol{X}\rangle$. From the above result, we see that the probability of getting a result α satisfies a Gaussian distribution, and the maximal probability is obtained when $\alpha = \langle \boldsymbol{X}\rangle$. It is equivalent to say that the measured result is a stochastic quantity

$$\alpha = \langle \boldsymbol{X}\rangle + \frac{dW}{\sqrt{8\kappa\Delta t}}, \tag{6.11}$$

where dW is a Gaussian random number with standard deviation equal to one. Also, we see that the measurement strength κ is related to the uncertainty of the measured position. It is quite reasonable that a weak measurement gives us a large amount of noise while a small uncertainty is guaranteed if a system is strongly measured.

The time evolution of the system state can be derived by calculating the change in the time interval Δt and then taking the small time limit. The system state after a measurement $\boldsymbol{E}_\alpha$ is given by

$$\begin{aligned} |\psi(t+\Delta t)\rangle &\propto \boldsymbol{E}_\alpha |\psi(t)\rangle, \\ &\propto \exp[-2\kappa\Delta t(\boldsymbol{X} - \alpha)^2] |\psi(t)\rangle. \end{aligned} \tag{6.12}$$

Now, if one Taylor expands the above expression and keep the terms to the order of $O(\Delta t)$, and normalizes the state, the following formula follows

$$d|\psi(t)\rangle = [-\kappa(\boldsymbol{X} - \langle \boldsymbol{X}\rangle)^2 dt + \sqrt{2\kappa}(\boldsymbol{X} - \langle \boldsymbol{X}\rangle)\sqrt{dt} dW] |\psi(t)\rangle, \tag{6.13}$$

where $d|\psi(t)\rangle = |\psi(t+\Delta t)\rangle - |\psi(t)\rangle$ and the limit $\Delta t \to dt$ is taken. The above equation is defined as the stochastic Schrödinger equation (SSE), which is conditioned on the measured result (To indicate position measurement, we use x_i instead of α as the measured result from now)

$$x_i = \langle \boldsymbol{X} \rangle + \frac{dW}{\sqrt{8\kappa dt}}. \tag{6.14}$$

We see that $|\psi(t)\rangle$ evolves randomly and each realization is called the quantum trajectory.

The above SSE can be recast into a stochastic master equation (SME) if we identify $\boldsymbol{\rho}(t) = |\psi(t)\rangle\langle\psi(t)|$. The result is

$$\begin{aligned} \boldsymbol{d\rho} &= -\kappa[\boldsymbol{X},[\boldsymbol{X},\boldsymbol{\rho}]]dt + \sqrt{2\kappa}(\boldsymbol{X\rho} + \boldsymbol{\rho X} - 2\langle \boldsymbol{X} \rangle \boldsymbol{\rho})\sqrt{dt}dW, \\ x_i &= \langle \boldsymbol{X} \rangle + \frac{dW}{\sqrt{8\kappa dt}}, \end{aligned} \tag{6.15}$$

which describes the system evolution under perfect detection efficiency. In reality, we will encounter inefficient measurement, where not all measured information can be collected. We can imagine two observers are making position measurements on the same system with measurement strengths κ_1 and κ_2. Each observer does not have access to the information from the other, so they must average over each other's results. It is equivalent to say that each observer has a less certain measured result. Take the first observer for example: the system state, from his knowledge, evolves

$$\begin{aligned} \boldsymbol{d\rho} &= -\kappa[\boldsymbol{X},[\boldsymbol{X},\boldsymbol{\rho}]]dt + \sqrt{2\eta\kappa}(\boldsymbol{X\rho} + \boldsymbol{\rho X} - 2\langle \boldsymbol{X} \rangle \boldsymbol{\rho})\sqrt{dt}dW, \\ x_i &= \langle \boldsymbol{X} \rangle + \frac{dW}{\sqrt{8\eta\kappa dt}}, \end{aligned} \tag{6.16}$$

where $\kappa = \kappa_1 + \kappa_2$ and $\eta = \frac{\kappa_1}{\kappa}$ is defined as the detection efficiency for the first observer. For the second observer, a similar expression can be derived. The above expression is actually very general, since it is impossible to collect all signals in any real measurement.

6.3.2 The feedback cooling schemes

From the previous subsection, it is demonstrated that, due to the position measurement, the system state evolves stochastically according to

$$\begin{aligned} d\boldsymbol{\rho} =& \frac{1}{i\hbar}[\boldsymbol{H}, \boldsymbol{\rho}]dt - \kappa[\boldsymbol{x}, [\boldsymbol{x}, \boldsymbol{\rho}]]dt \\ &+ \sqrt{2\eta\kappa}(\boldsymbol{x}\boldsymbol{\rho} + \boldsymbol{\rho}\boldsymbol{x} - 2\langle \boldsymbol{x} \rangle \boldsymbol{\rho})\sqrt{dt}dW, \\ x_i =& \langle \boldsymbol{x} \rangle + \frac{dW}{\sqrt{8\eta\kappa dt}}, \end{aligned} \tag{6.17}$$

which is the SME discussed above. x_i is the directly measured value of position. In our feedback cooling calculation, x_i is time averaged to get a better estimate of the particle position x_m (shown in Appx. B). $\langle \boldsymbol{x} \rangle = \mathrm{tr}(\boldsymbol{\rho}\boldsymbol{x})$. The parameter η is the measurement efficiency, which determines the uncertainty in the measured position, $\Delta x = 1/\sqrt{8\eta\kappa dt}$. From Eq. (6.2), a random momentum kick can be obtained $\Delta p = \sqrt{2\kappa dt}\hbar$. Thus, one immediately finds

$$\Delta x \Delta p = \frac{1}{\sqrt{\eta}} \frac{\hbar}{2}, \tag{6.18}$$

where the measurement efficiency η is by definition smaller than one, $\eta \leq 1$, and $\eta = 1$ corresponds to the minimal uncertainty allowed by quantum mechanics. Obviously, the classical uncertainty N defined in the previous chapter is related to the measurement efficiency η by $N = 1/\sqrt{\eta}$. dW is a standard normally distributed Gaussian random variable. Since dW is random, there would be many solutions to the above equation and each realization $\boldsymbol{\rho}(t)$ defines a quantum trajectory. Equation (6.17), excluding the last stochastic term, is the same as Eq. (6.1). Actually, if all the measured information were lost, one would need to average all the possible quantum trajectories, which leads to Eq. (6.1) due to the zero mean of dW. The evolution of the system can also be written in terms of a wave function $|\psi\rangle$,

$$\begin{aligned} d|\psi\rangle =& \{\frac{1}{i\hbar}\boldsymbol{H}dt - \kappa(\boldsymbol{x} - \langle \boldsymbol{x} \rangle)^2 dt \\ &+ \sqrt{2\kappa}(\boldsymbol{x} - \langle \boldsymbol{x} \rangle)\sqrt{dt}dW\}|\psi\rangle, \end{aligned} \tag{6.19}$$

which is referred to as the stochastic Schrödinger equation (SSE). In quantum simulations, the SSE is generally favored since the numerical calculation cost is much less than that required by the SME [88].

The stochastic equation is conditioned on the measured position, which we can use to modify the system Hamiltonian. We investigate two different feedback cooling schemes. The first one is force feedback. Force feedback was first used in cooling an optically trapped microsphere [80]. It works by exerting a force on the particle with the force direction opposite to the particle's instantaneous momentum. Thus, the modified Hamiltonian can be written as

$$\boldsymbol{H} = \hbar\omega(\boldsymbol{a}^\dagger\boldsymbol{a} + \frac{1}{2}) + \gamma p_m \boldsymbol{X}, \tag{6.20}$$

where $p_m = m\dot{x}_m$ is the feedback momentum (the subscript m indicates a measured variable while the parameter m is the mass). p_m is obtained from the measured position x_m according to the formula

$$\dot{x}_m \simeq -\omega x_m(t - T/4), \tag{6.21}$$

where the small oscillation approximation is used and T is the oscillation period. The parameter γ is the force feedback strength, and $\boldsymbol{X} = \sqrt{\hbar/(2m\omega)}(\boldsymbol{a}^\dagger + \boldsymbol{a})$ is the position operator. In the next section, this Hamiltonian is used in the force feedback cooling by numerically calculating both the SSE and the SME. It is worth mentioning that an extra noise might be introduced depending on the way force feedback is implemented, such as force feedback by implementing radiation pressure [80]. This noise is another source of heating, which is not taken into account in the current discussion.

The other cooling method is parametric feedback, where a single laser beam is used for both trapping and cooling [49, 89]. In the parametric feedback scheme, a signal at twice the oscillation frequency is obtained by multiplying the measured particle's position with its first time derivative $x_m(t)\dot{x}_m(t)$. This signal is then used to modify the laser trapping depth, which on average acts as a drag on the particle. The modified Hamiltonian can be written as

$$\boldsymbol{H} = \hbar\omega(\boldsymbol{a}^\dagger\boldsymbol{a} + \frac{1}{2}) + \frac{\chi}{2} m\omega^2 x_m \dot{x}_m \boldsymbol{X}^2, \tag{6.22}$$

where χ is the parametric feedback strength. In the following section, this Hamiltonian is used in the SSE to simulate the quantum parametric feedback cooling.

6.4 The numerical simulation of feedback cooling

6.4.1 Cooling by force feedback

In this subsection, we present the numerical calculations of the force feedback cooling. Both the SME and the SSE are numerically solved. We first define an average occupation number of the nanoparticle as $\langle n\rangle = \langle \boldsymbol{a}^\dagger \boldsymbol{a}\rangle = \mathrm{tr}(\boldsymbol{\rho a}^\dagger \boldsymbol{a})$. In an experiment, it is this number that one wants to decrease to less than one (the ground state). In the simulation, the particle occupation number $\langle n\rangle$ is calculated with respect to different values of the force feedback strength γ. Besides the quantum calculations, the cooling process is also simulated semi-classically, and we will show later that the quantum calculations match the semi-classical results. The semi-classical occupation is defined as $\langle n\rangle = E/\hbar\omega - 0.5$, where the energy is calculated through $E = \frac{p^2}{2m} + \frac{1}{2}m\omega^2 x^2$. The semi-classical equation of motion for force feedback is given by

$$\begin{aligned} m\frac{d^2x}{dt^2} &= -m\omega^2 x - \gamma p_m, \\ x_i &= x + dW\cdot\Delta x, \end{aligned} \tag{6.23}$$

where x_i is the directly measured position, p_m is the feedback momentum which is obtained from the measured position as discussed in the previous section, and $\Delta x = \hbar/\sqrt{8\eta\dot{E}dt\cdot m}$. During one time step, the shot noise induces a random momentum kick on the particle by

$$p(t+dt) = p(t) + dW\cdot\Delta p, \tag{6.24}$$

where $\Delta p = \sqrt{2\dot{E}dt\cdot m}$. It is worth mentioning that classically there is no theoretical limit to measure the position accurately. The uncertainty in the measured position x_i is added to quantitatively satisfy Eq. (6.18). We call it the classical uncertainty in position and momentum, which also satisfies $\Delta x\Delta p = \frac{1}{\sqrt{\eta}}\frac{\hbar}{2}$ [4]. The classical uncer-

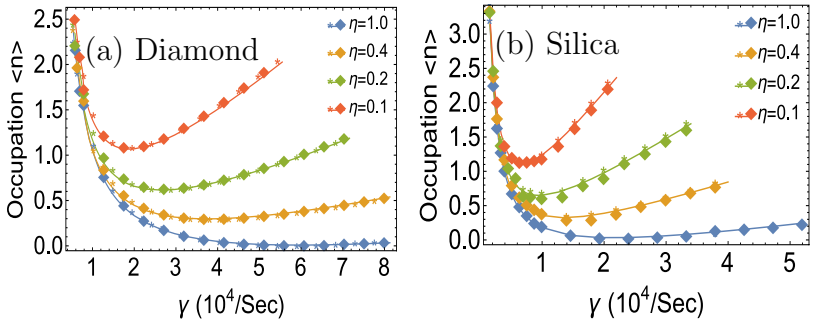

Figure 6.2. The steady state occupation in terms of the force feedback strength for diamond (left) and silica (right). The parameters in Tab. 6.1 are used. The solid lines, the asterisks and the diamonds correspond to the SSE, SME and the semi-classical results respectively. The data shown by the colors red, green, yellow and blue are for four different measurement efficiencies $\eta = (1.0, 0.4, 0.2, 0.1)$.

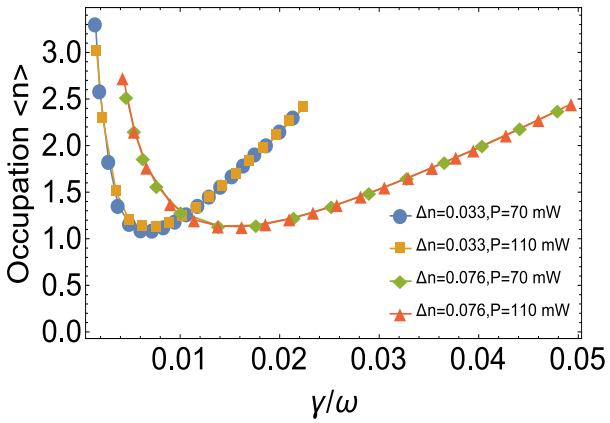

Figure 6.3. The steady state occupation in terms of the scaled force feedback strength for diamond, with the parameters given in Tab. 6.1. Δn is tuned by changing the beam waist. The measurement efficiency is fixed at $\eta = 0.1$. The solid lines are results from SSE and the symbols from semi-classical calculations.

tainty is fundamentally different from the quantum uncertainty, which intrinsically limits what we can know about physical observables.

The SSE and SME are numerically solved in the harmonic eigen-basis; details of the numerical method are given in Appx. B. The semi-classical equations of motion are numerically solved using a fourth-order Runge-Kutta algorithm and the momentum kick is added to the nanoparticle at each time step. All simulations are repeated over one thousand times and data is collected by averaging over the different runs to reduce the random noise.

The results are given in Figs. (6.2), which show the steady state occupation number with respect to the feedback strength for both diamond and silica. First, the quantum and semi-classical results match, even for the measurement efficiency $\eta = 1.0$, where a variation is intuitively expected between semi-classical and quantum calculations. This match justifies the use of semi-classical equations in the further analysis, which are more intuitively revealing and less computationally demanding. Second, as the measurement efficiency increases, the steady state occupation number is smaller for the same feedback strength. A better measurement efficiency indicates a more accurate measured position, which in turn leads to better feedback cooling. Third, for a fixed measurement efficiency η, the steady state occupation number has a minimal point (the optimal cooling limit), which can be reached as the feedback strength is tuned. As one increases the feedback strength, the feedback cooling is strengthened, but the feedback procedure itself adds heat into the system due to the noise of the measured position. The competition between the cooling and heating leads to the curved structure, which has a globe minimal. Fourth, even for the $\eta = 0.1$ measurement efficiency, a steady state occupation number close to $\langle n \rangle = 1$ can be reached, indicating the possibility of ground state cooling using the force feedback cooling scheme. Lastly, one can see that the optimal cooling limits are quite close for both silica and diamond when the measurement efficiency is chosen the same. We show below that the optimal cooling limit mainly depends on the measurement efficiency, but weakly depends on other parameters.

The fact that the quantum and semi-classical results match encourages us to further study the semi-classical equations, since they are intuitively revealing and can be solved more rapidly. We rescale the above semi-classical equations

$$\begin{aligned} \frac{d^2\tilde{x}}{d\tilde{t}^2} &= -\tilde{x} - \tilde{\gamma}\tilde{p}_m, \\ \tilde{p}(t+dt) &= \tilde{p}(t) + dW \cdot \Delta\tilde{p}, \\ \tilde{x}_i &= \tilde{x} + dW \cdot \Delta\tilde{x}, \end{aligned} \tag{6.25}$$

with the rescaled quantities $\tilde{x} = x/a_0$ with $a_0 = \sqrt{\hbar/(2m\omega)}$, $\tilde{t} = t\omega$, $\tilde{p} = p/(m\omega a_0)$ and the scaled feedback strength $\tilde{\gamma} = \gamma/\omega$. $\Delta\tilde{p} = \sqrt{2\dot{\tilde{E}} \cdot d\tilde{t}}$ and $\Delta\tilde{x} = \sqrt{1/(2\eta\dot{\tilde{E}}d\tilde{t})}$ with $\dot{\tilde{E}} = 2\dot{E}/(\hbar\omega^2)$. We define an important quantity

$$\Delta n \equiv \frac{2\pi\dot{E}}{\hbar\omega^2} = \pi\dot{\tilde{E}}, \tag{6.26}$$

which denotes the change in occupation number over one oscillation period. A detailed discussion of this quantity can be found in Ref. [4], and its importance will be shown below. As shown in the scaled semi-classical equation, the dynamics of force feedback cooling is totally governed by the parameter set $\{\eta,\tilde{\gamma},\Delta n\}$. In an experiment, if the measurement efficiency η is fixed, and we assume the feedback strength $\tilde{\gamma}$ can be freely tuned, then the parameter Δn determines the optimal cooling limit. As defined above, $\Delta n = (2\pi\dot{E})/(\hbar\omega^2)$ is determined both by the laser parameters (beam waist, wavelength, power) and the particle material properties (radius, dielectric constant, mass density). It is remarkable that all these parameters can group into one single variable Δn that determines the cooling limit.

In the rest of this subsection, we explore the trend of force feedback cooling as the parameter set is tuned. On the one hand, we numerically demonstrate that the parameter set $\{\eta,\tilde{\gamma},\Delta n\}$ indeed controls the dynamics (the cooling limit stays the same as long as the parameter set is fixed, no matter what material, beam waist or laser power are used). Using Eqs. (6.2) and (6.4), Δn is shown to be

$$\Delta n = 2\pi\frac{\dot{E}}{\hbar\omega^2} = \frac{\pi}{3}\frac{\epsilon-1}{\epsilon+2}R^3 w_0^2 k_0^5, \tag{6.27}$$

where $k_0 = 2\pi/\lambda$ is the incoming wave vector and w_0 is the beam waist. One finds that Δn is independent of the laser power, which means changing the laser power has no effect on the steady state occupation number if all other parameters are fixed. This is shown in Fig. (6.3) with $\eta = 0.1$ (the results with other η are similar), where the steady state occupation numbers in terms of the scaled feedback strength are exactly the same for the case with different trapping laser powers. Further, as we change Δn (by tuning w_0, α, or k_0), the steady state occupation number with respect to $\tilde{\gamma}$ varies, as shown by the curves with $\Delta n = 0.033$ and $\Delta n = 0.076$. It is worth noting that Fig. (6.3) also indicates the good agreement between semi-classical and quantum calculation as shown before.

The optimal cooling limit only depends on Δn and η. As shown in Fig. (6.2), a higher measurement efficiency η will lead to a lower steady state occupation number. However, it is not obvious how the optimal cooling limit depends on Δn. Figure (6.3) seems to show that the optimal cooling limits do not vary strongly with different Δn. To understand the role of Δn, we calculate the optimal cooling limit for several measurement efficiencies as a function of Δn. The result is shown in Fig. (6.4). The optimal cooling limit weakly depends on the parameter Δn. For measurement efficiencies $\eta = (0.1, 0.2, 0.4)$, the optimal cooling limit weakly increases as we increase the parameter Δn. The fact that Δn has little effect on the optimal cooling limit essentially means the measurement efficiency η is the most important parameter affecting the optimal cooling limit using force feedback. For reference, we list the optimal cooling limit with varied parameters in Tab. C.1 (shown in Appx. C).

6.4.2 Cooling by parametric feedback

In this subsection, we present the simulation results of the parametric feedback cooling by solving the SSE and the semi-classical equations. The SSE for parametric feedback cooling was already introduced in section 6.3. The semi-classical parametric

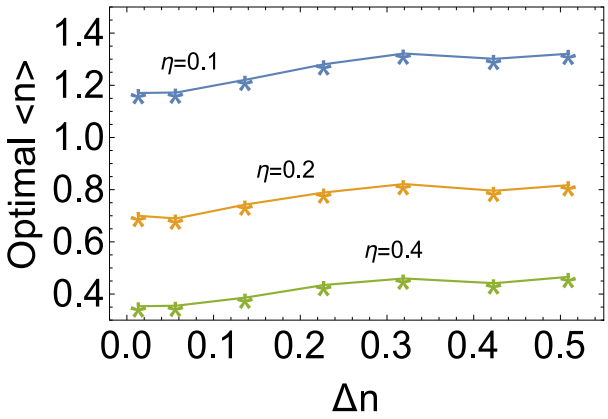

Figure 6.4. The optimal cooling limit in terms of the parameter Δn (by tuning the laser beam waist). The blue, yellow and green curves correspond to the cases with measurement efficiency η fixed at $(0.1, 0.2, 0.4)$. The data is based on semi-classical calculations.

feedback cooling was discussed in the previous chapter. For demonstration, we list below the semi-classical equations for parametric feedback cooling

$$\begin{aligned} m\frac{d^2x}{dt^2} &= -m\omega^2(1+\chi x_m \dot{x}_m)x, \\ x_i &= x + dW\cdot\Delta x, \\ p(t+dt) &= p(t) + dW\cdot\Delta p, \end{aligned} \tag{6.28}$$

where χ is the parametric feedback strength and the other quantities are the same as those in the force feedback equations. The semi-classical equation for parametric feedback cooling can also be scaled and the dynamics were shown to depend on the parameter set: the measurement efficiency η, the scaled parametric feedback strength $\tilde{\chi} = \hbar\chi/(2m)$, and the Δn (Eq. (6.26)). One can refer to the previous chapter for a detailed discussion. Similar to solving the equations for force feedback cooling, the semi-classical equations of motion for parametric feedback cooling are numerically solved using a fourth-order Runge-Kutta algorithm. The momentum kick is added to the nanoparticle at each time step. The SSE is solved in a harmonic eigen-basis and details are presented in Appx. B. All simulations are repeated over one thousand times and data is collected by averaging over the different runs.

Figure (6.5) gives the steady state occupation number in terms of parametric feedback strength, which has a similar structure to the force feedback cooling. First, the quantum and semi-classical results also match very well. Second, for different measurement efficiencies, there is also a minimal point (the optimal cooling limit) which can be reached when the parametric feedback strength is tuned. Comparing Fig. (6.2) with Fig. (6.5), the optimal cooling limit from the parametric feedback cooling is higher than that by force feedback. This indicates that ground state cooling by force feedback may be favored over parametric feedback. To clearly see that, we perform a calculation and collect the optimal cooling limit with respect to the measurement efficiency for the two cooling schemes. Figure (6.6) gives the result, which shows a much lower occupation number can be reached using the force feedback when the same measurement efficiency is used.

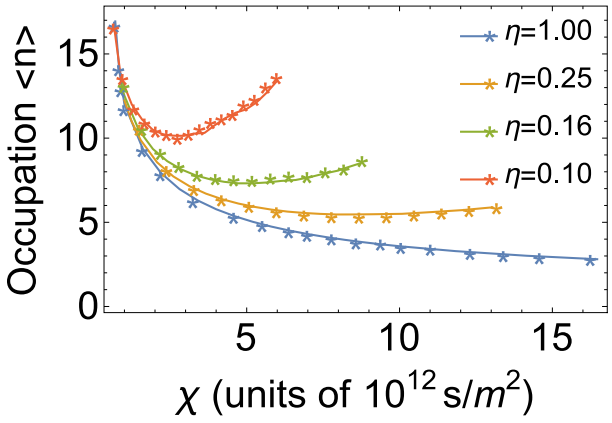

Figure 6.5. The steady state occupation in terms of the parametric feedback strength for diamond with parameters given in Tab. 6.1. The solid line is the semi-classical calculation while the asterisks correspond to the SSE. The blue, yellow, green, and red color correspond the calculations with measurement efficiencies $\eta = (1.0, 0.25, 0.16, 0.1)$ respectively.

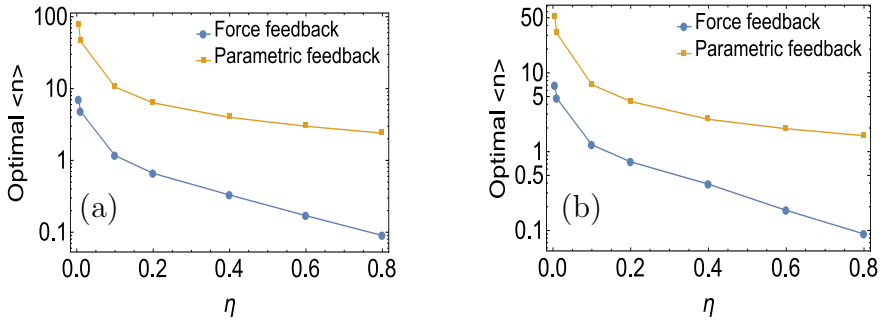

Figure 6.6. The optimal cooling limit with respect to the measurement efficiency. The blue lines connect the results from force feedback cooling, while the yellow lines connect the results from parametric feedback. The y axes are given in log scales. The data is obtained from solving semi-classical equations. **(a)** $\Delta n = 0.0142$. **(b)** $\Delta n = 0.1372$.

Similar to the force feedback, the parametric feedback cooling also only depends on the parameter set $\{\eta,\tilde{\chi},\Delta n\}$. First, as shown in Fig. (6.5), a lower optimal cooling limit can be obtained if one increases the measurement efficiency, which is the same as was observed for force feedback cooling. However, the dependence of the optimal cooling limit on Δn is quite different. As one increases Δn, the optimal cooling limit is observed to decrease significantly. The detailed discussion can be found in the previous chapter. Thus, unlike the force feedback cooling, one can efficiently tune both η and Δn so as to parametrically cool the levitated nanoparticle. For reference, we list the optimal cooling limit from parametric feedback with varied parameters in Tab. C.2 (shown in Appx. C).

In Ref. [11], $\langle n\rangle = 63$ was reached using parametric cooling. A recent experiment [75], reached $\langle n\rangle = 21$ with a better detection efficiency. In this experiment, a fused silica nano-sphere with radius about $R = 50$ nm was trapped in a polarized laser beam with wavelength $\lambda = 1064$ nm. The silica has a dielectric constant $\epsilon = 2.1$ and a mass of about $m = 1.13 \times 10^{-18}$ kg. The oscillation frequency in one transverse degree of freedom was measured to be $\omega = 2\pi \times 143$ kHz, which corresponds to an effective numerical aperture NA$\simeq 0.5$. The shot noise in this degree of freedom was measured close to $\langle \dot{n}\rangle \simeq 21$ kHz [11]. Combining the above parameters, we arrive at $\Delta n \simeq 0.9$. With these parameters, we simulate the parametric feedback cooling by scanning the measurement efficiency. The result is shown in Fig. (6.7), where an occupation number lower than 20 can be reached if the measurement efficiency is more than $\eta = 0.015$, and lower occupation number can be reached when the measurement efficiency increases.

6.5 The position measurement efficiency

The above calculation shows that the optimal cooling limit strongly depends on the position measurement efficiency. Thus, a natural question to ask is what is the maximal measurement efficiency for a given measurement scheme. In this section, we

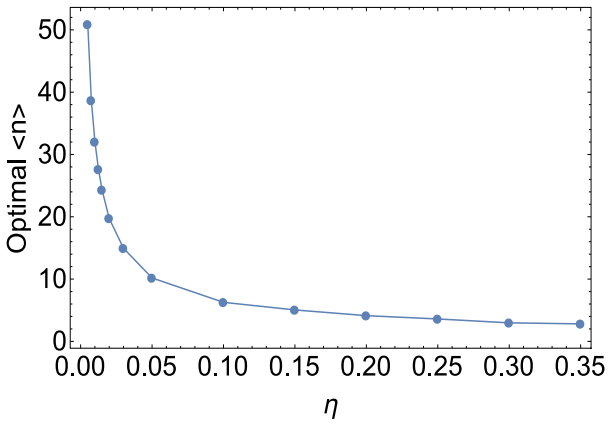

Figure 6.7. The simulation of an experiment [75] of parametric cooling of a fused silica, with $\Delta n \simeq 0.9$. The plot gives the optimal cooling limit in terms of the measurement efficiency η. The measurement efficiency is scanned from $\eta = 0.005$ to $\eta = 0.35$. The occupation number gets below $\langle n \rangle = 20$ when the measurement efficiency $\eta \geq 0.015$.

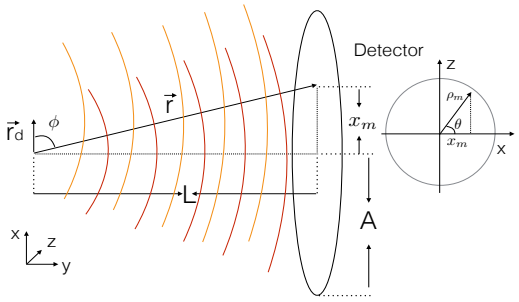

Figure 6.8. A schematic plot of the position measurement of a dielectric particle in a laser trap. The dipole induced radiation (denoted by the yellow lines) interferes with the laser beam (shown by the red lines), which is then detected at the detector. Using a balanced photon-detection scheme, the position of the particle is shown to be proportional to the measured signal.

analyze the position measurement efficiency using a balanced Homodyne detection scheme, which is widely used in recent experiments [49]. Similar to the case in the previous sections, we consider an incident Gaussian beam polarized along z, and propagating in y. The Gaussian beam is described by the formula

$$\begin{aligned}\vec{E}_G(r) &= E_0 \frac{w_0}{w(y)} e^{-\frac{x^2+z^2}{w^2(y)}} e^{i\left(ky-\eta(y)+\frac{k(x^2+z^2)}{2R(y)}\right)}\hat{z},\\ \vec{H}_G(r) &= \frac{1}{Z_0}(\vec{E}_G\cdot\hat{z})\hat{x}\end{aligned} \tag{6.29}$$

where $w(y) = w_0\sqrt{1+(y/y_0)^2}$, $\eta(y) = \arctan(y/y_0)$, $R(y) = y(1+(y_0/y)^2)$, w_0 is the laser beam waist, y_0 is the Rayleigh length and $Z_0 = \sqrt{\frac{\mu_0}{\epsilon_0}}$ is the vacuum impedance. As depicted in Fig. (6.8), the laser beam induces a dipole moment $\vec{P} = \alpha\vec{E}_G(r_d)$ from the nanoparticle located at r_d. A radiated electric field is produced from the dipole [61]

$$\begin{aligned}\vec{E}_D(r) &= Z_0\vec{H}_D\times\hat{n},\\ \vec{H}_D(r) &= \frac{k^2}{4\pi\epsilon_0}\frac{e^{ik|\vec{r}-\vec{r}_d|}}{|\vec{r}-\vec{r}_d|}(\hat{n}\times\vec{P})\end{aligned} \tag{6.30}$$

where $\vec{P}$ is the induced dipole moment defined above, and $\hat{n}$ is a unit vector in the radiation direction. The Gaussian beam and the dipole field interfere at the detector and the interference pattern depends on the nanoparticle's position. Monitoring the pattern should give us information of the particle's position.

In the following, I will show how the particle's position is obtained from the photons through the detector. For demonstration, I only consider the dipole motion in the direction with $\vec{r}_d = (x_d, 0, 0)$. The analysis of the other motions is similar. The fields interfere at the detector and induce an intensity distribution which is denoted by the average Poynting vector in the forward direction,

$$I(r) = \langle S\rangle_y = \frac{1}{2}(\vec{E}_G+\vec{E}_D)\times(\vec{H}_G^*+\vec{H}_D^*)\cdot\hat{y}. \tag{6.31}$$

In the balanced photodetection scheme, a signal is obtained by subtracting the detected photons in one half plane ($x_m > 0$) from those in the other half plane ($x_m < 0$)

$$\tilde{S} = \frac{\Delta t}{\hbar\omega}\left(\int_{x_m>0} I(r)ds - \int_{x_m<0} I(r)ds\right). \tag{6.32}$$

Substituting the fields by the formula given above and taking the paraxial approximation ($r \simeq L \gg x_m$), we arrive at the result for the above integral [2]

$$\tilde{S} = \frac{1}{2}\epsilon_0 c E_0^2 \frac{\Delta t}{\hbar\omega}\frac{\alpha k^3}{4\pi\epsilon_0} 2\sqrt{\pi} y_0 \frac{w_0^3}{y_0^3} x_d. \tag{6.33}$$

Obviously, the position x_d can be evaluated from the signal.

In a real measurement, an uncertainty will be attached to the measured position due to the photon statistics. For a collection of $N \sim \frac{1}{2}\epsilon_0 c E_0^2 \frac{\Delta t}{\hbar\omega}\frac{\pi w_0^2}{2}$ photons, the minimum uncertainty in photon number is $\sqrt{N}$, which yields a measured signal $\tilde{S}_m = \tilde{S} + dW\sqrt{N}$. Thus, the measured position is given by

$$x_m = x + \frac{dW\sqrt{N}}{\frac{1}{2}\epsilon_0 c E_0^2 \frac{\Delta t}{\hbar\omega}\frac{\alpha k^3}{4\pi\epsilon_0} 2\sqrt{\pi} y_0 \frac{w_0^3}{y_0^3}}. \tag{6.34}$$

The above equation can be reduced to the following familiar form

$$x_m = x + \frac{\hbar}{2}\frac{dW}{\sqrt{2m\Delta t \dot{E}\eta_{in}}}, \tag{6.35}$$

where $\dot{E} = \frac{2}{5}\frac{8\pi J_p}{3}\left(\frac{k^2}{4\pi\epsilon_0}\right)^2 \alpha^2 \frac{\hbar^2 k^2}{2m}$ is exactly the heating rate in the x degree of freedom, and

$$\eta_{\text{in}} = \frac{15}{8\pi}\text{NA}^4. \tag{6.36}$$

We call η_{in} the intrinsic achievable measurement efficiency, which defines an upper-bound for the balanced detection scheme. If the detector loses track of some fraction of the incoming photons, the overall measurement efficiency will be smaller by a factor of f: $\eta = f\eta_{in}$ with $f < 1$.

According to the formula $\eta_{\text{in}} = \frac{15}{8\pi}\text{NA}^4$, for NA=(0.9, 0.5), we can get efficiency η_{in}=(0.39,0.037). We should keep in mind that the result for high NA is not accurate since the above derivation is based on the paraxial approximation. For lower NA, we see that the intrinsic efficiency is too small to be satisfactory. In order to make the ground state cooling possible, we must find a measurement scheme with a higher intrinsic measurement efficiency.

[2]The integral can be greatly simplified if one notices that only the cross terms in Eq. (6.31) contribute to the integral.

There are several methods that are worth investigating for a better position measurement efficiency. This research is still ongoing and I shall only briefly mention them. One of the possibilities is to release the paraxial approximation by directly considering a tightly focused laser beam. The analytical calculation would be challenging, but we could numerically get an intuitive result. The other is to use a different measurement scheme, such as the one proposed in Ref. [83], where a parabolic mirror is used to collect the dipole radiation. Moreover, it is reported that there is possibility to get a better measurement efficiency by adopting the quantum metrology, by which one could possibly break the classical Cramér-Rao bound [84, 90, 91] and quantum Fisher information plays a role.

6.6 Summary and conclusion

In summary, we have extended the semi-classical calculation of the feedback cooling of a laser levitated nanoparticle in the shot-noise-dominant regime to the quantum domain. Using the theory of continuous quantum measurement, the measured particle position can be obtained continuously and the system state evolves stochastically due to the measurement back action. Cooling is achieved by feeding back the measured information (force and parametric feedback). Similar to the results from a model of semi-classical feedback scheme, the quantum cooling only depends on the feedback strength, the change of occupation number in one vibrational period (Δn) and the measurement efficiency. The minimum occupation number only depends on Δn and the measurement efficiency. The match between quantum and semi-classical results suggests that one can perform the much faster and more intuitive semi-classical calculation when analyzing the cooling of a levitated nanoparticle. The comparison between parametric feedback and force feedback cooling reveals that the force feedback cooling scheme is the more effective method to reach the ground state.

7. SUMMARY AND OUTLOOK

This thesis covered a small area of quantum physics based on five published papers during my graduate studies. In Chaps. 2 and 3, I discussed quasi-stable states of atoms and their related observing quantum effects. We spectrally probed the quasi-stable states of H and He atoms, where a series of survival peaks in the spectrum is formed as expected. When the electron is excited by UV laser with two frequencies, due to coherence, the survival spectrum can be modulated up to 10% by tuning the phase delay. The orientation of the quasi-stable state was also analyzed, which can be controlled by the phase delay as well. The relative stability of Rydberg states in the presence of strong lasers have attracted people's attention for decades. Various classical or semi-classical mechanisms have been proposed to explain this phenomenon [18–20]. The results presented in Chaps. 2 and 3 have aided in the understanding of this rapid expanding field. With the growing techniques of strong IR lasers, the phenomena discussed could be investigated experimentally.

In Chap. 4, I discussed the theory of decoherence and specifically explored the decoherence corresponding to the rotational degrees of freedom of a mesoscale quantum system. The theory of decoherence has been proposed to connect the quantum to classical transitions [9, 36]. It has been suggested that the decoherence theory addresses the problem of quantum measurement, however, some criticisms can also be found [92]. In the past decades, much effort has been placed on the decoherence of a meso-system's center of mass degree of freedom, while the rotational decoherence was widely ignored, probably due to the lack of efficient control over rotational motions. In Chap. 4, the general expression for rotational localization was obtained and the equation was applied to the cases of thermal photon and air molecule scattering. The study of rotational decoherence is important for the spreading interest in accurate quantum control over a system's mechanical motions. Together with decoherence in

translational degrees of freedom, rotational decoherence will surely contribute as a useful guide to future mesoscale experiments and applications.

Chapters 5 and 6 investigated shot noise heating and feedback cooling of a laser trapped nanoparticle. The shot noise heating from the trapping laser in the translational and rotational degrees of freedom were evaluated and compared in great detail. The feedback cooling of the levitated nanoparticle was then discussed in the laser-shot-noise-dominant regime. Both classical and quantum simulations were performed, where an exact match was observed. In the simulations, two different widely used feedback cooling schemes were discussed: the force feedback and the parametric feedback. Generally, the force feedback cooling yielded a better cooling limit than that from the parametric feedback cooling. Also, it was demonstrated that the cooling dynamics depends on three parameters: the feedback strength, the position measurement efficiency η and the change of occupation number in one vibrational period (Δn). Importantly, the position measurement efficiency was shown to be the key ingredient in getting a lower optimal cooling limit. Thus, the intrinsic position measurement efficiency of a given measurement scheme is important for ground state cooling. We analyzed the balanced Homodyne detection scheme and an upper bound of the position measurement efficiency was obtained. Since in a real experiment, the actual measurement efficiency should be smaller than the bound and the bound itself is not big enough, this analysis draws attention to big challenges to get the ground state cooling.

Fortunately, there are still many possibilities to improve the measurement efficiency. One of them is to release the paraxial approximation in the analysis. The other is to use a better measurement scheme, such as using a parabolic mirror to efficiently collect the dipole radiation [83, 93]. Moreover, it is reported that quantum metrology can break the classical shot noise limit [90], which could possibly be adopted to improve the measurement efficiency. The upper bound of the intrinsic position measurement efficiency in feedback cooling could be higher. To theoretically

predict the bound and experimentally get close to it should be an interesting and exciting work to do in the future.

APPENDICES

A. Parametric feedback cooling scheme

This appendix describes the parametric feedback cooling scheme and analyzes the cooling limit in the shot noise dominant regime. Perfect measurement is assumed in the following derivation. As an example, the average cooling power for one translational degree of freedom from the feedback is given by

$$\langle P \rangle = -\chi k \langle x^2 \dot{x}^2 \rangle \simeq -\frac{\chi E^2}{2m}. \tag{A.1}$$

where E is the system energy in this degree of freedom and k is the spring constant. The approximation is made above by ignoring the noise when taking the cycle average. The negative sign of the power guarantees an effective cooling during the feedback process. Combining with the translational shot noise heating rate, the system energy follows the differential equation

$$\frac{dE}{dt} = \dot{E}_T - \frac{\chi E^2}{2m}. \tag{A.2}$$

A steady state can be reached when the heating and cooling are balanced, which yields the cooling limit

$$\langle n \rangle_{limit} = \sqrt{\frac{2m\dot{E}_T}{\chi \hbar^2 \omega^2}}, \tag{A.3}$$

where ω is the oscillation frequency. One finds that a bigger χ gives a lower steady state energy and the particle mass together with the quantity $\dot{E}_T/\omega^2$ determine the final occupation. The differential equation can be analytically solved

$$E = E_{limit}\left(1 + \frac{2}{B\exp(2\sqrt{\frac{\chi \dot{E}_T}{2m}}t) - 1}\right), \tag{A.4}$$

where

$$B = \frac{\sqrt{\chi/2m}E_i + \sqrt{\dot{E}_T}}{\sqrt{\chi/2m}E_i - \sqrt{\dot{E}_T}}. \tag{A.5}$$

E_i is the initial energy of the system. The system gets cooled as time increases and the parameter $\sqrt{\frac{\chi \dot{E}_T}{2m}}$ is a measure of how fast the system is cooled. The feedback parameter χ has the unit $Time/Length^2$, which can be tuned to control the speed of cooling and the final steady state energy.

B. The numerical method for solving the SSE and the SME

This appendix introduces the numerical schemes used in the main text. The SSE (Eq. 6.19) is used in the calculations of the force feedback and parametric feedback cooling. The Hamiltonian is given by

$$\boldsymbol{H} = \boldsymbol{H}_0 + \boldsymbol{H}_{1,2}, \tag{B.1}$$

where $\boldsymbol{H}_0 = \hbar\omega(\boldsymbol{a}^\dagger\boldsymbol{a}+\frac{1}{2})$, $\boldsymbol{H}_1 = \gamma p_m \boldsymbol{x}$ denotes the force feedback and $\boldsymbol{H}_2 = \frac{\chi}{2} m\omega^2 x_m \dot{x}_m \boldsymbol{x}^2$ is the parametric feedback. At each time step, the Hamiltonian $\boldsymbol{H}$ is modified according to the measured position x_m and Eq. (6.21) is used in evaluating $\boldsymbol{H}_1$ and $\boldsymbol{H}_2$. To get a better estimate of the particle position, x_m at time t is calculated by taking the weighted time average of the directly measured positions in the earlier time $x_i(t')$,

$$x_m(t) = \frac{1}{\tau}\int_{-\infty}^{t} x_i(t') e^{-\frac{(t-t')}{\tau}} dt', \tag{B.2}$$

where $\tau \ll T$ and $T = 2\pi/\omega$ is the oscillation period. In our calculation, we take $\tau = T/20$. The wave function $|\psi(t)\rangle$ is represented in the eigen-basis of the operator $\boldsymbol{H}_0$. The initial state is chosen to be Gaussian, which is sensible because any other initial state would evolve rapidly into Gaussians under the continuous monitoring [59, 94–96]. The numerical propagation of Eq. (6.19) is split into two parts. The first part is the unitary evolution $d|\psi\rangle = -\frac{i}{\hbar}\boldsymbol{H}dt\,|\psi\rangle$ which is solved by the well known Crank-Nicolson method [66]. For the second part, the increment $d|\psi\rangle = \big(-\kappa(\boldsymbol{x} - \langle\boldsymbol{x}\rangle)^2 dt + \sqrt{2\kappa}(\boldsymbol{x} - \langle\boldsymbol{x}\rangle)\sqrt{dt}dW\big)\,|\psi\rangle$ is directly calculated in the eigen-basis, and the random number dW is generated and used at each time step. The wave function in the next time step is obtained by renormalizing the sum from the first and the second part of the propagation. Each calculation is repeated more than one thousand times and data is collected by averaging over them. The convergence is checked by changing the time step size as well as the number of eigenstates used in the simulation.

The SME (Eq. 6.17) is used in the force feedback cooling calculation. The density operator is also represented in the eigen-basis of Hamiltonian $\boldsymbol{H}_0$. Equation (6.17) is numerically solved using a second order Runge-Kutta algorithm. At each time step, a random number is generated and used, and the measured position x_m is used to get a feedback signal p_m, such that a modified Hamiltonian $\boldsymbol{H}$ is obtained. The simulation is performed many times and data is collected by averaging over a thousand trajectories. The convergence is also checked by changing the time step size and the number of eigenstates. The SME is basically equivalent to the SSE, so the results are expected to match when the same values of the parameters are used.

C. The data for optimal cooling limit

For reference, this appendix lists the data of optimal cooling limit with respect to the parameter set from both the force feedback and the parametric feedback cooling.

Table C.1.
This table gives the optimal cooling limit from the force feedback cooling scheme in terms of the parameters η and Δn. Each data point is obtained by scanning the feedback strength. The data roughly follows the formula $\langle n \rangle = \frac{0.48}{\sqrt{\eta}} - \eta + \frac{0.15}{\eta^{1/3}}\Delta n - 0.01\Delta n$.

η \ Δn	0.01	0.05	0.10	0.15	0.20	0.25	0.30
0.005	6.71	6.80	6.85	6.92	6.93	6.95	6.99
0.01	4.62	4.69	4.73	4.76	4.81	4.86	4.90
0.05	1.82	1.86	1.88	1.90	1.92	1.94	2.00
0.1	1.13	1.17	1.18	1.22	1.27	1.30	1.31
0.2	0.68	0.70	0.71	0.74	0.76	0.80	0.79
0.4	0.34	0.35	0.36	0.39	0.42	0.44	0.45

Table C.2.
This table gives the optimal cooling limit from the parametric feedback cooling scheme in terms of the parameters η and Δn. The data stops at $\Delta n = 0.2$ since our calculation becomes unstable for bigger values of Δn. Each data point is obtained by scanning the feedback strength.

η \ Δn	0.01	0.05	0.10	0.15	0.20
0.005	129	65.9	56.0	48.0	43.9
0.01	76.6	42.1	36.0	31.0	28.9
0.05	35.0	19.0	16.3	14.1	12.2
0.1	15.1	9.05	7.81	6.89	6.30
0.2	9.40	5.72	4.71	4.19	3.86
0.4	6.27	3.53	2.89	2.49	2.43

REFERENCES

REFERENCES

[1] C. Zhong and F. Robicheaux, "Spectrum of quasistable states in a strong infrared field," *Phys. Rev. A*, vol. 92, p. 013406, Jul 2015. [Online]. Available: http://link.aps.org/doi/10.1103/PhysRevA.92.013406

[2] ——, "Coherence and quasistable states in a strong infrared field," *Phys. Rev. A*, vol. 93, p. 033410, Mar 2016. [Online]. Available: https://link.aps.org/doi/10.1103/PhysRevA.93.033410

[3] ——, "Decoherence of rotational degrees of freedom," *Phys. Rev. A*, vol. 94, p. 052109, Nov 2016. [Online]. Available: https://link.aps.org/doi/10.1103/PhysRevA.94.052109

[4] ——, "Shot-noise-dominant regime for ellipsoidal nanoparticles in a linearly polarized beam," *Phys. Rev. A*, vol. 95, p. 053421, May 2017. [Online]. Available: https://link.aps.org/doi/10.1103/PhysRevA.95.053421

[5] C. Zhong, T. Li, and F. Robicheaux, "Quantum calculation of feedback cooling a laser levitated nanoparticle in the shot-noise-dominant regime," *arXiv preprint arXiv:1708.01203*, 2017.

[6] M. W. Noel, W. M. Griffith, and T. F. Gallagher, "Population trapping in extremely highly excited states in microwave ionization," *Phys. Rev. Lett.*, vol. 83, pp. 1747–1750, Aug 1999. [Online]. Available: http://link.aps.org/doi/10.1103/PhysRevLett.83.1747

[7] A. Arakelyan and T. F. Gallagher, "Metastable states in microwave ionization," *Phys. Rev. A*, vol. 87, p. 023410, Feb 2013. [Online]. Available: http://link.aps.org/doi/10.1103/PhysRevA.87.023410

[8] A. Arakelyan, T. Topcu, F. Robicheaux, and T. F. Gallagher, "Spectrum of quasistable states in a strong microwave field," *Phys. Rev. A*, vol. 90, p. 013413, Jul 2014. [Online]. Available: http://link.aps.org/doi/10.1103/PhysRevA.90.013413

[9] W. H. Zurek, "Decoherence, einselection, and the quantum origins of the classical," *Rev. Mod. Phys.*, vol. 75, p. 715, 2003.

[10] K. Hornberger and J. E. Sipe, "Collisional decoherence reexamined," *Physical Review A*, vol. 68, no. 1, p. 012105, 2003.

[11] V. Jain, J. Gieseler, C. Moritz, C. Dellago, R. Quidant, and L. Novotny, "Direct measurement of photon recoil from a levitated nanoparticle," *Phys. Rev. Lett.*, vol. 116, p. 243601, Jun 2016. [Online]. Available: http://link.aps.org/doi/10.1103/PhysRevLett.116.243601

[12] K. Jacobs and D. A. Steck, "A straightforward introduction to continuous quantum measurement," *Contemporary Physics*, vol. 47, no. 5, pp. 279–303, 2006.

[13] J. H. Gurian, K. R. Overstreet, H. Maeda, and T. F. Gallagher, "Connecting field ionization to photoionization via 17- and 36-ghz microwave fields," *Phys. Rev. A*, vol. 82, p. 043415, Oct 2010. [Online]. Available: http://link.aps.org/doi/10.1103/PhysRevA.82.043415

[14] E. S. Shuman, R. R. Jones, and T. F. Gallagher, "Multiphoton assisted recombination," *Phys. Rev. Lett.*, vol. 101, p. 263001, Dec 2008. [Online]. Available: http://link.aps.org/doi/10.1103/PhysRevLett.101.263001

[15] W. C. Henneberger, "Perturbation method for atoms in intense light beams," *Phys. Rev. Lett.*, vol. 21, pp. 838–841, Sep 1968. [Online]. Available: http://link.aps.org/doi/10.1103/PhysRevLett.21.838

[16] M. Pont, N. R. Walet, M. Gavrila, and C. W. McCurdy, "Dichotomy of the hydrogen atom in superintense, high-frequency laser fields," *Phys. Rev. Lett.*, vol. 61, pp. 939–942, Aug 1988. [Online]. Available: http://link.aps.org/doi/10.1103/PhysRevLett.61.939

[17] J. H. Eberly and K. C. Kulander, "Atomic stabilization by super-intense lasers," *Science*, vol. 262, no. 5137, pp. 1229–1233, 1993. [Online]. Available: http://www.sciencemag.org/content/262/5137/1229.abstract

[18] F. Benvenuto, G. Casati, and D. L. Shepelyansky, "Stability of rydberg atoms in a strong laser field," *Phys. Rev. A*, vol. 45, pp. R7670–R7673, Jun 1992. [Online]. Available: http://link.aps.org/doi/10.1103/PhysRevA.45.R7670

[19] K. C. Kulander, K. J. Schafer, and J. L. Krause, "Dynamic stabilization of hydrogen in an intense, high-frequency, pulsed laser field," *Phys. Rev. Lett.*, vol. 66, pp. 2601–2604, May 1991. [Online]. Available: http://link.aps.org/doi/10.1103/PhysRevLett.66.2601

[20] M. V. Fedorov and A. Movsesian., "Field-induced effects of narrowing of photoelectron spectra and stabilisation of rydberg atoms," *J. Phys. B*, vol. 21, 1988.

[21] H. G. Muller, "Tunneling excitation to resonant states in helium as main source of superponderomotive photoelectrons in the tunneling regime," *Phys. Rev. Lett.*, vol. 83, pp. 3158–3161, Oct 1999. [Online]. Available: http://link.aps.org/doi/10.1103/PhysRevLett.83.3158

[22] U. Eichmann, A. Saenz, S. Eilzer, T. Nubbemeyer, and W. Sandner, "Observing rydberg atoms to survive intense laser fields," *Phys. Rev. Lett.*, vol. 110, p. 203002, May 2013. [Online]. Available: http://link.aps.org/doi/10.1103/PhysRevLett.110.203002

[23] R. R. Jones and P. H. Bucksbaum, "Ionization suppression of stark states in intense laser fields," *Phys. Rev. Lett.*, vol. 67, pp. 3215–3218, Dec 1991. [Online]. Available: http://link.aps.org/doi/10.1103/PhysRevLett.67.3215

[24] L. D. Noordam, H. Stapelfeldt, D. I. Duncan, and T. F. Gallagher, "Redistribution of rydberg states by intense picosecond pulses," *Phys. Rev. Lett.*, vol. 68, pp. 1496–1499, Mar 1992. [Online]. Available: http://link.aps.org/doi/10.1103/PhysRevLett.68.1496

[25] F. Robicheaux., "Time propagation of extreme two-electron wavefunctions," *J. Phys. B*, vol. 45, 2012.

[26] C. H. K. M. Protopapas and P. L. Knight, "Atomic physics with super-high intensity lasers," *Rep. Prog. Phys.*, vol. 60, 1997.

[27] R. R. Jones, D. W. Schumacher, and P. H. Bucksbaum, "Population trapping in kr and xe in intense laser fields," *Phys. Rev. A*, vol. 47, pp. R49–R52, Jan 1993. [Online]. Available: http://link.aps.org/doi/10.1103/PhysRevA.47.R49

[28] P. Johnsson, R. López-Martens, S. Kazamias, J. Mauritsson, C. Valentin, T. Remetter, K. Varjú, M. B. Gaarde, Y. Mairesse, H. Wabnitz, P. Salières, P. Balcou, K. J. Schafer, and A. L'Huillier, "Attosecond electron wave packet dynamics in strong laser fields," *Phys. Rev. Lett.*, vol. 95, p. 013001, Jun 2005. [Online]. Available: http://link.aps.org/doi/10.1103/PhysRevLett.95.013001

[29] V. Carrat, E. Magnuson, and T. F. Gallagher, "Coherence, ionization, and recombination in a microwave field," *Phys. Rev. A*, vol. 92, p. 063414, Dec 2015. [Online]. Available: http://link.aps.org/doi/10.1103/PhysRevA.92.063414

[30] K. J. Schafer, M. B. Gaarde, A. Heinrich, J. Biegert, and U. Keller, "Strong field quantum path control using attosecond pulse trains," *Phys. Rev. Lett.*, vol. 92, p. 023003, Jan 2004. [Online]. Available: http://link.aps.org/doi/10.1103/PhysRevLett.92.023003

[31] F. Krausz and M. Ivanov, "Attosecond physics," *Rev. Mod. Phys.*, vol. 81, pp. 163–234, Feb 2009. [Online]. Available: http://link.aps.org/doi/10.1103/RevModPhys.81.163

[32] A. J. Leggett, S. Chakravarty, A. T. Dorsey, M. P. A. Fisher, A. Garg, and W. Zwerger, "Dynamics of the dissipative two-state system," *Rev. Mod. Phys.*, vol. 59, pp. 1–85, Jan 1987. [Online]. Available: http://link.aps.org/doi/10.1103/RevModPhys.59.1

[33] S. Gerlich, S. Eibenberger, M. Tomandl, S. Nimmrichter, K. Hornberger, P. J. Fagan, J. Tüxen, M. Mayor, and M. Arndt, "Quantum interference of large organic molecules," *Nature Communications*, vol. 2, p. 263, Apr. 2011.

[34] O. Romero-Isart, M. L. Juan, R. Quidant, and J. I. Cirac, "Toward quantum superposition of living organisms," *New Journal of Physics*, vol. 12, no. 3, p. 033015, 2010. [Online]. Available: http://stacks.iop.org/1367-2630/12/i=3/a=033015

[35] Q. Z. Tongcang Li, "Quantum superposition, entanglement, and state teleportation of a microorganism on an electromechanical oscillator," *Science Bulletin*, vol. 61, pp. 163–171, 2016.

[36] W. H. Zurek, "Decoherence and the transition from quantum to classical," *Physics Today*, p. 36, Oct 1991.

[37] E. Joos, H. D. Zeh, C. Kiefer, D. J. Giulini, J. Kupsch, and I.-O. Stamatescu, *Decoherence and the appearance of a classical world in quantum theory*. Springer Science & Business Media, 2013.

[38] M. Schlosshauer, "Decoherence, the measurement problem, and interpretations of quantum mechanics," *Reviews of Modern Physics*, vol. 76, no. 4, p. 1267, 2005.

[39] ——, *Decoherence and the Quantum-to-Classical Transition*. Springer, 2007.

[40] T. Fischer, "Decoherence of the orientation state," Ph.D. dissertation, Duisburg-Essen, 2014.

[41] J. D. Jackson, *Classical Electrodynamics*, 2nd ed. John Wiley, New York, 1999.

[42] W. H. Zurek, "Decoherence and the transition from quantum to classical–revisited," *arXiv preprint quant-ph/0306072*, 2003.

[43] D. E. Chang, C. Regal, S. Papp, D. Wilson, J. Ye, O. Painter, H. J. Kimble, and P. Zoller, "Cavity opto-mechanics using an optically levitated nanosphere," *Proceedings of the National Academy of Sciences*, vol. 107, no. 3, pp. 1005–1010, 2010.

[44] O. Romero-Isart, "Quantum superposition of massive objects and collapse models," *Physical Review A*, vol. 84, no. 5, p. 052121, 2011.

[45] J. Chan, T. M. Alegre, A. H. Safavi-Naeini, J. T. Hill, A. Krause, S. Gröblacher, M. Aspelmeyer, and O. Painter, "Laser cooling of a nanomechanical oscillator into its quantum ground state," *Nature*, vol. 478, no. 7367, pp. 89–92, 2011.

[46] A. D. O'Connell, M. Hofheinz, M. Ansmann, R. C. Bialczak, M. Lenander, E. Lucero, M. Neeley, D. Sank, H. Wang, M. Weides *et al.*, "Quantum ground state and single-phonon control of a mechanical resonator," *Nature*, vol. 464, no. 7289, pp. 697–703, 2010.

[47] A. A. Geraci, S. B. Papp, and J. Kitching, "Short-range force detection using optically cooled levitated microspheres," *Physical review letters*, vol. 105, no. 10, p. 101101, 2010.

[48] T. M. Hoang, Y. Ma, J. Ahn, J. Bang, F. Robicheaux, Z.-Q. Yin, and T. Li, "Torsional optomechanics of a levitated nonspherical nanoparticle," *Phys. Rev. Lett.*, vol. 117, p. 123604, Sep 2016. [Online]. Available: http://link.aps.org/doi/10.1103/PhysRevLett.117.123604

[49] J. Gieseler, B. Deutsch, R. Quidant, and L. Novotny, "Subkelvin parametric feedback cooling of a laser-trapped nanoparticle," *Physical review letters*, vol. 109, no. 10, p. 103603, 2012.

[50] J. Gieseler, M. Spasenović, L. Novotny, and R. Quidant, "Nonlinear mode coupling and synchronization of a vacuum-trapped nanoparticle," *Physical review letters*, vol. 112, no. 10, p. 103603, 2014.

[51] L. P. Neukirch and A. N. Vamivakas, "Nano-optomechanics with optically levitated nanoparticles," *Contemporary Physics*, vol. 56, no. 1, pp. 48–62, 2015.

[52] J. Gieseler, L. Novotny, C. Moritz, and C. Dellago, "Non-equilibrium steady state of a driven levitated particle with feedback cooling," *New Journal of Physics*, vol. 17, no. 4, p. 045011, 2015.

[53] B. A. Stickler, B. Papendell, and K. Hornberger, "Spatio-orientational decoherence of nanoparticles," *Physical Review A*, vol. 94, no. 3, p. 033828, 2016.

[54] S. Kuhn, A. Kosloff, B. A. Stickler, F. Patolsky, K. Hornberger, M. Arndt, and J. Millen, "Full rotational control of levitated silicon nanorods," *arXiv preprint arXiv:1608.07315*, 2016.

[55] S. Kuhn, P. Asenbaum, A. Kosloff, M. Sclafani, B. A. Stickler, S. Nimmrichter, K. Hornberger, O. Cheshnovsky, F. Patolsky, and M. Arndt, "Cavity-assisted manipulation of freely rotating silicon nanorods in high vacuum," *Nano letters*, vol. 15, no. 8, pp. 5604–5608, 2015.

[56] B. A. Stickler, S. Nimmrichter, L. Martinetz, S. Kuhn, M. Arndt, and K. Hornberger, "Ro-translational cavity cooling of dielectric rods and disks," *arXiv preprint arXiv:1605.05674*, 2016.

[57] B. Rodenburg, L. Neukirch, A. Vamivakas, and M. Bhattacharya, "Quantum model of cooling and force sensing with an optically trapped nanoparticle," *Optica*, vol. 3, no. 3, pp. 318–323, 2016.

[58] H. M. Wiseman and G. J. Milburn, *Quantum measurement and control*. Cambridge University Press, 2009.

[59] A. C. Doherty and K. Jacobs, "Feedback control of quantum systems using continuous state estimation," *Physical Review A*, vol. 60, no. 4, p. 2700, 1999.

[60] J. F. Ralph, K. Jacobs, and J. Coleman, "Coupling rotational and translational motion via a continuous measurement in an optomechanical sphere," *Phys. Rev. A*, vol. 94, p. 032108, Sep 2016. [Online]. Available: http://link.aps.org/doi/10.1103/PhysRevA.94.032108

[61] J. D. Jackson, *Classical electrodynamics*. Wiley, 1999.

[62] M. O. Scully and M. S. Zubairy, *Quantum optics*. AAPT, 1999.

[63] A. R. Edmonds, *Angular momentum in quantum mechanics*. Princeton University Press, 1996.

[64] C. F. Bohren and D. R. Huffman, *Absorption and scattering of light by small particles*. John Wiley & Sons, 2008.

[65] J. Trojek, L. Chvátal, and P. Zemánek, "Optical alignment and confinement of an ellipsoidal nanorod in optical tweezers: a theoretical study," *JOSA A*, vol. 29, no. 7, pp. 1224–1236, 2012.

[66] W. H. Press, S. A. Teukolsky, W. T. Vetterling, and B. P. Flannery, "Numerical recipies in c," 1992.

[67] J. Millen, T. Deesuwan, P. Barker, and J. Anders, "Nanoscale temperature measurements using non-equilibrium brownian dynamics of a levitated nanosphere," *Nature nanotechnology*, vol. 9, no. 6, pp. 425–429, 2014.

[68] L. P. Neukirch and A. N. Vamivakas, "Nano-optomechanics with optically levitated nanoparticles," *Contemporary Physics*, vol. 56, no. 1, pp. 48–62, 2015.

[69] Z. Xu and T. Li, "Detecting casimir torque with an optically levitated nanorod," *arXiv preprint arXiv:1704.08770*, 2017.

[70] T. M. Hoang, J. Ahn, J. Bang, and T. Li, "Electron spin control of optically levitated nanodiamonds in vacuum," *Nature communications*, vol. 7, 2016.

[71] L. P. Neukirch, E. Von Haartman, J. M. Rosenholm, and A. N. Vamivakas, "Multi-dimensional single-spin nano-optomechanics with a levitated nanodiamond," *Nature Photonics*, vol. 9, no. 10, p. 653, 2015.

[72] J. Millen, P. Fonseca, T. Mavrogordatos, T. Monteiro, and P. Barker, "Cavity cooling a single charged levitated nanosphere," *Physical review letters*, vol. 114, no. 12, p. 123602, 2015.

[73] N. Kiesel, F. Blaser, U. Delić, D. Grass, R. Kaltenbaek, and M. Aspelmeyer, "Cavity cooling of an optically levitated submicron particle," *Proceedings of the National Academy of Sciences*, vol. 110, no. 35, pp. 14 180–14 185, 2013.

[74] C. Genes, D. Vitali, P. Tombesi, S. Gigan, and M. Aspelmeyer, "Ground-state cooling of a micromechanical oscillator: Comparing cold damping and cavity-assisted cooling schemes," *Phys. Rev. A*, vol. 77, p. 033804, Mar 2008. [Online]. Available: https://link.aps.org/doi/10.1103/PhysRevA.77.033804

[75] V. Jain, F. Tebbenjohanns, and L. Novotny, "Microkelvin control of an optically levitated nanoparticle," in *Frontiers in Optics*. Optical Society of America, 2016, pp. FF5B–2.

[76] P. Asenbaum, S. Kuhn, S. Nimmrichter, U. Sezer, and M. Arndt, "Cavity cooling of free silicon nanoparticles in high vacuum," *Nature communications*, vol. 4, 2013.

[77] M. Aspelmeyer, T. J. Kippenberg, and F. Marquardt, "Cavity optomechanics," *Reviews of Modern Physics*, vol. 86, no. 4, p. 1391, 2014.

[78] H. Habibi, E. Zeuthen, M. Ghanaatshoar, and K. Hammerer, "Quantum feedback cooling of a mechanical oscillator using variational measurements: tweaking heisenberg?s microscope," *Journal of Optics*, vol. 18, no. 8, p. 084004, 2016.

[79] T. A. Brun, "A simple model of quantum trajectories," *American Journal of Physics*, vol. 70, no. 7, pp. 719–737, 2002.

[80] T. Li, S. Kheifets, and M. G. Raizen, "Millikelvin cooling of an optically trapped microsphere in vacuum," *Nature Physics*, vol. 7, no. 7, pp. 527–530, 2011.

[81] J. Vovrosh, M. Rashid, D. Hempston, J. Bateman, M. Paternostro, and H. Ulbricht, "Parametric feedback cooling of levitated optomechanics in a parabolic mirror trap," *JOSA B*, vol. 34, no. 7, pp. 1421–1428, 2017.

[82] C. Genes, D. Vitali, P. Tombesi, S. Gigan, and M. Aspelmeyer, "Ground-state cooling of a micromechanical oscillator: Comparing cold damping and cavity-assisted cooling schemes," *Physical Review A*, vol. 77, no. 3, p. 033804, 2008.

[83] J. Vovrosh, M. Rashid, D. Hempston, J. Bateman, and H. Ulbricht, "Controlling the motion of a nanoparticle trapped in vacuum," *arXiv preprint arXiv:1603.02917*, 2016.

[84] A. Gover, A. Nause, E. Dyunin, and M. Fedurin, "Beating the shot-noise limit," *Nature Physics*, vol. 8, no. 12, pp. 877–880, 2012.

[85] P. Hyllus, W. Laskowski, R. Krischek, C. Schwemmer, W. Wieczorek, H. Weinfurter, L. Pezzé, and A. Smerzi, "Fisher information and multiparticle entanglement," *Physical Review A*, vol. 85, no. 2, p. 022321, 2012.

[86] A. Jonáš and P. Zemanek, "Light at work: The use of optical forces for particle manipulation, sorting, and analysis," *Electrophoresis*, vol. 29, no. 24, pp. 4813–4851, 2008.

[87] P. Busch, P. J. Lahti, J.-P. Pellonpää, and K. Ylinen, *Quantum measurement*. Springer, 2016.

[88] K. Jacobs, "Wave-function monte carlo method for simulating conditional master equations," *Physical Review A*, vol. 81, no. 4, p. 042106, 2010.

[89] L. G. Villanueva, R. B. Karabalin, M. H. Matheny, E. Kenig, M. C. Cross, and M. L. Roukes, "A nanoscale parametric feedback oscillator," *Nano letters*, vol. 11, no. 11, pp. 5054–5059, 2011.

[90] V. Giovannetti, S. Lloyd, and L. Maccone, "Quantum metrology," *Physical review letters*, vol. 96, no. 1, p. 010401, 2006.

[91] M. Zwierz, C. A. Pérez-Delgado, and P. Kok, "General optimality of the heisenberg limit for quantum metrology," *Phys. Rev. Lett.*, vol. 105, p. 180402, Oct 2010. [Online]. Available: https://link.aps.org/doi/10.1103/PhysRevLett.105.180402

[92] O. Pessoa Jr, "Can the decoherence approach help to solve the measurement problem?" *Synthese*, vol. 113, no. 3, pp. 323–346, 1997.

[93] M. Rashid, M. Toroš, and H. Ulbricht, "Wigner function reconstruction in levitated optomechanics," *Quantum Measurements and Quantum Metrology*, vol. 4, no. 1, pp. 17–25, 2017.

[94] K. Jacobs and P. L. Knight, "Linear quantum trajectories: Applications to continuous projection measurements," *Phys. Rev. A*, vol. 57, pp. 2301–2310, Apr 1998. [Online]. Available: https://link.aps.org/doi/10.1103/PhysRevA.57.2301

[95] W. H. Zurek, S. Habib, and J. P. Paz, "Coherent states via decoherence," *Physical Review Letters*, vol. 70, no. 9, p. 1187, 1993.

[96] B. M. Garraway and P. L. Knight, "Evolution of quantum superpositions in open environments: Quantum trajectories, jumps, and localization in phase space," *Phys. Rev. A*, vol. 50, pp. 2548–2563, Sep 1994. [Online]. Available: https://link.aps.org/doi/10.1103/PhysRevA.50.2548

VITA

VITA

Education

• Ph.D. Department of Physics, Purdue University, 08/2012~12/2017.

• M.S. Department of Physics, Beijing Normal University, 09/2008~07/2011.

• B.S. Department of Physics, Minzu University of China, 09/2004~07/2008.

Interests

• Quantum measurement and control, Quantum computation, Quantum fundamentals, Black Hole physics.

• Math riddles, Literature, Playing the piano and flute.

Publication

• C. Zhong, F. Robicheaux, "Shot-noise-dominant regime for ellipsoidal nanoparticles in a linearly polarized beam". Phys. Rev. A 95, 053421 (2017).

• C. Zhong, F. Robicheaux, "Decoherence of rotational degrees of freedom". Phys, Rev. A 94, 052109 (2016).

• C. Zhong, F. Robicheaux, "Coherence and quasistable states in a strong infrared field". Phys, Rev. A 93, 033410 (2016).

• C. Zhong, F. Robicheaux, "Spectrum of quasistable states in a strong infrared field". Phys, Rev. A 92, 013406 (2015).

• C. Zhong, Sijie Gao, "Particle collisions near the cosmological horizon of Reissner-Nordstrm de Sitter black holes". JETP Lett. vol. 94 issue 8 (2011).

• Sijie Gao, C. Zhong, "Non-extremal Kerr black holes as particle accelerators". Phy. Rev. D 84, 044006 (2011).

• C. Zhong, T. Li, F. Robicheaux, "Quantum calculation of feedback cooling a laser levitated nanoparticle in the shot-noise-dominant regime" Preprint arXiv:1708.01203